Electrochemical Stability of Noble-Metal Based Nanoparticles as Oxygen Reduction and Evolution Catalysts for Vanadium Air Redox Flow Batteries

Betreuender Gutachter: Prof. Dr. J. Parisi, Universität Oldenburg
Zweiter Gutachter: Prof. Dr. G. Wittstock, Universität Oldenburg
Dritter Prüfer: Prof. Dr. C. Agert, Universität Oldenburg

Tag der Disputation: 04.03.2016

Abstract

The transition towards a sustainable energy system implies the need of cost-efficient energy storage systems. Thus, a variety of new types of batteries is researched. The vanadium air redox flow battery (VARFB) is a combination of a redox flow battery and a proton exchange membrane unitized regenerative fuel cell (PEM-URFC). One major challenge for the VARFB and related systems is to increase the stability of the noble metal based catalysts for oxygen reduction reaction (ORR) and oxygen evolution reaction (OER). In this thesis, the structure and electrochemical stability of these catalysts was investigated.

A strong degradation of carbon supported platinum (Pt) nanoparticles as ORR catalyst was observed with cyclic voltammetry after an OER-ORR protocol simulating repeated changes between charge and discharge mode of the VARFB. Vanadium (V) ions in the solution lowered the degradation. Electrochemical quartz crystal microbalance (EQCM) measurements on bulk Pt in V-containing solution showed no deposition of V compounds, but a decrease of the electrode mass in the range of V^{3+} and VO^{2+} oxidizing potentials. It is suggested, that these oxidations reduce the surface (hydr)oxide occupancy at the Pt electrode, so that the degrading ORR currents are lower, and finally less degradation is observed.

Iridium decorated Pt nanorods (Ir@Pt) were colloidchemically synthesized as bifunctional OER-ORR catalysts. Structural studies were conducted with X-ray diffraction (XRD), transmission electron microscopy (TEM) and energy dispersive X-ray (EDX) spectroscopy. The influence of the Ir decoration towards the electrochemical stability was investigated via cyclic voltammetry. The stability of Ir was lowered by the Pt support during an OER-ORR stability protocol due to Pt degradation. The stability of Pt was increased via Ir decoration. This is explained by the IrO_2 degradation and a subsequent uncovering of additional Pt surface area. A mild annealing procedure was conducted aiming at improved adhesion of the Ir nanodots to the support, but did not increase the OER or ORR stability of Ir@Pt.

Ir nanodots were succesfully deposited on ruthenium oxide (RuO_2) nanoparticles as OER catalyst. Investigations of the structure and electrochemical stability of Ir@RuO_2 were conducted with XRD, TEM, EDX, and cyclic voltammetry. The stability of RuO_2 could not be increased by the decoration with Ir nanodots. The OER stability of pure Ir nanodots, that are oxidized to IrO_2, is even lower than both RuO_2 and Ir@RuO_2. The higher material-specific stability of IrO_2 seems to be overcompensated by size effects. A mild annealing procedure did not improve the OER stability of Ir@RuO_2.

Zusammenfassung

Der Übergang zu einem nachhaltigen Energiesystem impliziert einen Bedarf an kostengünstigen Energiespeichersystemen. Deshalb wird eine Vielfalt neuer Batterie-Typen erforscht. Die Vanadium-Luft-Redox-Flow-Batterie (VARFB) ist eine Kombination aus einer Redox-Flow-Batterie und einer Protonen-Austausch-Membran-basierten, Vereinheitlichten Regenerativen Brennstoffzelle (PEM-URFC). Eine zentrale Herausforderung für die VARFB und verwandte Systeme ist die Verbesserung der Stabilität der edelmetallbasierten Katalysatoren für die Sauerstoffreduktion (ORR) und Sauerstoffentwicklung (OER). Im Rahmen dieser Doktorarbeit wurde die Struktur und elektrochemische Stabilität solcher Katalysatoren untersucht.

Eine starke Degradation von Platin-Nanopartikeln (Pt) auf Kohlenstoff-Trägerpartikeln als ORR-Katalysator wurde mittels Zyklovoltammetrie nach einem OER-ORR-Protokoll beobachtet, das wiederholte Wechsel zwischen dem Lade- und Entladebetrieb der VARFB zu simuliert. Vanadium-Ionen (V) in der Lösung verringerten die Degradation. Messungen mit der Elektrochemischen Quarz-Kristall-Mikrowaage (EQCM) an makroskopischen Platin-Schichten in V-haltiger Lösung zeigten keine Abscheidung von V-Verbindungen, aber eine Verringerung der Elektrodenmasse im Bereich der V^{3+}- und VO^{2+} oxidierenden Potentiale. Es wird vermutet, dass diese Oxidationen die Oberflächenbelegung der Pt-Elektrode mit (Hydr-)Oxiden verringern, so dass die degradierenden ORR-Ströme geringer sind und somit letztendlich weniger Degradation beobachtet wird.

Mit Iridium dekorierte Platin-Nanostäbchen (Ir@Pt) wurden kolloidchemisch hergestellt, um bifunktionale OER-ORR-Katalysatoren zu ergeben. Strukturelle Untersuchungen wurden mit Röntgenbeugung (XRD), Transmissions-Elektronenmikroskopie (TEM) und Energiedispersiver Röntgenspektroskopie (EDX-Spektroskopie) durchgeführt. Der Einfluss der Ir-Dekoration auf die elektrochemische Stabilität wurde mit Hilfe der Zyklovoltammetrie untersucht. Die Stabilität von Ir innerhalb eines OER-ORR-Stabilitätsprotokolls wurde aufgrund von Pt-Degradation durch die Pt-Trägerpartikel verringert. Die Stabilität von Pt wurde durch die Ir-Dekoration erhöht. Dies wird durch die Degradation des IrO_2 und einer daraus resultierenden Freigabe zusätzlicher Pt-Oberfläche erklärt. Eine vorsichtige Wärmebehandlung wurde mit dem Ziel durchgeführt, die Anhaftung der Ir-Nanopunkte an die Trägerpartikel die Stabilität zu verbessern, führte aber nicht zur Verbesserung der OER- oder ORR-Stabilität der Ir@Pt-Katalysatoren.

Ir-Nanopunkte wurden erfolgreich auf Rutheniumoxid-Nanopartikeln (RuO_2) als

OER-Katalysatoren abgeschieden. Studien zur Struktur und elektrochemischen Stabilität an den Ir@RuO_2-Katalysatoren wurden mit XRD, TEM, EDX-Spektroskopie und Zyklovoltammetrie durchgeführt. Die Stabilität von RuO_2 konnte durch Dekoration mit Ir-Nanopunkten nicht erhöht werden. Die Stabilität von puren Ir-Nanopunkten, die zu IrO_2 oxidiert werden, ist sogar sowohl geringer als RuO_2 als auch als Ir@RuO_2. Die höhere materialspezifische Stabilität von IrO_2 scheint durch Größeneffekte überkompensiert zu werden. Eine vorsichtige Wärmebehandlung führte nicht zu einer Verbesserng der OER-Stabilität der Ir@RuO_2-Katalysatoren.

Contents

List of Figures

List of Tables

Abbreviations

CV: cyclic voltammogramm

EDX: energy dispersive X-Ray

EQCM: electrochemical quartz crystal microbalance

FC: fuel cell

HUPD: hydrogen under potential deposition

ICDD: International Centre for Diffraction Data

MMSE: mercury / mercury sulfate electrode

OER: oxygen evolution reaction

ORR: oxygen reduction reaction

PEM: protone exchange membrane

RFB: redox flow battery

STEM: scanning transmission electron microscopy

TEM: transmission electron microscopy

URFC: unitized regenerative fuel cell

VRFB: vanadium redox flow battery

VARFB: vanadium air redox flow battery

WE: water electrolyzer

XRD: X-ray diffraction

Symbols

α: transfer coefficient

b: full width of half maximum

c: light velocity

c_{m}: frequency-mass coefficient

c_{O}: concentration of oxidized species

c_{R}: concentration of reduced species

d: lattice spacing, crystallite diameter

D: diffusion constant

δ: half path difference

Δf: frequency change

Δm: mass change

e: elementary charge

E: potential, energy of electron

E^0: formal potential

E_{kin}: kinetic energy of electron

E_{rest}: rest energy of electron

η: overpotential

F: Faraday constant

f_0: resonance frequency

h: Planck constant

I: current

I_{OER}: OER current

I_{ORR}: ORR peak current

j: current density

j_{a}: anodic current density

j_{c}: cathodic current density

j_0: exchange current density

k: Scherrer constant

λ: wavelength

m_{e0}: electron's rest mass

μ_{q}: shear modulus of quartz

n: order of interference maximum, number of charges

p: momentum of electron

π: pi

Q_{Hdes}: hydrogen desorption charge

R: universal gas constant

ρ_{q}: density of quartz

T: temperature

t: time

Θ: diffraction angle

U: voltage

1 Introduction

The transition towards a sustainable energy system implies the challenge of matching the volatile energy production by wind and solar power plants with the energy demand. This can, for example, be achieved by using decentralized, stationary electrochemical energy storage systems [1]. Beyond the most popular energy storage technologies, the lead acid battery and the lithium ion battery, a variety of new types of batteries is researched.

The vanadium air redox flow battery (VARFB) is a combination of a redox flow battery and a proton exchange membrane unitized regenerative fuel cell (PEM-URFC) [2–8]. Due to stability reasons, noble metal based catalysts are usually applied [9, 10]. For oxygen reduction during discharge, platinum (Pt) catalysts are common. For oxygen evolution during charge, iridium oxide (IrO$_2$) or iridium-ruthenium-based mixed oxides serve mostly as catalyst. In order to lower the catalysts' material costs, nanoparticles are applied. Unfortunately, nanoparticles are less stable than the bulk material. Consequently, one major task is to improve the catalysts' stability under this conditions [10].

During operation, an undesired crossover of vanadium (V) cations into the water/air half-cell occurs. The negative influence on the battery's efficiency was already reported [7]. Deposition of vanadium compounds on carbon felts was reported in vanadium redox flow batteries [11]. Also, vanadium compounds were intentionally deposited on carbon and Pt at higher pH values [12, 13]. But so far, it has not been investigated, if vanadium compounds deposit on the Pt catalyst under operation conditions in a VARFB or if there is any other influence of this vanadium contamination on the stabilty of the Pt catalyst.

In chapter 2, the VARFB is introduced, general approaches to improve the stability of ORR and OER catalysts in acidic media are presented and a survey is given about deposition of Vanadium compounds. Furthermore, stability studies on bifunctional OER-ORR catalysts and oxygen evolution catalysts are reviewed.

In chapter 3, the experimental methods are outlined. Namely, these are nanoparticle synthesis, as well as transmission electron microscopy (TEM), energy dispersive X-ray (EDX) spectroscopy and X-ray diffraction (XRD) for structural investigations and cyclic voltammetry, as well as electrochemical quartz crystal microbalance (EQCM) for electrochemical characterization and stability studies.

In chapter 4, cyclic voltammetry and EQCM are used to investigate, whether V compounds are deposited on the Pt surface under operating conditions or whether

the V ions influence the stability of Pt in any other way. These studies are conducted on polycrystalline bulk Pt and on carbon supported Pt nanoparticles.

It is shown in the literature, that the preparation of inhomogeneous surfaces via, for example, decoration of nanoparticles with other nanoparticles can lead to improvements in catalytic activity and stability [14, 15]. Moreover, the stepwise synthesis allows a higher control of the morphology and, thus, the electrochmical properties of the nanoparticles. In chapter 5, the structure of the synthesized nanoparticles is studied and the electrochemical stability of Ir decorated Pt nanorods towards oxygen evolution reaction (OER) and oxygen reduction reaction (ORR) is compared to unsupported Ir nanodots and pure Pt nanorods. In addition, the influence of a mild annealing procedure on the structure and the electrochemical stability is investigated.

Chapter 6 deals with the influence of the decoration of RuO_2 nanoparticles with Ir nanodots on the structure and the stability towards the OER and, also, with the influence of an annealing procedure on both.

Conclusions and perspectives are presented in chapter 7.

2 Background

In this chapter, the background of the conducted studies on the stability of catalysts for VARFBs is reviewed. Namely, the vanadium air redox flow battery is introduced. Literature that might help to investigate, whether V compounds deposit on Pt catalysts or influence the catalysts' stability in any other way, is reviewed. The state of the art concerning research on bifunctional OER-ORR catalysts in acidic media is described focussing on the catalysts' stability. Finally, efforts to improve the stability of oxygen evolution catalysts in acidic media are illustrated.

2.1 Vanadium Air Redox Flow Battery (VARFB)

In order to lower the costs of energy storage systems, that are needed for a sustainable energy system, research is conducted on established technologies like the lead acid battery and the lithium ion battery, but also on a variety of new types of batteries. One promising energy storage system is the redox flow battery (RFB) with the most famous all vanadium (V) RFB using the V^{2+}/ V^{3+} redox couple for the negative electrolyte and the VO^{2+} / VO_2^+ redox couple for the positive one [16]. In the vanadium air redox flow battery (VARFB), the positive half cell's electrolyte is replaced by oxygen and water as reaction partners (Fig. 2.1). This leads to a saving of the positive electrolyte, meaning a cost reduction and roughly a doubled energy density [2–7]. The basic reaction equations of the VARFB are

$$4V^{2+} \rightleftarrows 4V^{3+} + 4e^- \tag{2.1}$$

at the electrolyte side and

$$O_2 + 4e^- + 4H^+ \rightleftarrows 2H_2O \tag{2.2}$$

at the water/air side.

Compared to a proton exchange membrane unitized regenerative fuel cell (PEM URFC) system [4, 7, 17–20], the VARFB has a negative half cell acting as proton reservoir, a lower open circuit potential due to the different redox couple, and does not need Pt as catalyst for the negative half cell reaction. For the oxygen reduction reaction (ORR) during discharge and the oxygen evolution reaction (OER) during charge, noble metal-based catalysts are usually needed in acidic systems due to their comparatively high stability. Pt is commonly applied as ORR catalyst, while the OER catalyst is IrO_2 or a Ir-Ru-based mixed oxide [9].
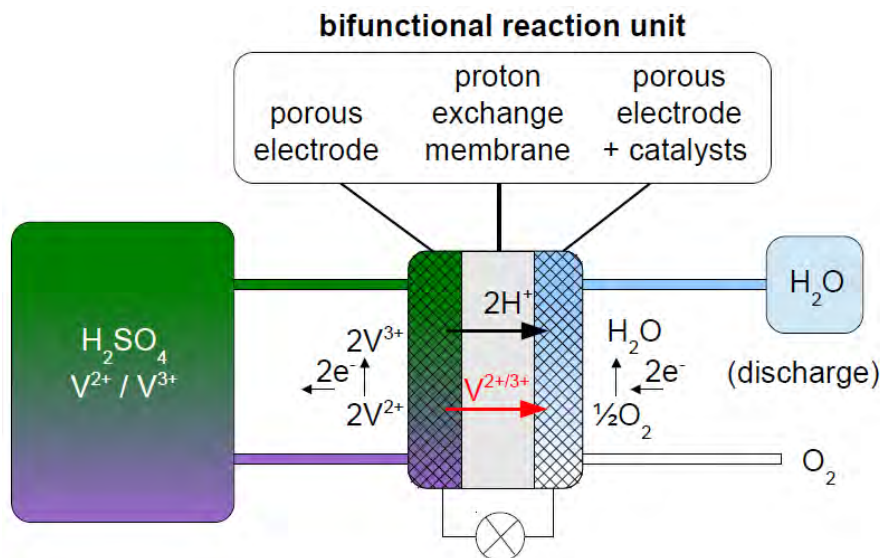
Figure 2.1: *Scheme of the vanadium air redox flow battery. In the discharge case, V ions are oxidized on the Vanadium electrolyte side of the reaction unit, while oxygen is reduced to water. Electrons can power an electrical load. Protons get to the water/air side of the reaction unit to serve as reaction partners for oxygen and ensure charge neutrality, or in other words to close the circuit. An undesired crossover of V ions takes place (red arrow).*

A common strategy to reduce the amount of noble metal and, thus, the costs is the use of nanoparticles instead of bulk material. Furthermore, the use of a bifunctional reaction unit has been proposed instead of two separate units for charge and discharge, respectively [7,17]. Consequently, the stability requirements for the bifunctional reaction unit are higher than for each separate discharge or charge unit.

In VARFBs, as in other redox flow systems, an undesired crossover of ions through the proton exchange membrane from one electrolyte to the other takes place [6,7,16]. One problem resulting from the crossover of V^{2+} or V^{3+} to the water / air side in the VARFB is a loss of energy efficiency due to oxidation or reduction of the V ions instead of water or oxygen. To be more precise, V^{2+} or V^{3+} can be finally oxidized to VO_2^+ during charge [7]. During discharge, previously produced VO_2^+ can be finally reduced to V^{2+}. Moreover, it is reported that V^{2+} is oxidized at Pt by reduction of protons to H_2 [6]. As a consequence, it is crucial to avoid Pt contamination of the vanadium electrolyte during operation, because this would not only lead to a discharge but moreover lead to a massive evolution of hydrogen gas. This can be achieved by ensuring a satisfying stability of the Pt or by replacing it with other catalysts.

Another important issue, which has not been investigated in detail so far, is the

question of whether vanadium ions crossing the membrane can lead to deposits on the surface of platinum catalysts in a bifunctional reaction unit during the operation of the battery and, therefore, reduce the electrochemically active surface area and, thus, the overall activity for the ORR. More generally, the question remains, whether there is any influence of a V contamination on the stability of Pt [8]. For example, Wen et al. [21] observed a voltage drop in a system similar to a VARFB and assumed the Pt nanoparticles to be poisoned by V ions.

2.2 General Approaches to Increase the Stability of Oxygen Reduction / Evolution Catalysts in Acidic Media

The overall reaction of the oxygen reduction reaction (ORR) and the oxygen evolution reaction (OER) in acidic media is:

$$O_2 + 4e^- + 4H^+ \rightleftarrows 2H_2O \tag{2.3}$$

Despite the apparent simplicity and beauty of this equation, the elucidation of the reaction mechanisms is challenging and still not finished. Mayrhofer's group proposes the reaction pathways shown in Fig. 2.2 [10].
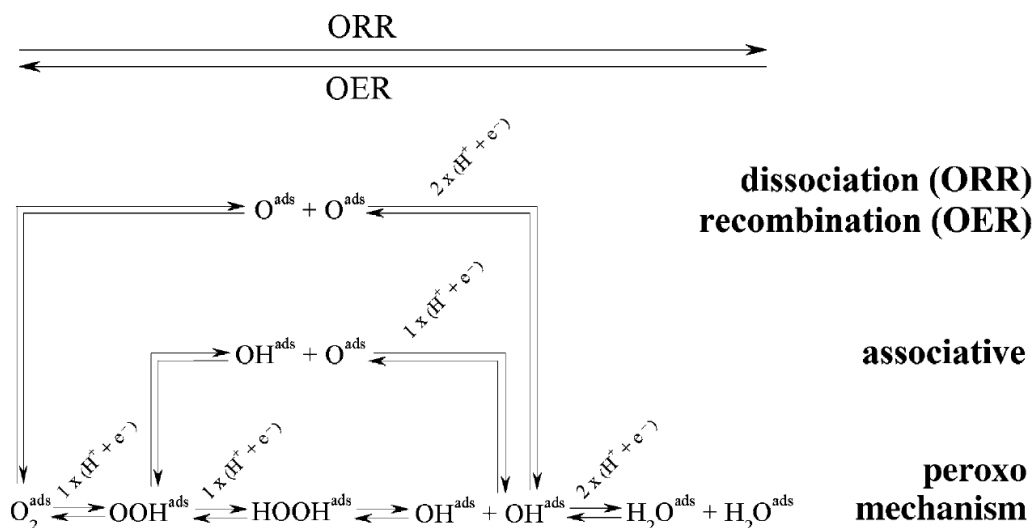
Figure 2.2: *Scheme of proposed reaction mechanisms for the ORR and OER in acidic media taken from [10].*

In acidic proton exchange membrane fuel cells (PEM-FC), proton exchange membrane water electrolyzers (PEM-WE) and related systems like PEM-based unitized

regenerative fuel cells (PEM-URFC) or vanadium air redox flow batteries (VARFB) the catalysts for OER and ORR are commonly noble metal based: Pt is used as ORR catalyst, while IrO_2 or Ir-Ru-based mixed oxides serve as OER catalysts [9].

Concerning the noble metal based catalysts, the main challenge is to reduce the costs by raising the noble metal mass specific activity and to increase the stability [22]. More research has been performed on these topics on Pt-based ORR catalysts than on OER catalysts.

The common ORR catalysts for fuel cells are carbon supported Pt nanoparticles. To increase the mass specific activity further, the ORR activity per Pt binding site can be slightly enhanced and the amount of Pt, that is not placed at the nanoparticles' surface has to be reduced. To achieve that, Pt-based alloy nanoparticles were researched, as well as core-shell nanoparticles with a Pt shell and nanoparticles with $Pt_3Ni(111)$-surfaces. Another route is the deposition of Pt monolayers or thin films on nanostructured support materials [22–26]. Moreover, the catalytic activity is structure-sensitive, meaning that the acitivity depends on the Pt facet exposed to the electrolyte, the kind and amount of edge atoms and the particle size, so it is a combination of electronic and geometric effects [10]. Recently, the Markovic group reported on the role of surface defects on the ORR activity of Pt [27]. A 4-fold improvement in ORR current density could be achieved by the Adzic group by replacing a part of Pt surface atoms of a Pt monolayer on palladium (Pd) by Ir and other transition metals [28]. Wang et al. could improve the ORR activity of Pd-Pt core-shell nanoparticles by decoration with Ir [29].

The same principles apply for OER catalysts, keeping in mind, that these are no metals but metal oxides [10, 30].

Unfortunately, nanoparticles are usually less stable than the bulk material. Consequently, one major task is to improve the catalysts' stability under these conditions. Concerning the stability of these catalysts, first, Pt-based ORR-catalysts shall be dealt with. The strength of the different degradation mechanisms depends on the electrochemical treatment and can occur parallel during fuel cell operation [8, 10, 31–33]:

- Pt dissolution: This is more favorable for smaller nanoparticles. Possible consequences include redeposition on bigger Pt particles (Ostwald ripening), or reduction to metallic Pt by molecular hydrogen in the membrane.

- detachment of Pt nanoparticles from the support

- loss of active Pt surface due to Ostwald ripening or agglomeration of Pt nanoparticles

- corrosion of the (carbon) support, that can lead to detachment of support with catalysts, or enhance nanoparticle detachment or agglomeration

- leach out of non-noble metals from Pt-based alloy nanoparticles and, consequently, reduction of the Pt mass specific activity

These findings were experimentally confirmed, for example with identical location TEM [10, 31, 32].

Analog considerations hold for OER catalysts, too: The dissolution of RuO2 and IrO_2 as well as the leach out of Ru from Ru-Ir-based mixed oxides was reported [9, 34]. The stability of the support is an important issue [10]. The Markovic group showed that the stability and activity trends for monometallic noble metal oxides as OER catalysts are adverse [35]. The Chorkendorff group could show that the stability as well as the activity of RuO_2 nanoparticles depends strongly on its surface pretreatment [36].

Some of the approaches to improve the catalysts stability arise from the description of the degradation mechanisms, for example the use of more stable support materials or alteration of the nanoparticles' morphology [37–39]. But there are also some interesting new approaches: Liu et al. reported that degradation of Pt nanoparticles on Indium Tin Oxide can be minimized via strong metal-support interaction [41, 42]. Also, doped graphene support improved the stability of Pt catalysts [43]. A positive influence of the support on the activity of OER nanocatalysts was also reported [10, 44–46].

The preparation of inhomogeneous catalyst surfaces e.g. by segregation or decoration of support particles with other particles opens new ways to further improve the catalysts properties, but also offers new challenges in understanding the underlying interaction mechanisms [15, 28, 29, 47–49]. The Adzic group achieved a stability improvement by decorating Pt nanoparticles with Au nanoparticles [14]. The Markovic group achieved stability improvements by nanosegregation of Ru-Ir-based metal oxides compared to the homogeneous mixed metal oxide [15].

In chapters 5 and 6, studies on the influence of a decoration of Ir nanodots on Pt nanorods and RuO_2 nanoparticles on the catalysts' stability towards ORR and OER are presented.

2.3 Influence of V Ions on the Stability of Pt Nanoparticles

Chapter 4 deals with the influence of a V contamination of the electrolyte on the stability of a Pt catalyst simulating VARFB conditions and more specifically with

the question, if V compounds deposit on the catalyst's surface. In a first step, the existing literature from similar research fields shall be reviewed based on [8].

The electrodeposition of V_2O_5 from a 3 mM V^{IV} solution is predicted by calculations to occur at pH values around 1.8 that are much higher than those in a VARFB. At different pH values, a higher V concentration is required to gain deposition of V_2O_5 or V^V compounds, and the precipitation takes place after the oxidation into another soluble V^V species [12]. Potiron et al. [12] deposited $H_{0.4}V_2O_{5.2-\delta}\cdot nH_2O$ with $0.04 < \delta < 0.2$ and $0 < n < 1.8$ from 0.1 M $VOSO_4$ electrolyte (pH 1.8) on a Pt electrode in an electrochemical quartz crystal microbalance (EQCM) setup. They postulated the necessity of oxygen evolution for the deposition of the V compounds, because oxidation of the V^{IV} species already started at 0.1 V vs. mercury / mercury sulfate electrode (MMSE), but deposition was only observed at potentials above 1.1 V vs. MMSE. Li et al. [13] deposited $VO_x \cdot nH2O$ compounds consisting of a mixture of V^{IV} and V^V oxy-/hydroxyl species from a 25 mM $VOSO_4$ solution (pH 2.7) on graphite substrates. Deposition was possible at much lower potentials above 0 V vs. MMSE, where no oxygen evolution occurs.

In the VARFB electrolyte that is H_2SO_4 in a concentration range of 2 M, the pH is much lower leading to a lower solubility of $VOSO_4$. The solubility of $VOSO_4$ in 3 M H_2SO_4 at 20°C is 1.8 mol l^{-1} [50, 51]. Studies on the stability of V-containing solutions without any electrochemical treatment show precipitation of V^{II}, V^{III}, and V^{IV} in 2 M vanadium solutions below 10°C, whereas precipitation of V^V was observed above 40°C. A higher H_2SO_4 concentration supports the precipitation of V^{II}, V^{III}, and V^{IV}, but leads to a stabilization of V^V in the solution. This is described by the equilibrium [52]

$$V_2O_5(s) + 2H^+ \rightleftarrows 2VO_2^+ + H_2O \tag{2.4}$$
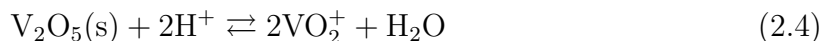
Moreover, the solubility and stability of V ions is affected by the anions in the solution [53].

In a VRFB a high V^V concentration occurs at the electrode during charging due to V^{IV} oxidation. If the local V^V concentration exceeds the solubility limit, deposition of V^V compounds is expected to take place. Deposition of vanadium oxides on carbon felt was reported in the positive half cell of the vanadium redox flow battery during operation, where the V concentration is a few moles per litre [11, 53].

The examples mentioned show that deposition of vanadium compounds strongly depends on conditions like the pH value and other factors. However, under conditions directly relevant to the VARFB, the question of V deposition was not examined in

detail yet.

Chapter 4 deals with the research question, if there is any influence of vanadium ions on the stability of platinum catalysts in a water/air electrode under conditions close to a VARFB. The degradation behavior of Pt nanoparticles was previously studied mainly in the field of proton exchange membrane fuel cells [31, 32, 54–57]. Studies showed that, in degradation treatments in a potential range above the oxygen reduction potential, Pt nanoparticle detachment is the dominant degradation process - likely due to carbon corrosion. In treatments at lower potentials, the main degradation mechanisms are nanoparticle migration and coalescence, Pt dissolution during oxygen reduction, and Ostwald ripening [32].

The studies presented in chapter 4 are based on Cyclic Voltammetry measurements in a three-electrode setup that enables the conditions to be simulated in the bifunctional reaction unit during operation, including contamination with V ions. Concerning the Pt electrode, we considered in a first step a bulk Pt electrode as relatively simple model system. EQCM measurements were performed at bulk platinum in order to investigate possible deposition of vanadium compounds and gain further insight into the processes occurring at the electrode surface. Closer to a real battery, the stability of Pt nanoparticles supported on Carbon (Pt/C) and the influence of V ions on it were examined in a second step and compared with the bulk system.

2.4 Stability of Bifunctional OER-ORR Catalysts

There are different options to design the oxygen electrode of a bifunctional reaction unit of a VARFB or a PEM URFC [17]. For example, the OER and ORR catalysts can be placed in different electrode layers optimized for each reaction. If both catalysts are placed in one layer, the nanoparticles can be physically mixed or colloidchemically prepared bifunctional OER-ORR catalysts can be used. This section reviews the state of the art as introduction to the studies on Pt-Ir-based bifuntional catalysts presented in chapter 5.

Several studies were conducted on this topic in the field of PEM URFC research [9,17,58–73]. Because of the poor stability of RuO_2, binary bifunctional catalysts are commonly based on Pt for ORR and IrO_2 for OER. The best round trip efficiency was commonly achieved using low amounts of Ir or IrO_2 [9,59,69,74]. In the literature it is reported that physical mixing of both catalysts does not lead to a good dispersion of the catalysts [59,73]. The colloidchemical synthesis of bifunctional catalysts for ORR and OER leads to a better dispersion and offers the possibility of synergistic effects.

So, mostly a better round trip efficiency of the colloidchemically prepared catalysts is reported compared to the mixed ones. Also in this research field, stability studies of the catalysts are rare. Kong et al. prepared Ir in the presence of IrO_2 and mixed it with Pt nanoparticles [61, 62]. After activation cycles that oxidized the Ir surface they performed accelerated potential cycling tests for ORR and OER separately. They apparently compared each one single measurement of mixed Pt/IrO_2 particles with mixed $Pt/Ir-IrO_2$ particles. In the latter case, the stability of the IrO_2 did not change while the Pt stability increased. Papazisi et al. prepared $Pt_xIr_{1-x}O_2$ mixed oxide nanoparticles and studied the degradation of the OER currents during 180 cycles between OER and hydrogen evolution potentials. The OER currents of the pure IrO_2 decreased to 82 % of the initial value while it decreased to 86 % for $Ir_{0.8}Pt_{0.2}O_2$ and to 60% for $Ir_{0.2}Pt_{0.8}O_2$ [74]. There are no studies known to the author, that compare the stability of Pt-Ir-based nanoparticles with the single Pt and Ir based catalysts under URFC conditions, meaning under simulated charge-discharge cycles that include ORR and OER potentials. It is known that such a treatment is harsher than single ORR or OER protocols [8, 31]. This is explained by the degrading effect of repeated build up and reduction of an (hydr)oxide layer on the Pt surface [8].

In the studies presented in chapter 5, Pt nanorods, that are known to exhibit an excellent stability compared to Pt nanoparticles under ORR cycling tests [37–39], were prepared and decorated with Ir nanodots. The stepwise synthesis allows a higher control over the morphology of the nanoparticles and, thus, their activity and stability. Structural measurements are performed with XRD and TEM. The OER and ORR stability of the Ir decorated Pt nanorods (Ir@Pt) is studied via Cyclic Voltammetry in comparison to unsupported Ir nanodots and pure Pt nanorods.

2.5 Stability of Oxygen Evolution Catalysts

Since the conditions during charge (meaning OER) in the oxygen electrode of a VARFB (or PEM URFC or PEM water electrolyzer) are known to be harsh due to the acidic environment and the high potentials [40], one major challenge is to improve the OER nanocatalyst's stability. In this section, the current research is reviewd prior to the studies on Ir-decorated RuO_2 nanoparticles presented in chapter 6.

RuO_2 is generally recognized as one of the OER catalysts with the highest activity [34–36]. Unfortunately, RuO_2 is oxidized to RuO_4 under OER conditions in acidic media, that dissolves into the electrolyte [9, 34, 36, 75–77]. IrO_2 does not show the high catalytic activity of RuO_2 but a higher stability [15, 49, 59, 78, 79]. In order to

increase both the activity and stability of noble metal based OER catalysts, studies on Ru-Ir mixed oxides were conducted [9, 15, 34, 59, 77, 78]. Koetz et al. observed a significantly higher stability and an inhibition of RuO_4 production on sputtered Ru-Ir mixed oxides during OER conditions [77] while there is only a small loss of activity. This behavior can already be observed for small amounts of Ir. It is suggested that a common electronic d-band is formed that allows the electron transfer from Ru sites to Ir sites and, thus, mitigating Ru oxidation. Danilovic et al. showed for the bulk and the nanoparticle form that nanosegregated Ru-Ir mixed oxides possess a similar activity but a 3 to 4 times higher stability compared to homogeneous Ru-Ir mixed oxides [15]. They observed a surface enrichment of Ir in the nanosegregated samples and explained the higher stability with the higher stability of surface Ir compared to Ru [15]. Audichon et al. prepared $Ir_xRu_{1-x}O_2$ nanoparticles and tested the performance and stability in an electrolyzer cell. $Ru_{0.9}Ir_{0.1}O_2$ had a smaller overpotential and a higher stability compared to pure RuO_2 [80].

The aim of the studies presented in chapter 6 is to decorate RuO_2 nanoparticles with Ir nanodots that are oxidized to IrO_2 later on, at least at the surface, and to compare the stability of both single nanoparticle catalysts and the composite catalyst. The advantage of this stepwise approach is the possibility to control more easily the morphology and thus activity and stability of both nanoparticle species compared to the synthesis of an alloy or mixed oxide. Moreover, this approach leads to a reduced amount of expensive Ir needed compared to mixed oxides.

3 Experimental Methods

This chapter aims at shortly introducing the necessary theoretical background for the experimental methods, giving references for further information and illustrating the experimental setups and procedures.

3.1 Nanoparticle Synthesis

There are several physical and chemical methods, to prepare nanoparticles [81, 82]. One popular method to synthesize metal based nanoparticles, is to dissolve metal salts in a liquid and to reduce the metal cations by an reducing agent. As long as the solution is supersaturated with metal atoms, they will form nanoparticles, that are stable above a critical size. This colloidchemical nanoparticle synthesis can ideally be described as consisting of three stages: seed formation, particle growth and termination. Usually, organic molecules can act as ligands, that bind to the nanoparticles' surface and, thus, prevent agglomeration. The nanoparticles' morphology depends on the material as well as on the ligands and the reaction velocity of the synthesis. The latter depends on the concentration evolution of the metal atoms, that is influenced by the kind and concentration of metal salt, by the temperature, the reducing agent, the solvent and gases dissolved in it. Usually, the nanoparticle dispersion is centrifuged, the supernatant is decanted and the solids are redispersed in another solvent in order to eliminate the contamination of the nanoparticle dispersion with undesired chemicals from the synthesis. More information can be found in [81, 82].

3.1.1 Synthesis of Pt Nanorods

The synthesis of the Pt nanorods is based on the synthesis of Sun et al. [37–39] 32 mg $H_2PtCl_6 \cdot 6H_2O$ and 1 ml formic acid were simultaneously added to 20 ml ultrapure water at room temperature. The reduction of the Pt to metallic nanoparticles can be described by the following reaction equation [38]:

$$H_2PtCl_6 + 2HCOOH \rightarrow Pt + 6Cl^- + 6H^+ + 2CO_2 \qquad (3.1)$$
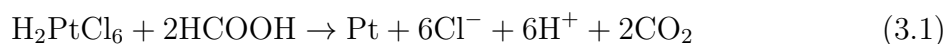
Within one day, turbidity of the solution due to black precipitates could be observed along with decoloration of the formerly yellow solution due to the consumption of Pt ions. The synthesis turned out to be robust against changes in the concentrations of the chemicals. After the synthesis, the dispersion was filled in a centrifuge tube and diluted with isopropanol. The centrifugation was usually performed for five

minutes at around 5,000g. The supernatant was decanted and the nanoparticles were redispersed in isopropanol by ultrasonication for five minutes. The centrifugation / redispergation procedure was performed two times.

3.1.2 Synthesis of Ir Nanodots

The polyol-process based synthesis of Ir nanodots was adapted from Kong et al. [60–62]. The ethylene glycol, that served as solvent, reacts to a reducing agent at temperatures around 140°C. The process can be described by the follwoing reaction equations:

$$C_2H_4(OH)_2 \rightarrow CH_3CHO + H_2O \tag{3.2}$$

$$2M^+ + 2CH_3CHO \rightarrow 2M + CH_3(CO)_2CH_3 + 2H^+ \tag{3.3}$$

The synthesis was performed without support particles as well as in the presence of previously synthesized Pt nanorods and commercially available RuO_2 nanoparticles (Johnson Matthey) as support. Changes in the concentration of the chemicals did not alter the morphology of the nanodots. Ethylene glycol, $IrCl_3 \cdot n\ H_2O$ (58 wt% Ir, Johnson Matthey), isopropanol, 0.5 M NaOH if applicable, and support particles if needed were filled into a flask and stirred under Ar atmosphere for several minutes. Then the flask was immersed into an oil bath heated to 140°C under Ar flow. Three minutes after the immersion, the liquid lost the yellow color accompanied by a turbidity meaning the consumption of Ir ions as well as the formation of nanoparticles. During the syntheses using support particles, this is harder to observe, but can easily be controlled after centrifugation. Afterwards, the dispersion was filled into a centrifuge tube and diluted with isopropanol. The centrifugation was at least performed for five minutes at around 5,000g. The supernatant was decanted and the nanoparticles were ultrasonically redispersed in isopropanol for five minutes. The centrifugation / redispergation procedure was performed two times. Unsupported Ir nanodots were synthesized with varying Ir salt concentrations (20, 40, 60 and 80 mg $IrCl_3 \cdot n\ H_2O$). 10 ml ethylene glycol served as solvent. The immersion time of the flask in the oil bath was 10 minutes.

The Ir decoration of Pt nanorods was performed similar to the synthesis of pure Ir nanodots. 1 ml of Pt nanorods dispersed in isopropanol and 8 mg Ir salt were added to 9 ml ethylene glycol. For comparison, a synthesis without Ir salt was also conducted. The cleaning procedure was performed five times.

For the synthesis of Ir nanodots in the presence of RuO_2 nanoparticles, 20 ml ethy-

lene glycol with 12.5 mM NaOH were used as solvent and 20 mg RuO_2 were added. The amount of Ir salt was varied between 0 and 100 mg. The part of Ir nanodots that did not deposit on the support particles could be reduced to a negligible concentration compared to the RuO_2-supported Ir nanodots by centrifugating, decanting and redispersing it six times.

3.2 Transmission Electron Microscopy (TEM)

Transmission electron microscopy (TEM) is one of the most important techniques for the structural investigation of nanoparticles. It was developed in the 1930s by Max Knoll and Ernst Ruska, who was honored with the Nobel prize in physics in 1986. Since the electron's de Broglie wavelength λ is coupled on the acceleraton voltage of an electron source U via its momentum p, sufficiently high acceleration voltages enable microscopic images with a resolution far better than in conventional light microscopy, that is limited by the Rayleigh criterion to a spatial resolution near to the used wavelength λ [83–85]. With

$$\lambda = h/p \tag{3.4}$$

$$E = E_{kin} + E_{rest} \tag{3.5}$$

$$= eU + m_{e0}c^2 \tag{3.6}$$

$$E^2 = p^2c^2 + m_{e0}^2c^4 \tag{3.7}$$

the wavelength of electrons with relativistic velocity can be described as

$$\lambda = \frac{h}{\sqrt{2Ume(1 + \frac{eU}{2mc^2})}} \tag{3.8}$$

with the Planck constant h, the light velocity c, the elementary charge e, the electron's rest mass m_{e0} [86].

For an acceleration voltage of U=300 kV the electron's wavelength is λ=2 pm. In reality, the TEM resolution is much worse. This is due to lens errors. The most common errors are

- spherical aberration, meaning that the focal length of an electron lens depends on the incident angle of the electrons into the lens or in other words on the distance of the electron's to the center of the lens

- chromatic aberration, meaning that the focal length depends on the electrons'

wavelength. The energy distribution of the electrons leads to a wavelength distribution and, thus, to a decrease in resolution.

- astigmatism, meaning that due to asymmetries of the lens the focal length of a lens can vary as function of the position (or incident angle) in the lens' x-y plane, in which an electron beam propagating in z direction passes the lens.

Fig. 3.1 shows a schematic drawing of a typical TEM setup. The electron source is usually a heated field emission electrode. In the electron gun the electrons are accelerated. The condensor system consists of 2, 3 or more lenses and apertures to ensure a high quality of the electron beam. The objective lense consists of two parts. Between both, the sample is positioned. Since the objective lens has the highest opening angle or in other words is the most important lens for magnification, its lens errors are crucial for the resolution. Afterwards there are some lenses and apertures to magnify the image or the diffraction pattern or parts of it onto a detector or screen.
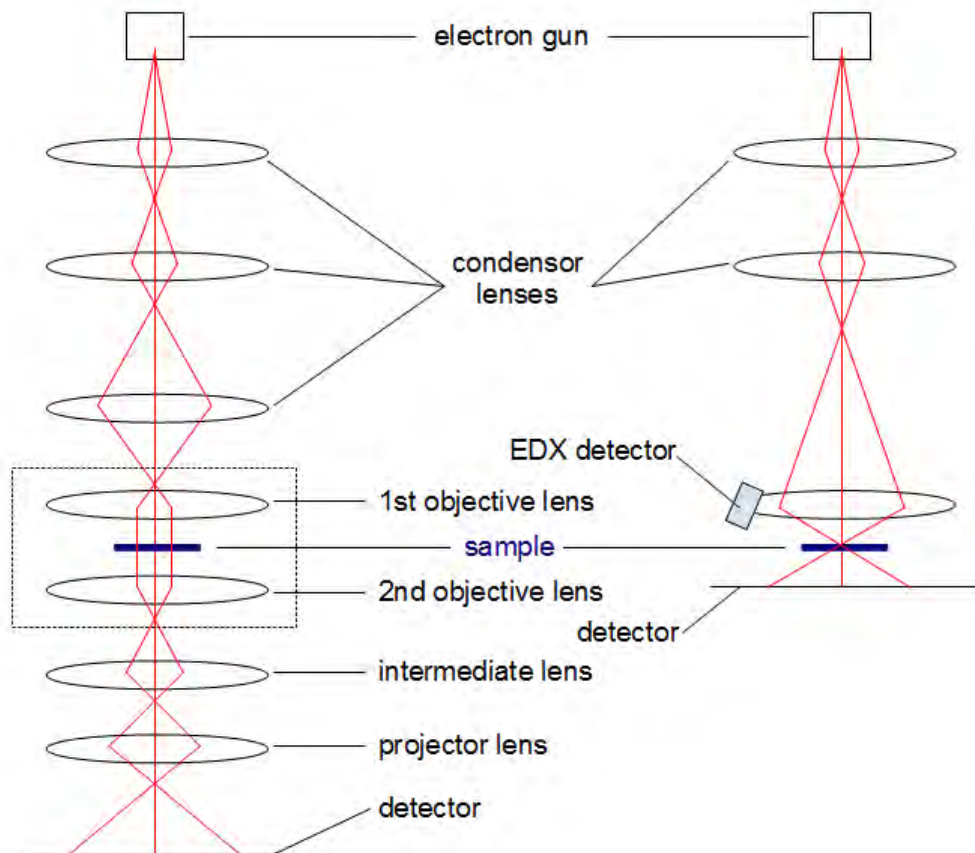
Figure 3.1: *Schematic drawing of a typical TEM setup in TEM mode (left) and STEM mode (right) with EDX detector. The beam path is schematically illustrated in red. Apertures are excluded for the sake of simplicity. This image is inspired by [83–85].*

While in TEM mode the electron beam passes the sample's region of interest parallel to the optical axis of the TEM, in scanning TEM (STEM) mode the electron beam is focused on the sample. The spot on the sample has usually a sub-nanometer diameter. The scanning of the sample with the electron beam is conducted via deflection coils. In STEM mode the recording of EDX spectroscopic maps of the lateral element distribution can be conducted.

TEM images and EDX spectroscopic data were collected on a Jeol 2010F system with an acceleration voltage of 200 kV. The image analysis was performed with the software ImageJ. The sample preparation was conducted by dropping an aliquot of the nanoparticle dispersion on Cu TEM grids. Depending on the desired resolution and the atomic number of the elements in the sample, the sample has to be thin. In case of nanoparticles, the dispersion should be not too concentrated and the agglomerates should be not too big. To perform TEM measurements on nanoparticles, that had experienced a stability protocol before (see chapter 3.5.2), the electrode coated with particles was ultrasonicated in ethanol to redisperse the particles. The dispersion was then dropped on TEM grids. For comparison, nanoparticles were deposited on the electrode, exposed to the electrolyte without conducting a stability protocol and redispersed as described above.

3.3 Energy Dispersive X-Ray (EDX) Spectroscopy

Energy dispersive X-ray (EDX) spectroscopy is an element specific spectroscopy method. Electrons are excited from lower atomic orbitals of the sample material by high energy electrons of the TEM's electron beam. Electrons from higher atomic orbitals relaxate into this vacancy and emit X-ray photons with the energy that is characteristic for specific elements and transitions (Tab. 1). EDX spectra show the X-ray intensity as function of the X-ray photons' energy (Fig. 3.2). In EDX spectra a continous background is visible that is due to the so called Bremsstrahlung. It originates from the deceleration of electrons from the electron beam in the sample.

The denomination of EDX peaks (Tab. 1) is defined by the following rule: The letter (K,L,M, ...) denotes the initially ionized atom shell, the greek letter α stands for the relaxation of an electron into this vacancy from the next higher shell, while β stands for relaxation from a shell that it two principal quantum numbers higher. The number (1,2, ...) depends on the change of the azimuthal quantum number of the transition [84, 85, 87].

Fig. 3.2 shows a typical STEM image and EDX sum spectrum of an agglomerate of Ir decorated RuO_2 after an electrochemical stability protocol. EDX spectra were

Element	Atomic Number	$K_{\alpha 1}$ [keV]	$L_{\alpha 1}$ [keV]	$M_{\alpha 1}$ [keV]
O	8	0.525		
Cu	29	8.048	0.930	
Ru	44	19.279	2.559	
Ir	77	64.90	9.175	1.980
Pt	78	66.83	9.442	2.051

Table 1: *X-ray energy for selected transitions of selected elements [87].*

recorded in STEM mode. The agglomerates have a typical diameter in the range of a few hundred nanometers. The copper (Cu) signal in the EDX spectrum originates from the TEM grid, that is made of Cu. The Sulphur (S) signal results from the sulphuric acid solution in which the stability protocol was conducted.
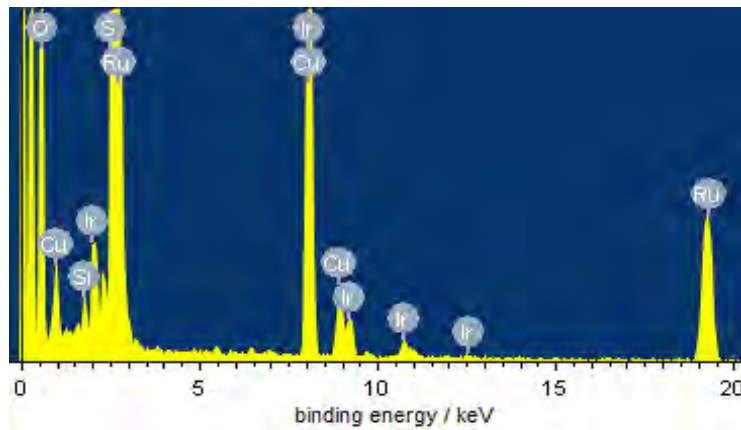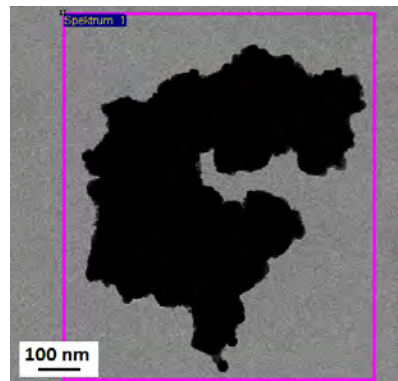
Figure 3.2: *STEM image (top) and EDX spectrum (bottom) of an agglomerate of Ir decorated RuO_2 after the stability protocol. The EDX spectrum was recorded as sum spectrum of the marked area in the image.*

By analyzing the peak intensities, it is possible to determine quantitavely the fraction of certain elements in a sample. For elements with an atomic number above 10 the detection limit is in the range of 0.1 to 0.2 weight percent [84, 85, 87]. To determine the Ir:Pt and Ir:Ru atomic ratio via EDX, sum spectra of 10 agglomerates were

collected and the ratios were averaged.

3.4 X-Ray Diffraction (XRD)

Powder X-ray diffractrometry is a common method to study the structural properties
of nanoparticles. X-ray diffraction (XRD) is a method based on the work of Max
von Laue from 1912 and was first confirmed by Walter Friedrich and Paul Knipping.
Von Laue was honored with the Nobel prize for physics in 1914. William Henry
Bragg and William Lawrence Bragg used this method to study the crystal structure
of e.g. NaCl and Calcite and got for that research the Nobel prize for physics in
1915 [84, 88].

As all radiation can be diffracted by periodic structures in the order of magnitude of
the radiation's wavelength, X-ray diffraction is an adequate method to investigate
the structure of crystals, since its wavelength is usually in the Angstrom range. It
can be described by the Bragg equation:

$$n\lambda = 2dsin(\theta) \tag{3.9}$$

n describes the order of the interference maximum, λ is the wavelength of the ra-
diation, d is the lattice spacing. θ is the angle between the beam and the lattice
planes. The path difference is 2 δ with $\delta = d\ sin(\theta)$. The equation describes, that
constructive interference of radiation diffracted on two lattice planes occures, when
the path difference is a multiple of the wavelength. This is illustrated in Fig. 3.3.
With known wavelength and angles the crystal structure can be investigated [84, 88].
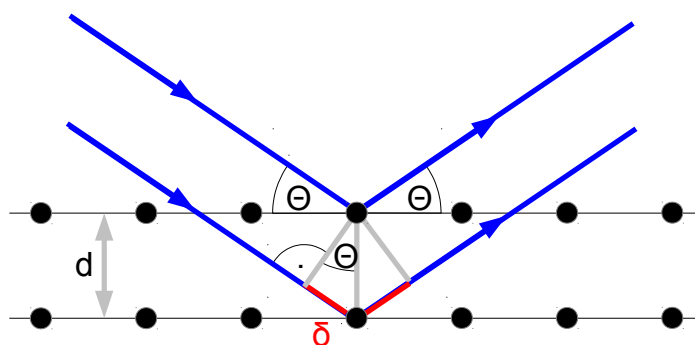
Figure 3.3: *Schmeatic illustration of Bragg's law. The incident and diffracted beam
are blue. The path difference δ is red. The atoms are shown as black
dots. The thin lines represent the lattice planes.*

Powder diffractometry uses the assumption, that crystallites are randomly oriented

in the sample. In the Bragg-Brentano geometry one point-like X-ray source and one point like X-ray detector are used. This method allows relatively fast measurements. During the recording of a X-ray diffractogramm in the θ-θ geometry the X-ray source and the detector are moved in opposite directions on a semi circle with a flat sample in the center (Fig. 3.4). In other words, the source produces an incident beam falling onto the sample under the angle θ and the detector collects the diffracted beam under the same angle [88].
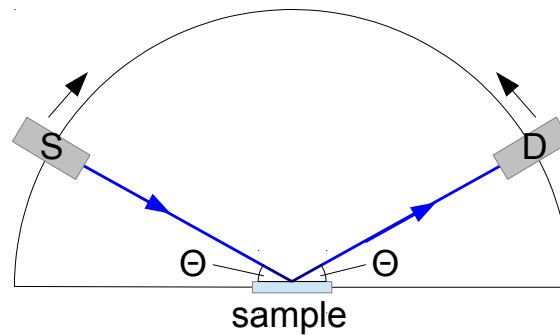
Figure 3.4: *Schematic illustration of a XRD setup in the Bragg-Brentano geometry. S denotes the X-ray source, D the detector. During the θ-θ scan both move in opposite directions as described in the text. Apertures are excluded for the sake of simplicity.*

In the X-ray tube electrons are accelerated onto a target (in most cases copper (Cu)). The electrons are partly slowed down in the target leading to emission of X-Rays with continous wavelengths (so called Bremsstrahlung). Another part ionizes the atoms in the lower orbitals. Electrons fall in these vacancies and emit characteristic X-Ray radiation - typically K_β, $K_{\alpha 1}$ and $K_{\alpha 2}$ radiation. The Bremsstrahlung and the K_β radiation are attenuated by a metallic filter (in case of Cu target typically nickel (Ni)). The $K_{\alpha 1}$ and $K_{\alpha 2}$ radiation are used for the XRD measurements. They have the wavelengths $\lambda_{\mathrm{CuK\alpha 1}}$= 0.15406 pm and $\lambda_{\mathrm{CuK\alpha 2}}$= 0.15444 pm and an intensity ratio of about 2:1 [88]. Apertures are used to ensure an adequate divergence of the beam. An automatic divergence slit is used to keep the illuminated area of the sample constant for all θ. A linear detector with 255 channels along 3.3° 2θ was used.

The measured data are displayed as a diffractogram, meaning the X-ray intensity is shown as function of 2θ. Since the XRD patterns result from diffraction of the X-ray beam at the sample's lattice, changes of the latter influence the diffractogram. Vice versa one can draw conclusions from the diffraction data to the lattice structure. If the lattice, for example, experiences compressive strain the associated reflex will

shift to higher values.

It is possible, to estimate the crystallites' mean diameter from peak width of the XRD reflexes under certain assumption. In X-ray diffraction there are several line broadening mechanisms. One is due to the measurement setup and can be determined with reference samples. Another mechanism is due to the finite size of crystallites. If the particles are not monodisperse, the variation of the size additionally broadens the peak. Moreover, inhomogeneous strain within one particle or varying strain in different particles of the sample leads to a line broadening since it leads to a variation of the lattice spacings. In these studies the mean crystallite diameters for Pt nanoparticles, Ir nanodots and RuO_2 nanoparticles was estimated via Scherrer equation assuming quasi-spherical, monodisperse nanoparticles, that are not inhomgeneously strained [89, 90]. Using these simplifying assumptions, the Scherrer equation describes the relation between the crystallites' diameter d and the full width at half maximum b of a XRD peak with a maximum at θ for a given X-Ray wavelength λ:

$$d = \frac{k\lambda}{b\ cos(\theta)} \tag{3.10}$$

The Scherrer constant k is a dimensionless number, that is usually a value near unity. The author used k=0.9 assuming quasi-spherical particles.

XRD data were collected using a PANalytical X'Pert Pro diffractometer operating with Cu-Kα radiation in Bragg-Brentano θ-θ-geometry, using an automatic divergence slit. Samples were prepared by dropping the dispersion on low background silicon sample holders. Reference data were taken from the data base of the International Centre for Diffraction Data (ICDD). A linear background was subtracted prior to further analysis. A peak broadening due to the instrument was corrected by subtracting 0.08° from the full width at half maximum.

The structural behavior of nanoparticles after certain annealing procedures was studied using the high temperature XRD chamber HTK 1200N from the company Anton Paar. The heating element installed was a Kanthal APM (Cr: 22%; Al: 5.8%; Fe: rest) and the thermocouple was a Pt-10%Rh-Pt sensor with a measuring inaccuracy of ±2K. The chamber could be purged with Ar gas or synthetic air. Fig. 3.5 shows the annealing procedure schematically. First, the XRD pattern of the sample was recorded at room temperature (A). Then, the sample was annealed with a heating rate of 60 K/min to 100°C (B). After an equilibration time of 30 min, a XRD pattern was recorded (C). Since the data acquisition lasts 5.5 h the sample was hold at the elevated temperature for 6 h. Then, the samples was cooled down

with 50 K/min to room temperature (D) and after an equlibration time of 30 min, a further XRD pattern was recorded (A2). This procedure was repeated with the same parameters for annealing temperatures of 200°C, 300°C and 400°C.
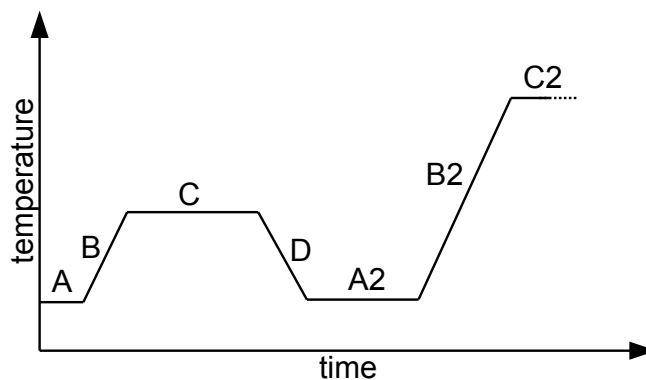
Figure 3.5: *Scheme of the annealing procedure.*

The XRD patterns recorded at room temperature were taken for further analysis. This has two reasons: first, the crystals' lattice expands with rising temperature leading to a peak shift to lower angles. The comparison of XRD patterns recorded at different temperatures is, thus, more challenging - and in this case easily avoidable. Secondly, when the temperature rises, the sample holder expands leading to an inaccurate positioning of the sample and, consequently, to a shift of the XRD features. These so called height errors can be compensated. But it seems more secure to the author, to use room temperature diffractograms, since there is no obvious advantage in analyzing the high temperature diffractograms.

3.5 Cyclic Voltammetry

Since the electrochemical stability studies in this work are based on cyclic voltammetry, this method and the expermental design shall be introduced.

3.5.1 Theoretical Background

Cyclic voltammetry is one of the most popular methods to study electrochemical processes: a potential on a working electrode is varied with a constant potential sweep rate between a lower and an upper potential limit and the current response is measured (Fig. 3.6). The results are shown as potential-current diagramm, the so called cyclic voltammogram (CV).
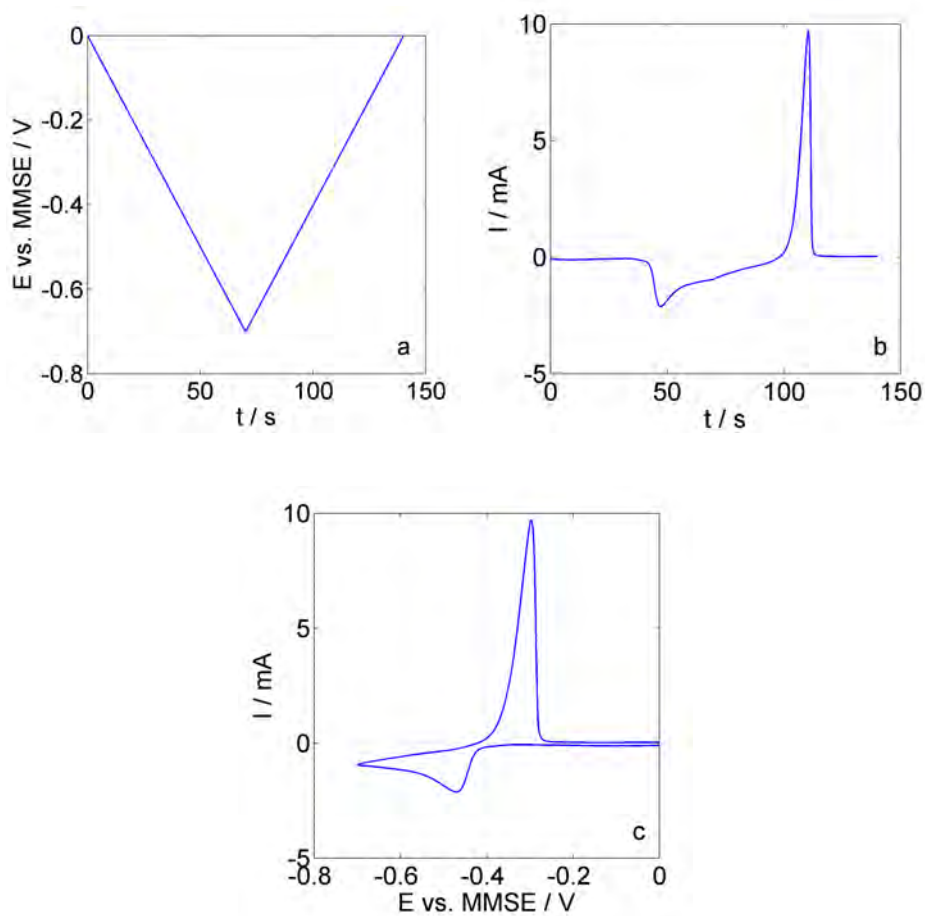
Figure 3.6: *Potential as function of time (a), current response as function of time (b) and the CV (c), meaning current as function of the potential of a cyclic voltrammetry measurement on a Pt electrode in 0.2M K_2SO_4 with 10mM $CuSO_4$ with a scan rate of $\nu=10$ mV s^{-1}. The CV shows reduction of Cu^{2+} to metallic Cu and dissolution of the electrodeposited Cu to Cu^{2+}.*

The basics of cyclic voltammetry will shortly be introduced. For further information the books of Derek Pletcher [91,92], Hamann and Vielstich [93] as well as Bard and Faulkner [94] are recommended.

The correlation between a potential E on an electrode and the concentrations of the oxidized and reduced form of a redox species c_O and c_R in a currentless steady state are described by the Nernst equation:

$$E = E^0 + \frac{RT}{nF} ln \left(\frac{c_O}{c_R} \right) \qquad (3.11)$$

with the formal potential E^0, the universal gas constant R, the temperature T, the

number of tranferred charges per redox reaction n, and the Faraday constant F. As described by the equation, the potential depends on the concentration ratio of the oxidized to the reduced form of the redox couple. Vice versa, by applying a potential at the electrode an according concentration ratio arises at the electrode.

The overall charge transfer at the electrode for the reduction/oxidation of a redox species as function as the applied overpotential η compared to the equilibrium potential is for low overpotentials, meaning no diffusion limitation, described by the Butler-Volmer equation. The anodic current j_a (for the oxidation), the cathodic current j_c (for the reduction) and the resulting overall current j (Butler-Volmer equation) are [91, 93]:

$$j_a = j_0 \ exp\left(\frac{\alpha nF}{RT}\eta\right) \tag{3.12}$$

$$j_c = -j_0 \ exp\left(-\frac{(1-\alpha)nF}{RT}\eta\right) \tag{3.13}$$

$$j = j_a + j_c \tag{3.14}$$

$$j = j_0 \left[exp\left(\frac{\alpha nF}{RT}\eta\right) - exp\left(-\frac{(1-\alpha)nF}{RT}\eta\right)\right] \tag{3.15}$$

The exchange current j_0 is the current for the reduction/oxidation for the equilibrium potential, where both currents compensate each other. While j_0 describes the slope for both the anodic and cathodic current, the transfer coefficient α describes the ratio of the reaction velocities or, in other words, of the slopes of the cathodic and the anodic current (Fig. 3.7).
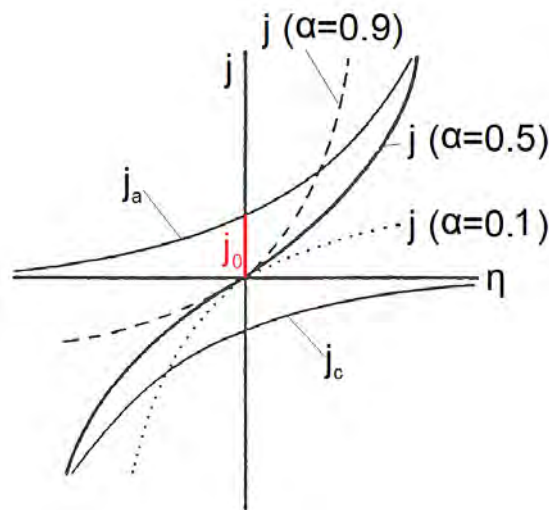
Figure 3.7: *Illustration of the anodic and cathodic current j_a and j_c and the overall current, of j_0 and of the influence of α according to the Butler-Volmer equation. The image was adapted from [93].*

For simple electrode reactions, the sum of the transfer coefficients for the cathodic and the anodic reaction is unity and, thus, instead of two constants only one is necessary using α for the anodic current density and (1-α) for the cathodic one. Commonly, α is close to 0.5 [91, 93].

With rising current the influence of the diffusion of the redox species on the current density increases and finally limits the current density. For example, if a positive overpotential is applied on the electrode in a solution containing the reduced form of a redox species, 'Red', and the overpotential is high enough, the concentration of 'Red' drops to nearly zero at the electrode's surface. A concentration gradient to the bulk solution appears and leads to a diffusion driven current. According to Fick's 1. law, the diffusion driven current j of a species is defined by the concentration gradient $\frac{dc}{dx}$ and the diffusion constant D:

$$j = -D\frac{dc}{dx} \tag{3.16}$$

Fick's 2. law describes the changes of the concentration in a volume element over time as difference between the currents flowing into that volume element and flowing out of it:

$$\frac{\partial c}{\partial t} = D\frac{\partial^2 c}{\partial x^2} \tag{3.17}$$

Morevoer, the consumption of 'Red' (with the concentration c_R and the diffusion constant D_R) at the electrode (x=0) equals the production of the oxidized form 'Ox' (with the concentration c_O and the diffusion constant D_O) and the electrical current:

$$\frac{j}{nF} = D_R \left(\frac{\partial c_R}{\partial x} \right)_{x=0} = -D_O \left(\frac{\partial c_O}{\partial x} \right)_{x=0} \tag{3.18}$$

With the help of these equations one can describe the current after a potential step as function of the time via the Cottrell equation [91]:

$$j = \frac{nFD^{1/2}c_R}{\pi^{1/2}t^{1/2}} \tag{3.19}$$

Fig. 3.8 illustrates the evolution of the concentration profiles of the redox species as function of distance from the electrode for dfferent points of time after a potential step to an oxidizing potential. The corresponding current transient is also shown. With increasing time the diffusion layer propagates into the bulk solution leading

to a decrease of the concentration gradient and, thus, of the current.
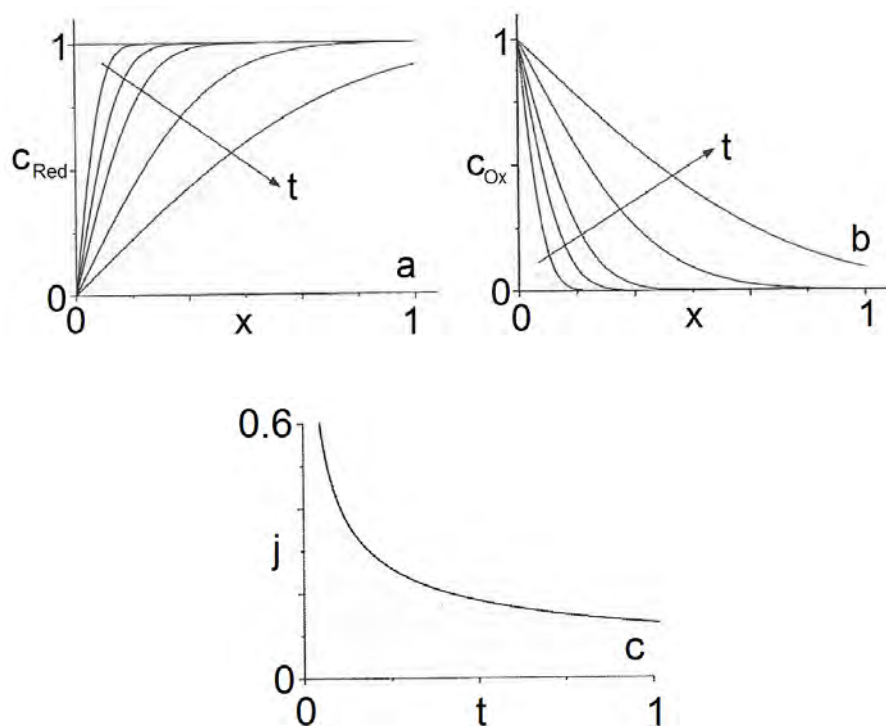
Figure 3.8: *Schematic concentration profiles of the reduced (a) and oxidized form of a redox species (b) as function of the distance from the electrode for different points of time after an oxidizing potential step. Corresponding current transient as described by the Cottrell equation (c). With increasing time the concentration gradient decreases leading to a decline of the current. The images were adapted from [91].*

Fig. 3.9 illustrates the evolution of the concentration profiles and, thus, the current during an anodic scan of a cyclic voltammogram. At the beginning, the current increases exponentially, but later the influence of the diffusion increases and leads to the peak maximum and the decrease of the current.
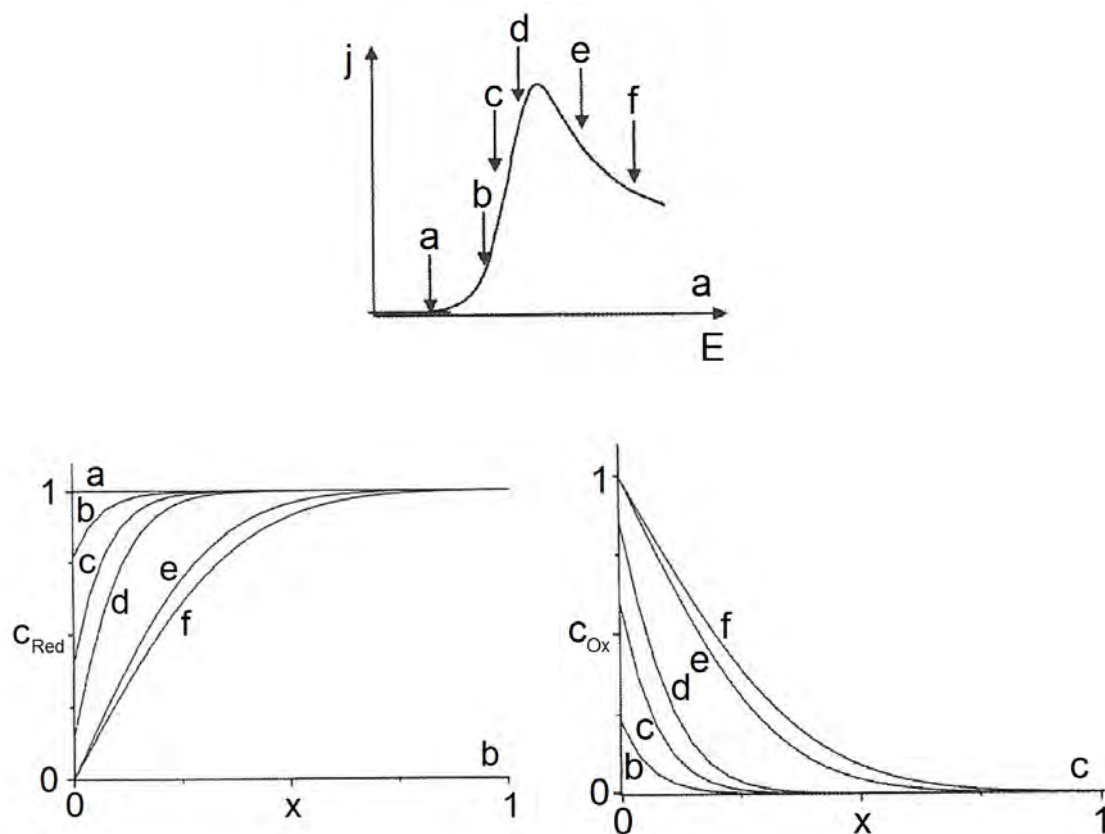
Figure 3.9: *Evolution of the current density (a) and the concentration profiles of the reduced (b) and the oxidized form of a redox species (c) during the anodic scan of a CV. The concentrations are normalized to their maximum. x describes a dimensionless distance from the electrode surface. The concentration profiles after different time steps (a-f) illustrate the interplay of electrode kinetics and diffusion: the concentration gradient at the electrode is steeper at time step d compared to time step f leading to a higher current at d compared to f. The images were adapted from [91].*

A different case is the oxidation/reduction of surface bound species (Fig. 3.10). Since the total amount of redox species is bound to the surface, the redox current drops to zero when all redox species are reduced or oxidized. The shape of the signal depends on the surface including inhomogeneities and possible interaction between the surface bound species. If there is an overpotential for reduction and/or oxidation, the oxidation peak will shift to higher potentials and/or the reduction peak will shift to lower potentials (case b in Fig. 3.10).
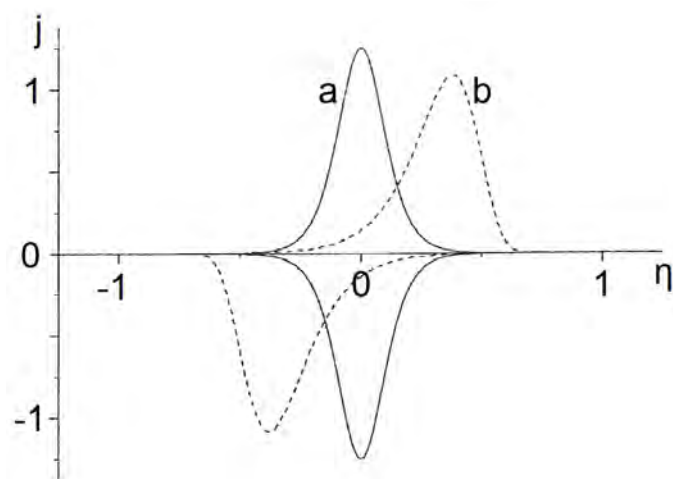
Figure 3.10: *Schematic CV of a surface bound species without overpotentials for reduction and oxidation (a) and with overpotentials (b). The image was adapted from [91].*

Fig. 3.11 shows a CV of a Pt electrode in 2M H_2SO_4 with a scan rate of ν=100 mV s$^-$1.
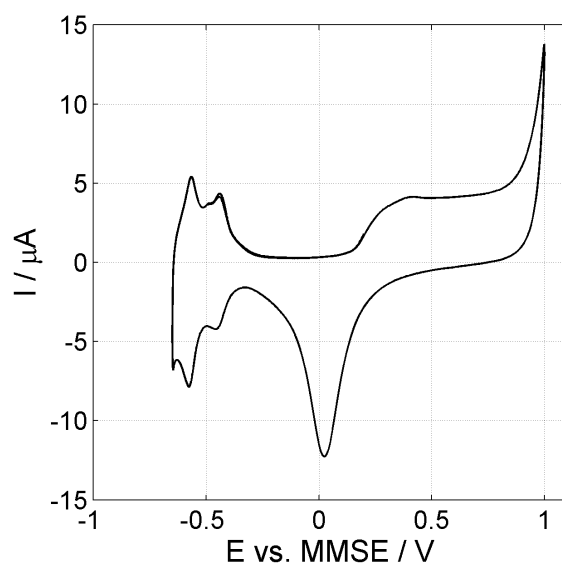
Figure 3.11: *CV of a bulk Pt electrode in 2M H_2SO_4. Scan rate: 100 mV s^{-1}.*

In the low potential regime (below -0.3 V vs. MMSE), the adsorption and desorption of hydrogen leads to the typical features for surface bound species. In the potential range between ca. -0.2 V vs. MMSE and 0 V vs. MMSE of the anodic scan the CV is featureless. In this so called double layer region the only contribution to the CV is due to capacitive currents, meaning the build up or decrease of the electrostatic double layer. If the potential is increased above 0.2 V vs. MMSE, the oxidation

of water to surface bound hydroxide and at higher potentials oxide leads to anodic currents. At potentials above 0.9 V vs. MMSE the surface oxide occupancy of the surface is high enough to lead to the evolution of molecular oxygen (oxygen evolution reaction, OER). With decreasing potentials, (hydr)oxide is reduced to water leading to the ORR (oxygen reduction reaction) peak at around 0 V vs. MMSE.

In cyclic voltammetry, the current leads due to a finite ohmic resistance of the system to a potential drop, the so called iR drop, that can distort the real applied potential on the working electrode. To handle this problem, it is useful to work with a so called three electrode setup, including a working electrode, a reference electrode and a counter electrode. While the working electrode is the electrode of interest, the potential at this electrode is applied versus a reference electrode having a fixed potential. The counter electrode provides the charges according to the working electrode to keep the charge neutrality of the system - or in other words it closes the ionic-electrical circuit through the working electrode [91–95].

Since the iR drop depends on the current and on the amount of the ohmic resistance of the solution, it is useful to work with low currents, with highly conducting electrolytes (e.g. acids with a concentration in the order of 1M) and small distances between the working electrode and the reference electrode. To avoid shading effects of the reference electrode, so called Haber-Luggin capillaries can be applied, that have a small diameter at the end, that is placed near to the working electrode. Moreover, electronic iR compensation can be applied. Here, the estimation of the solution's ohmic resistance and subsequent correction of the potential applied on the working electrode is conducted by the potentiostat [91–95].

3.5.2 Experimental Setup

The cyclic voltammograms (CVs) were recorded in an undivided three-electrode setup with 2 M H_2SO_4 electrolyte, that was purged with N_2. A Pt wire served as counter electrode. Potentials were measured against a mercury/mercury sulfate electrode (MMSE), and a CH Instruments potentiostat was used (Fig. 3.12). All measurements were conducted at room temperature. Electrochemical measurements of bulk platinum were performed on a previously polished Pt working electrode (2.0 mm^2 surface area). For measurements on nanoparticles the nanoparticle dispersion were ultrasonicated for 15 minutes. The dispersion was dropped onto a previously polished glassy carbon electrode (7.1 mm^2 surface area) and air-dried in the vent hood.
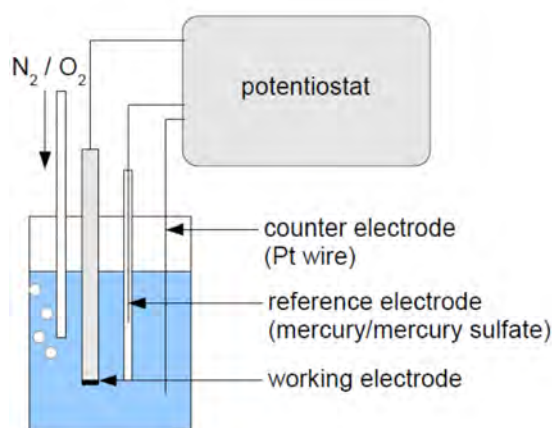
Figure 3.12: *Scheme of the cyclic voltammetry setup.*

To enable TEM measurements on particles after the stability protocol a measurement cell with a 1x1 inch^2 (6.45 cm^2) glassy carbon working electrode prepared with nanoparticles, a MMSE and a Pt coil counter electrode were used. iR compensation was applied [95]. After the protocol, the electrolyte was removed and the cell was repeatedly rinsed with water. Afterwards, the particles were removed from the electrode and dropped on the TEM grids as described in chapter 3.2.

3.5.3 Studies on the Influence of V Ions on the Stability of Pt/C

For the studies on the influence of vanadiums on the stability of Pt/C, commercially available Vulcan XC-72R carbon-supported Pt nanoparticle powder (40 wt% Pt/C, Sigma Aldrich) was used. The nanoparticle dispersion consisted of 2.5 mg of this Pt/C powder, 2 ml deionized water and 0.5 ml isopropanol.

Prior to the first measurement, the bulk Platinum and the Pt/C working electrode were electrochemically cleaned in 2 M H_2SO_4 by cycling it between -0.7 and 1.1 V vs. MMSE with 0.5 V s^{-1} starting and ending at 0.2 V vs. MMSE. To characterize the electrode, CVs were recorded between -0.65 and 1.0 V vs. MMSE with 0.1 V s^{-1} starting and ending at 0.2 V vs. MMSE. Afterwards, a defined stability protocol was performed. Therefore, the solution was replaced by a 2 M H_2SO_4 solution that was continuously purged with O_2. To investigate the influence of vanadium ions on the ORR activity and stability of the catalysts, different measurements were performed each with and without vanadium ions in the solution. A heavy vanadium contamination of the solution was simulated by adding 0.1 M $VOSO_4$. In the stability protocol, the working electrode was cycled 100 times between different potentials simulating alternating operation modes of the battery. After the stability protocol, the solution was replaced with N_2 purged 2 M H_2SO_4 again for the characteriza-

tion measurements. To remove the V-containing solution from the electrodes, they were immersed in another 2 M H_2SO_4 solution before. Fig. 3.13 illustrates the measurement procedure described.

Characterization		Stability Protocol		Characterization
2 M H_2SO_4		2 M H_2SO_4 (+ 0.1 M $VOSO_4$)		2 M H_2SO_4
-0.65 ... 1.0 V vs. MMSE		various potential regimes		-0.65 ... 1.0 V vs. MMSE
N_2 purged		100 cycles, O_2 purged		N_2 purged
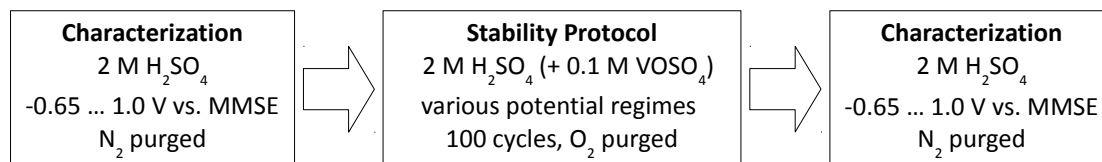
Figure 3.13: *Scheme of the measurement procedure.*

3.5.4 Stability Studies on Ir decorated Pt Nanorods

The comparing measurements on Pt nanorods, Ir decorated Pt (Ir@Pt) nanorods, and Ir nanodots consisted of an activation protocol followed by an OER-ORR stability protocol simulating multiple changes between charge and discharge mode of the VARFB. Since it is known, that cycling between ORR and OER potentials is very degrading for Pt nanoparticles [8], an OER stability protocol was also performed simulating multiple changes between charge mode and stop of the VARFB:

- Activation protocol (six low potential characterization cycles, six wide potential characterization cycles, six low potential characterization cycles)

- OER-ORR stability protocol (2,400 OER-ORR degradation cycles in groups of 50 to 200 cycles, interrupted by two wide potential characterization cycles and six low potential characterization cycles, respectively)

- Or: OER stability protocol (2,400 OER degradation cycles in groups of 50 to 200 cycles, interrupted by two wide potential characterization cycles and six low potential characterization cycles, respectively)

The measurement procedure is illustrated in Fig. 3.14. The potential regimes and scan rates are shown in Tab. 2. The potential maximum of the degradation cycles was chosen not too high, to avoid the formation of bubbles. For the stability analysis always the last OER and ORR characterization cycles were used.
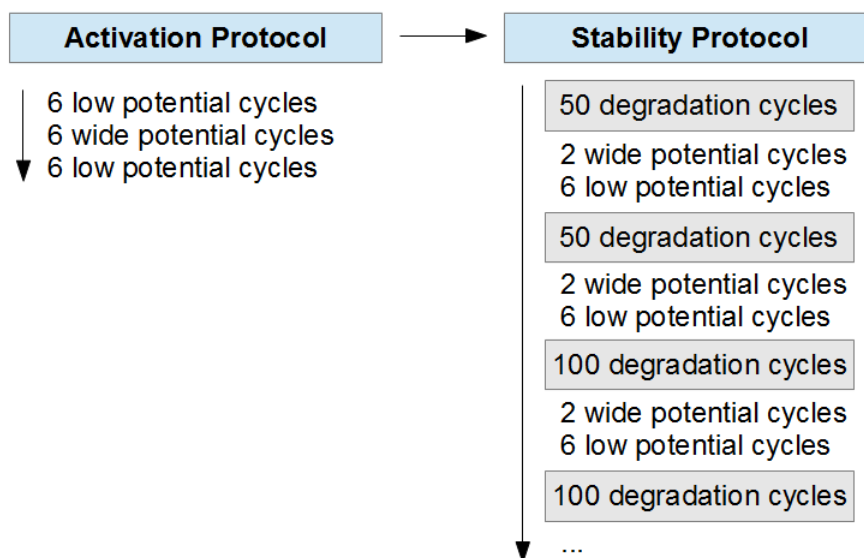
Figure 3.14: *Scheme of the measurement procedure.*

Type of CV	Potential regime / V vs. MMSE	Initial and final potential / V vs. MMSE	Scan rate / mV/s
Low potential characterization	-0.65 ... 0.2	0.1	100
Wide potential characterization	-0.65 ... 0.95	0.1	100
OER degradation	0.35 ... 0.85	0.4	500
OER-ORR degradation	-0.2 ... 0.85	0.1	500

Table 2: *Potential regimes and scan rates of the CVs used in the stability protocol.*

3.5.5 Stability Studies on Ir decorated RuO$_2$ Nanoparticles

For the studies on Ir nanopdots, RuO$_2$ nanoparticles and the Ir decorated RuO$_2$ the measurement comprised an activation protocol followed by an OER stability protocol that simulates multiple changes between charge mode and stop of the VARFB:

- Activation protocol (six low potential characterization cycles, six wide potential characterization cycles)

- OER stability protocol (2,000 OER degradation cycles in groups of 50 to 200 cycles interrupted by two wide potential characterization cycles, respectively)

The measurement procedure is illustrated in Fig. 3.15. Tab. 2 lists the potential regimes and scan rates used. The potential maximum of the degradation cycles was

chosen not too high, to avoid the formation of bubbles. For the stability analysis always the last OER characterization cycle was used.
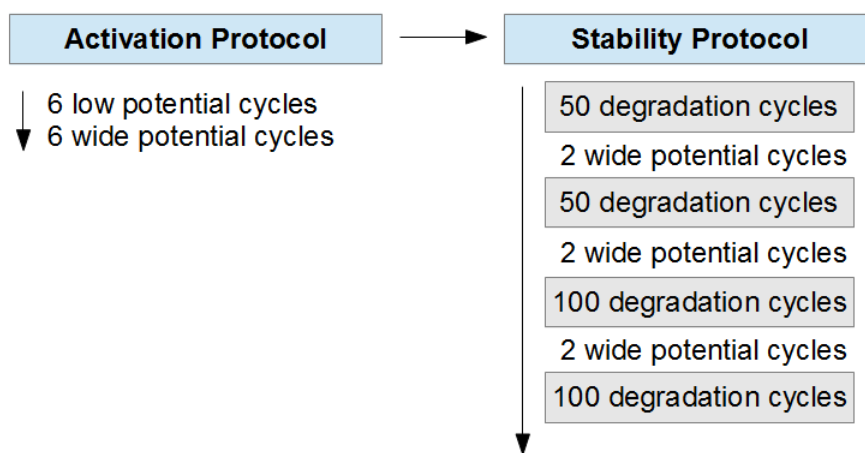
Figure 3.15: *Scheme of the measurement procedure.*

3.6 Electrochemical Quartz Crystal Microbalance (EQCM)

The electrochemical quartz crystal microbalance (EQCM) is a method, that allows to detect in situ mass changes of the working electrode during electrochemical experiments [94, 96, 97]. Thereby, it reveals, complementary to the current, further information about electrode processes. In chapter 4, the EQCM was used in order to investigate, whether a Vanadium contamination of the electrolyte leads to deposits on a bulk Pt electrode or whether it influences the Pt surface reactions in any other way. The aim of this section is to introduce this method and to present the experimental setup as well as the design of the measurements.

The EQCM is based on the piezo-electric effect: when a force acts on a quartz crystal leading to a deformation of it, electric dipole moments between the charges in the crystal are changed leading to a potential difference across the crystal. Vice versa, a potential applied to the crystal results in a deformation of it. Using alternating voltages the crystal vibrates with the frequency of the applied voltage. Usually, the EQCM is operated at the crystal's resonance frequency. The latter depends on the dimensions and material specific properties of the crystal, normally the shear modulus and the density (or in other words, the crystal's mass). If the load of the crystal is changed, the resonance frequency changes correspondingly.

In practice, the EQCM crystal is coated with two electrodes, mostly made of Au (gold) or Pt. Between these electrodes the alternating voltage is applied with the crystal's resonance frequency leading to a shear oscillation. Moreover, one electrode faces the electrolyte and acts as working electrode (Fig. 3.16).
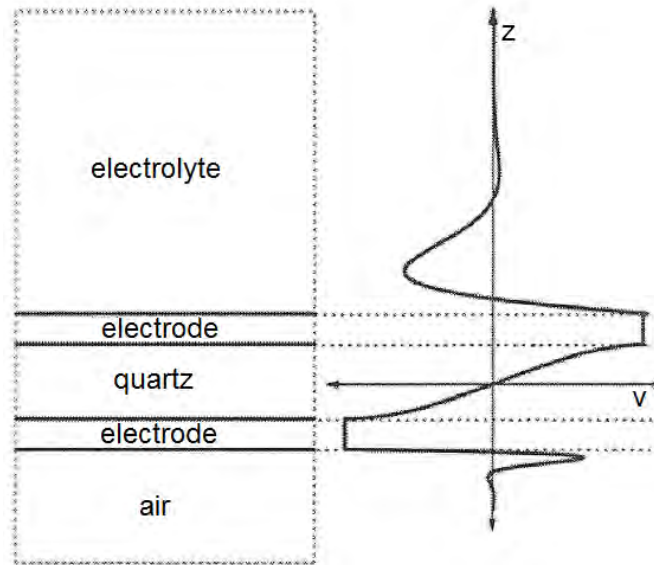
Figure 3.16: *Scheme of the media coupled to the oscillation (left) and the tangential velocity v of the layers as function of the position perpendicular to the crystal's center z (right). The image is adapted from [96].*

If, for example, metal is deposited from an electrolyte containing metal ions, the crystal's mass rises leading to a decrease of its resonance frequency (Fig. 3.17). By detecting the latter, one can, thus, conclude to mass (or more generally load) changes.

The relation between frequency changes Δf and mass changes Δm is described by the Sauerbrey equation [98]:

$$\Delta f = -c_m \Delta m \tag{3.20}$$

c_m is a characteristic constant defined by the resonance frequency f_0, the shear modulus of quartz μ_q and its density ρ_q:

$$c_f = \frac{2 f_0^2}{\sqrt{\mu_q \rho_q}} \tag{3.21}$$

The resonance frequency is usually in a range of 5 to 10 MHz. With μ_q=2.947·10^{11} g cm^{-1} s^{-2} and ρ_q=2.648 g cm^{-3} and f_0=6 MHz c_m=8.13·10^7 Hz g^{-1} cm^2. Consequently, an added mass of 12.3 ng cm^{-2} results in a frequency decrease of 1 Hz, that is under common conditions above the detection limit. The deposition of a monolayer of silver would lead to a frequency decrease of 18 Hz [96].
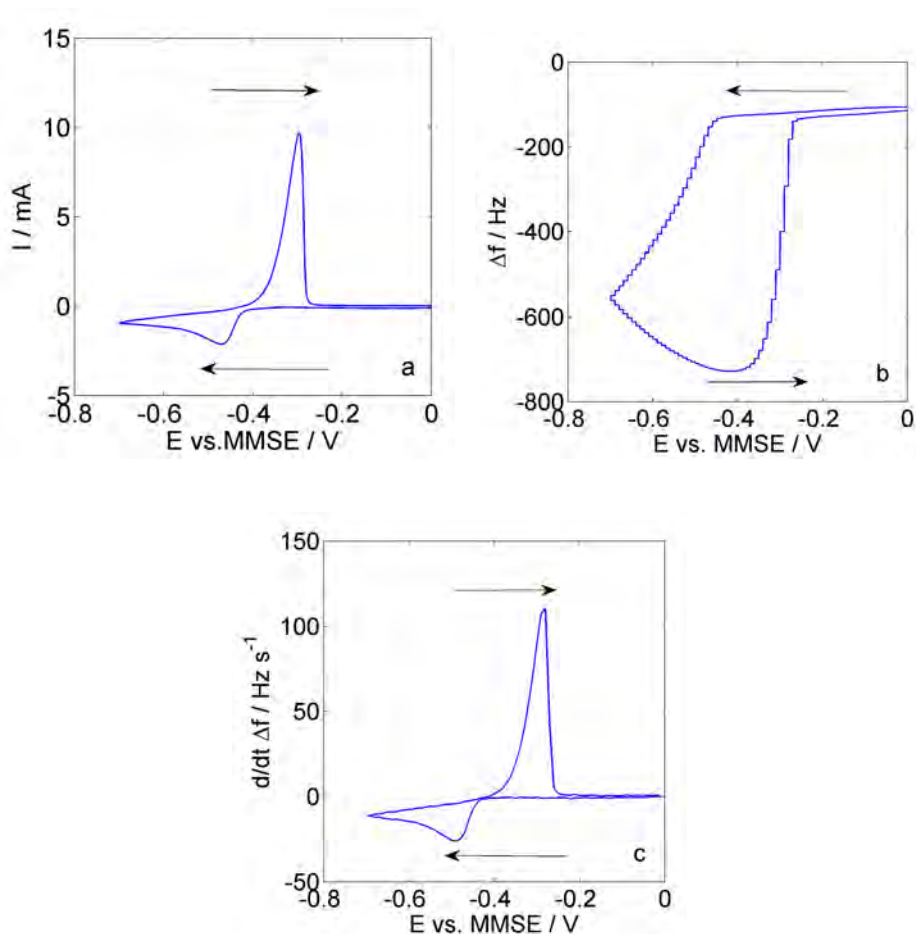
Figure 3.17: *a: CV of Cu deposition and dissolution from a 0.2 M K_2SO_4 electrolyte with 10 mM $CuSO_4$ performed with 10 mV s^{-1}. b: frequency changes as function of the applied potential. The deposition of Cu during the anodic scan leads to a mass increase of the crystal, meaning a frequency decrease. c: frequency change deviated by time. Since it is correlated with the mass flux, that equals the detected current, one yields a signal shape similar to the CV.*

One has to keep in mind, that this equation is only true, when some assumptions are fulfilled: The surface has to be smooth, additional mass has to be evenly distributed and not too much mass should be added. Since the crystal's resonance frequency changes slightly with temperature, the latter shall be constant. Moreover, no other changing loads shall act on the crystal. Additional loads originate from coupling of the shear wave in the air below the crystal and in the electrolyte. The propagation depth of the shear wave into the electrolyte is defined by the electrolyte's viscosity and density and the resonance frequency and is for a dilute aqueous solution at room temperature around 0.23 μm. The load on the electrolyte side depends mainly on the electrode's surface roughness as well as the liquid's viscosity and density, that depend both on the temperature. The shear modulus of the electrode and a

thin deposited mass layer is assumed to have no noteworthy influence, since the displacement of these layers is assumed to be constant in z-direction. Strain in the crystal resulting from the hydrostatic pressure of the electrolyte influences the resonance frequency. Interfacial slippage, meaning that the electrolyte's tangential velocity does not equal the electrode's velocity at the electrode-electrolyte boundaray might also influence the resonance frequency. Further information on the EQCM can be found in [94, 96, 97].

Electrochemical quartz crystal microbalance (EQCM) measurements were performed in a 2 M H_2SO_4 solution with and without 0.1 M $VOSO_4$ purged with O_2 at room temperature. An Inficon Research Quartz Crystal Microbalance system was used with commercially available AT-cut 5 MHz one inch diameter quartz crystals coated with a bulk platinum electrode from the company Inficon. A Pt coil served as counter electrode, and a MMSE was used as reference electrode (Fig. 3.18). An electronic iR drop compensation described in [95] was applied. Before the measurements, the working electrode was electrochemically cleaned as described before. Afterwards, eleven cycles between -0.2 and 1.1 V vs. MMSE were performed with 10 mV s^{-1} in oxygen purged 2 M H_2SO_4 electrolyte without and with 0.1 M $VOSO_4$. The ten cycles after the initial one were averaged for further analysis.
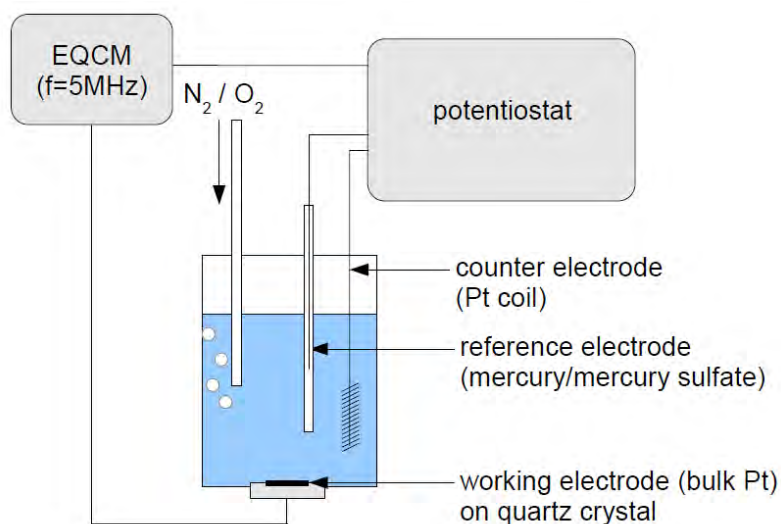
Figure 3.18: *Scheme of the electrochemical quartz crystal microbalance (EQCM) setup.*

4 Influence of V Ions on the Degradation of Pt catalysts

In VARFBs, as in other Redox Flow Battery systems, an undesired crossover of ions through the proton exchange membrane from one electrolyte to the other was reported to occur [6, 7, 16]. That lowers the battery's efficiency [6, 7, 16]. Moreover, there is the question, whether there is an influence of a Vanadium contamination on the stability of a Pt catalyst simulating VARFB conditions and more specifically, if V compounds deposit on the catalyst's surface. In this section, this question is investigated. More information on the background of ths study can be found in chapter 2.3.

Cyclic voltammetry in a three-electrode setup was used to simulate the operation conditions in a bifunctional oxygen electrode of a VARFB. A heavy Vanadium contamination was simulated by adding 0.1M $VOSO_4$. In a first step a bulk Pt electrode was used as working electrode as relatively simple model system. EQCM measurements were performed at bulk platinum, in order to investigate possible deposition of vanadium compounds and gain further insight into the processes occurring at the electrode surface. Closer to a real battery, the stability of Pt nanoparticles supported on carbon (Pt/C) and the influence of V ions on their stability was investigated in a second step. The experimental methods are described more detailled in chapter 3. These results were already published in [8].

4.1 Electrochemical Characterization of Bulk Pt

In a first step, we investigated the influence of vanadium contaminations on a bulk Pt electrode as structurally simple model system. Fig. 4.1 shows a typical CV of bulk platinum in sulphuric acid (black) with the oxygen reduction peak at 0 V vs. MMSE and the oxygen evolution reaction at potentials above 1 V vs. MMSE. Furthermore, the hydrogen underpotential deposition (HUPD) features can be observed around -0.5 V vs. MMSE followed by the hydrogen evolution below -0.7 V vs. MMSE. The blue dashed curve shows the CV in a solution with the same H_2SO_4 concentration and 0.1 M $VOSO_4$. Here, one can see the redox peaks of the transitions between V^{II}, V^{III}, V^{IV} and V^V species. The assignment of all mentioned peaks is in agreement with available reference data [21, 99, 100]. The relatively low intensity of the oxidation peak of V^{2+} (labeled O2 in Fig. 4.1) can be explained by oxidation of V^{2+} due to reduction of protons to H_2 [6].
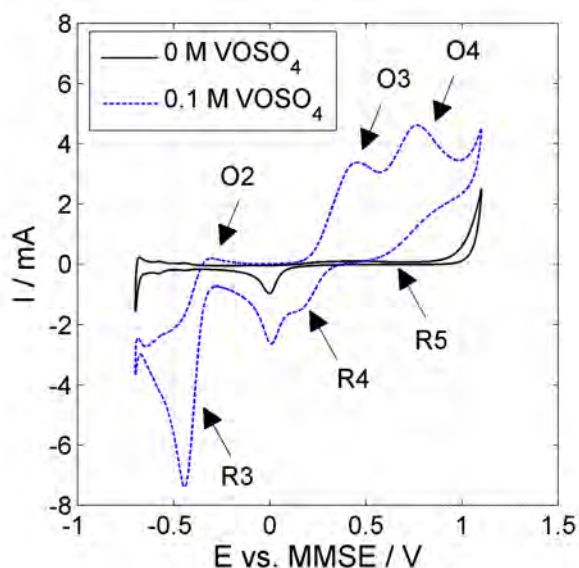
Figure 4.1: *CV of an EQCM bulk Pt electrode in 2 M H_2SO_4 with (blue dashed) and without (black) V contamination. Scan speed: 20 mV s^{-1}. The oxidation of V^{2+}, V^{3+} and VO^{2+} is marked with O2, O3, and O4, respectively, the reduction of VO_2^+, VO^{2+}, and V^{3+} with R5, R4, and R3, respectively.*

To simulate the battery system -0.2, 0.2 and 1.1 V vs. MMSE were defined as discharge, open circuit and charge potential at this electrode, respectively. The charge potential was chosen to maximize the current without getting interferences with gas bubbles due to too much oxygen evolution. In the case of discharge, the potential of -0.2 V was chosen to achieve a sufficiently high oxygen reduction current, but to avoid reduction of V^{3+}.

4.2 Electrochemical Quartz Crystal Microbalance Investigations

EQCM measurements were performed at bulk platinum to investigate a possible V deposition and, more generally, to gain an insight into the processes occurring at the electrode surface during the treatment. Fig. 4.2 shows the CVs recorded with the EQCM Pt electrodes between the previously defined charge and discharge potentials (top) and the average potential-frequency curves (bottom) in V-free and V-containing 2 M H_2SO_4 electrolyte. In both cases, an increase of the frequency of around 2 Hz per cycle was observed during the measurement. As a possible reason, we assume a slow platinum dissolution to occur under these harsh conditions (high potentials, strong acidic solution), in accordance with other reports [101]. The frequency step at the lower potential limit is due to the fact, that the averaging of

the potential-frequency curves was performed for cycles starting and ending at the lower potential limit. Nevertheless, this drift does not significantly affect the results.
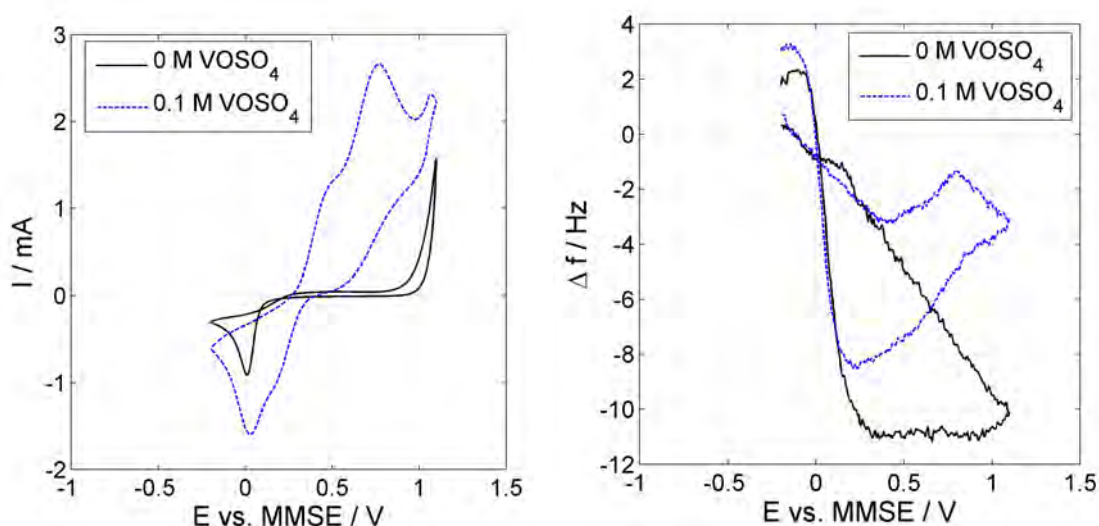
Figure 4.2: *Left: CV at an EQCM bulk Pt electrode in V free (black) and V containing (blue dashed) solution. Right: Average of 10 potential-frequency curves. The data indicates a lower (hydr)oxide occupancy at the platinum surface in the presence of V ions. All measurements were performed with a potential sweep speed of 10 mV s^{-1}.*

The measurement in V-free solution shows the typical potential-frequency curve characteristics known from the literature [102–107]. Starting to explain the curve at -0.2 V vs. MMSE, the frequency continuously decreases with rising potential (meaning an increase in electrode mass) due to the build-up of an (hydr)oxide layer at the platinum surface. During the backward scan, the frequency stays constant until about 0.3 V. This means a constant (hydr)oxide occupancy until the ORR potential is reached. At this potential, the surface (hydr)oxide is rapidly detached. Finally, the starting frequency is reached again, except for the small general drift mentioned above. The measurement in V-containing solution shows no strong additional frequency decrease. In fact, the frequency decrease is even less pronounced than in the V-free case. This means that no deposition of vanadium compounds takes place. This is evidenced by further measurements that show no significant changes of CVs performed before and after a treatment in V-containing solution. Starting to interpret the EQCM-measurements in V-containing solution at -0.2 V vs. MMSE, one can first see the same frequency decrease as described in the V-free system due to the build-up of the (hydr)oxide layer at the Pt electrode. However, at 0.4 V vs. MMSE the frequency starts to rise. This occurs simultaneously with

the oxidation of V^{3+} via the reaction [108]

$$V^{3+} + H_2O \rightleftarrows VO^{2+} + 2H^+ + e^- \tag{4.1}$$
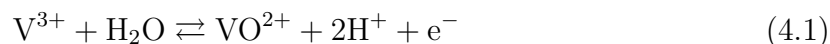
and the oxidation of VO^{2+} via the reaction [108]

$$VO^{2+} + H_2O \rightleftarrows VO_2^+ + 2H^+ + e^- \tag{4.2}$$
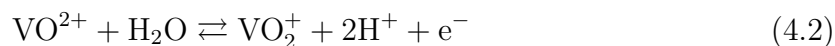
The frequency maximum around 0.8 V vs. MMSE occurs simultaneously with the current peak attributed to the vanadium oxidation. The authors suggest a reaction of V^{3+} and VO^{2+} with the surface (hydr)oxide leading to a decreasing surface (hydr)oxide occupancy. One possible explanation is that the (hydr)oxide layer acts as oxygen source during the oxidation of V^{3+} and VO^{2+}. Hence, two competing processes can be assumed at the surface: the water oxidation leading to the build-up of the surface (hydr)oxide layer and the vanadium oxidation leading to the consumption of oxide. With the given parameters, the vanadium oxidation dominates the water oxidation between 0.4 and 0.8 V vs. MMSE, resulting in an electrode mass decrease. At potentials above 0.8 V vs. MMSE, the electrode mass starts to increase again which might be explained by a higher water oxidation rate and, thus, a faster surface (hydr)oxide layer build-up. Furthermore, the V oxidation currents decrease at potentials above 0.8 V vs. MMSE and during the backward scan, meaning a lower (hydr)oxide consumption and, consequently, an increase in electrode mass. The backward scan shows with decreasing potential a rising electrode mass up to the ORR potential. In this range, the electrode mass is lower than that in the V-free case. Thus, it is suggested that the (hydr)oxide occupancy is lower than in the V-free case because of the competing V oxidation that counteracted the surface layer build-up before. At potentials below around 0.3 V vs. MMSE, the ORR takes place similarly to the V-free system.

4.3 Degradation Behavior of bulk Pt and Influence of V Ions

Following the procedure described in section 3.5.3, stability protocols consisting of 100 cycles between -0.2 and 1.1 V vs. MMSE were performed in 2 M H_2SO_4 solution, containing either no V ions or 0.1 M $VOSO_4$ to simulate a heavy V contamination. Fig. 4.3 shows the characterization CVs before and after the treatment (a,b) as well as selected cycles during the treatment (c, d).
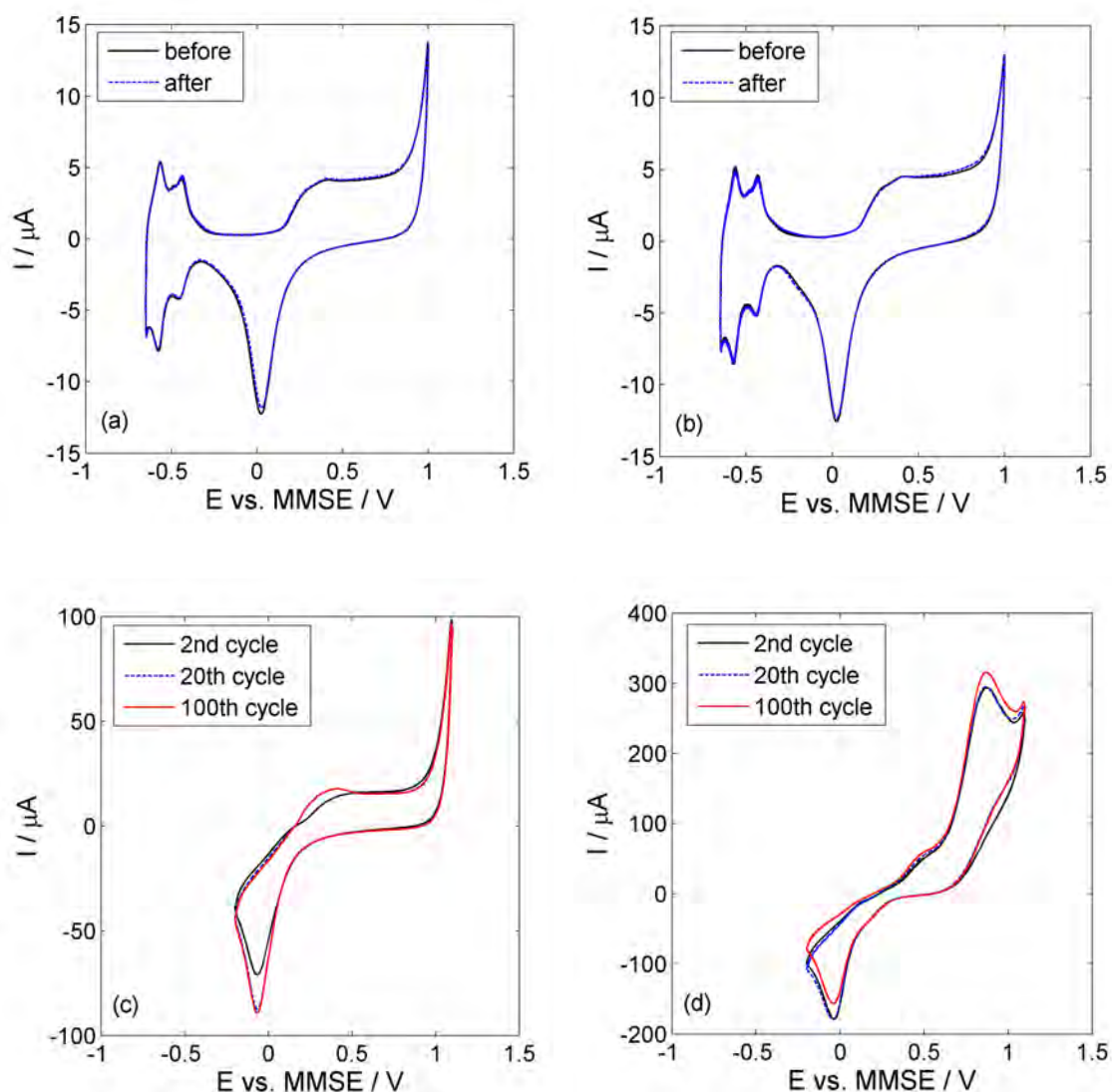
Figure 4.3: *Top: CVs of bulk Pt performed in N_2-purged solution with 100 mV s^{-1} scan speed before (black) and after (blue dashed) the degradation treatment in a V-free 2 M H_2SO_4 solution (a) and 2 M H_2SO_4 solution with 0.1 M $VOSO_4$ (b). Neither a significant degradation nor a significant difference between both samples can be observed. Bottom: Selected cycles of the degradation treatment (100 cycles between -0.2 and 1.1 V vs. MMSE, scan speed: 500 mV s^{-1}) in V-free (c) and V-containing (d) solution purged with O_2 show no significant degradation.*

100 cycles did neither lead to a significant degradation, nor can any significant influence of V ions be observed. Reier et al. [54] performed an OER stability protocol on a bulk Pt rotating disc electrode in 0.1 M $HClO_4$ leading to an OER activity reduction. The protocol consisted of 51 cycles with 200 mV s^{-1} between around 0.3 and 1.2 V vs. MMSE, thus, in a range above the ORR potential and to more than 100 mV higher potentials than in this study. The OER activity loss to less than

the half was explained by the build-up of a poorly conducting Pt oxide layer [54]. The reason for the difference between the OER stability of the bulk Pt in this study and the degradation of the OER currents observed by Reier et al. [54] may be the higher upper potential limit in the latter case, leading to a thicker insulating oxide layer. To describe the observations on a statistical basis, the stability protocol was performed five times for the solutions with and without V contamination, and the ORR peak currents before and after the protocol were taken for further analysis. To compare the degradation of the ORR activity after the protocols, we calculated the ratio of the ORR peak current after the treatment and the ORR peak current before. The average and standard deviation of this ratio is (1.01 ± 0.03) for the treatment in V-free solution and (1.03 ± 0.04) for the treatment in V-containing solution, respectively. The analysis of variances shows no significant degradation effect nor a significant influence of the V contamination.

4.4 Structural Characterization of Pt Nanoparticles

XRD and TEM measurements were performed to gain the mean and the standard deviation of the diameter of the Pt nanoparticles (Fig. 4.4).
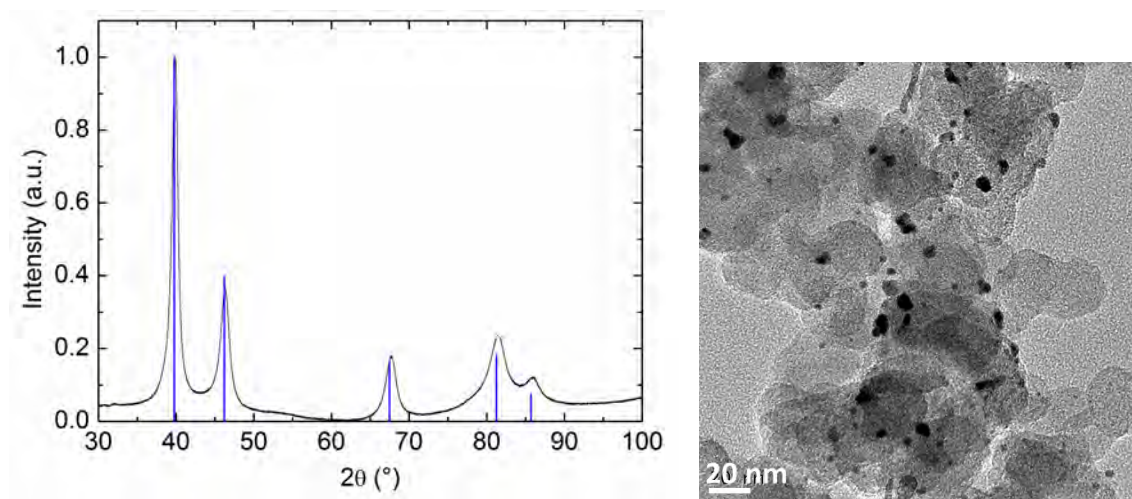
Figure 4.4: *Left: XRD pattern of the Pt/C powder. The stick pattern is the ICDD reference pattern for platinum number 03-065-2868. The volume mean crystallite size estimated by the Scherrer equation and averaged over the peaks is (7 ± 2) nm. Right: HR-TEM image of the Pt/C sample. The volume-weighted mean particle diameter determined by statistical image analysis is (6 ± 2) nm.*

The volume-weighted mean crystallite diameter estimated from the XRD pattern by the Scherrer equation [89] (assuming the Scherrer constant $k=0.9$) and averaged

over the three peaks between 35° and 75° is (7 ± 2) nm (Fig. 4.4). The HR-TEM images (Fig. 4.4) show that the Pt nanoparticles are well dispersed on the carbon support and seem to have a relatively broad size distribution. The volume-weighted mean crystallite diameter [109] estimated from HR-TEM images over 214 particles is (6 ± 2) nm.

4.5 Electrochemical Characterization of Pt Nanoparticles

To study the stability of the ORR activity of the Pt/C electrode under simulated operation conditions in a VARFB, different changes of the operation modes were simulated by CVs in different potential regimes. The influence of a V contamination was studied by comparing measurements without V ions in the H_2SO_4 electrolyte with measurements with 0.1 M $VOSO_4$. To get an overview, CVs over the whole potential range are shown in Fig. 4.5 in N_2 purged solutions with and without V contamination.
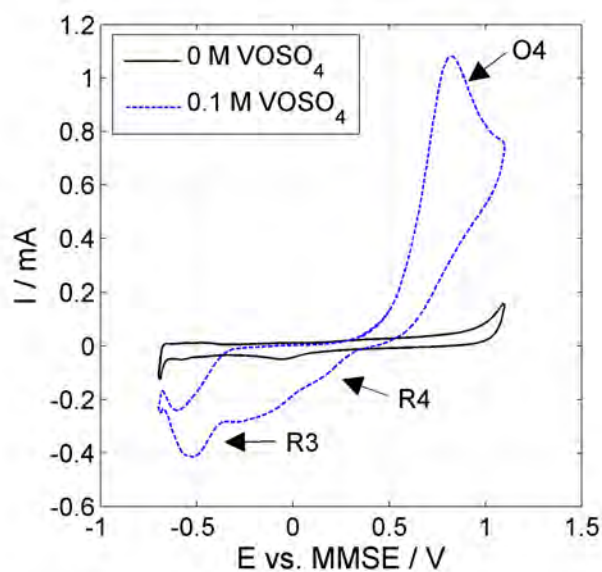
Figure 4.5: *CVs of the Pt/C electrode in a 2 M H2SO4 solution purged with N_2 with (blue dashed) and without (black) a 0.1 M $VOSO_4$ contamination. Scan speed: 100 mV s^{-1}. In the V-containing solution the oxidation of VO^{2+} (O4) and the reduction of VO^{2+} (R4) and V^{3+} (R3) can be observed.*

Basically, the data obtained is similar to the results for bulk Pt, but the signals are less pronounced, and some of the peaks discussed before are strongly broadened and hardly visible. In detail, the CV in V-free solution shows the typical OER, ORR, HUPD, and hydrogen evolution features. The ORR peak potential of the

Pt/C electrode is a little bit cathodically shifted compared to the bulk Pt. This is commonly attributed to particle size effects: smaller particles have a higher fraction of corner and edge atoms that bind oxygen stronger than terrace atoms [31, 54, 110, 111]. The CV of the Pt/C in V-containing solution is dominated by the oxidation of VO^{2+} (O4) and the reduction of VO^{2+} (R4) and V^{3+} (R3). The oxidation of V^{2+} cannot be identified here because of the oxidation of V^{2+} via proton reduction on Pt as described before. The oxidation of V^{3+} and the reduction of VO_2^+ cannot be discovered, either. The hydrogen evolution feature can be observed, but the HUPD and OER currents are masked by the V redox currents. The ORR currents lead to a shoulder between the signals of the reduction of VO^{2+} and V^{3+}.

4.6 Degradation Behavior of Pt Nanoparticles

Next, stability protocols were conducted with and without a vanadium contamination (Tab. 3). 100 cycles between charge and discharge potentials (-0.2 ... 1.1 V vs. MMSE) were performed (stability protocol A). Furthermore, the degradation was studied when cycling only between the potential defined as open circuit potential and charge potential (0.2 ... 1.1 V vs. MMSE, stability protocol B) or discharge potential (-0.2 ... 0.2 V vs. MMSE, stability protocol C). Since the high potentials are known to be harsh conditions, cycles were also performed between discharge or open circuit potential and 0.8 V (stability protocol D and E). At this potential, the currents related to water oxidation are much lower than at 1.1 V vs. MMSE, but oxidation to VO_2^+ does still take place. Therefore, a possible influence of the redox reactions with V may be easier to discover after these relatively mild treatments. Fig. 4.6 exemplarily shows characterization CVs (a, b) as well as selected cycles (c, d) from charge-discharge treatment (A) in the presence and absence of vanadium.

The characterization CVs show a decrease of the HUPD features and, thus, the electrochemically active surface area. They also show a decrease of the Pt (hydr)oxide build-up feature above 0.3 V vs. MMSE, the OER feature and of the ORR peak. A strong degradation of the OER currents of the Pt/C can be observed during this treatment that has an upper potential limit of 1.1 V vs. MMSE, but a much smaller decrease in the characterization CVs running up to 1.0 V vs. MMSE. This shows the strong potential dependence of the deactivation behavior and its partial reversibility reported in the literature [112].
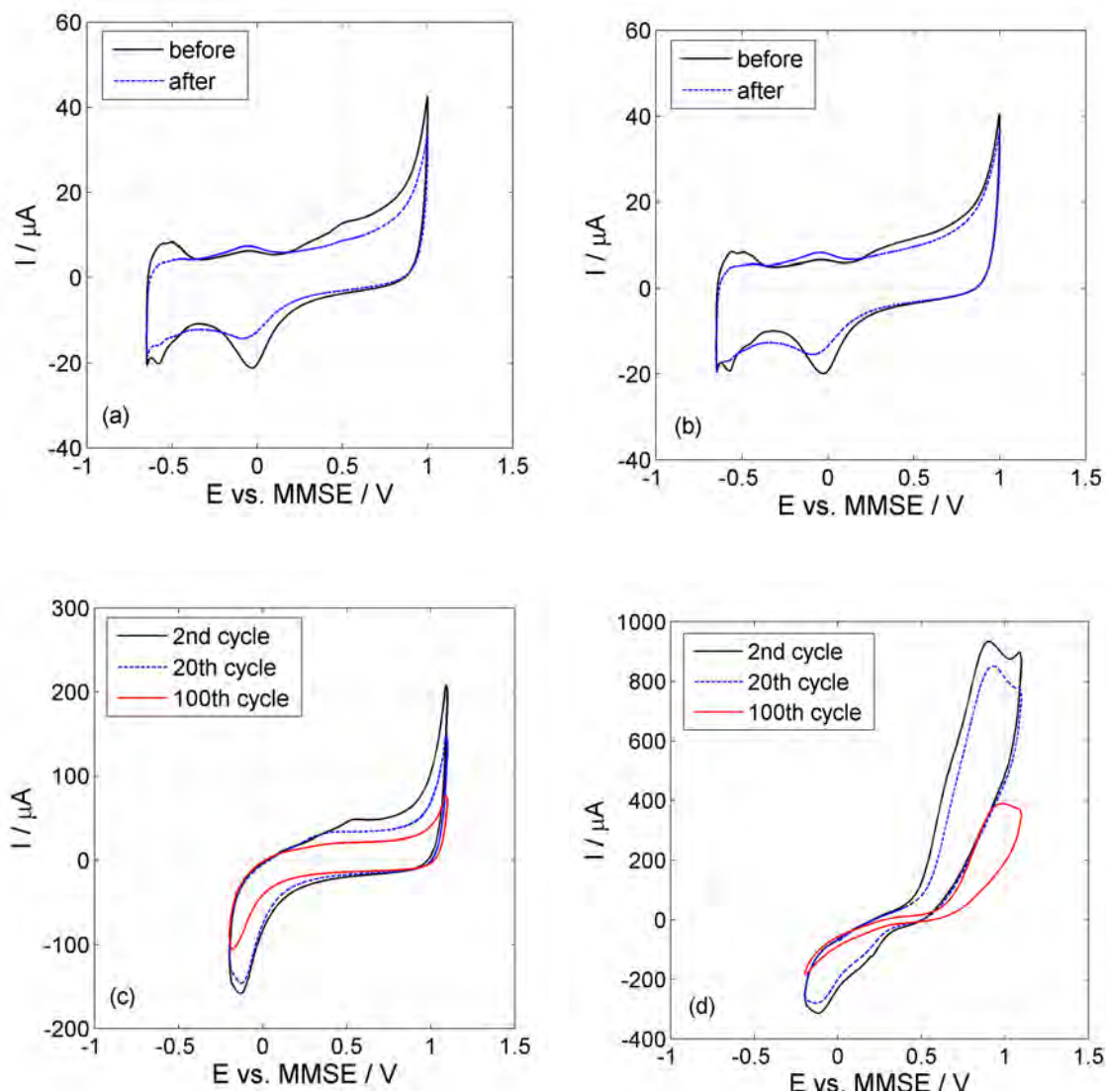
Figure 4.6: *Top: Characterization measurements of Pt/C before and after the charge-discharge treatment (A) (100 cycles between -0.2 and 1.1 V vs. MMSE) in 2 M H_2SO_4 solution without vanadium contamination (a) and with 0.1 M $VOSO_4$ (b). Scan speed: 100 mV s^{-1}. A decrease of the platinum related features and an increase of the currents in the double layer region related to carbon corrosion can be observed. Bottom: Selected cycles of the treatment without (c) and with (d) V contamination showing a strong decrease in ORR and OER currents and in the case of V contamination also a decrease in the V oxidation and reduction currents.*

Reier et al. [54] performed a stability protocol at Pt/C leading to a complete deactivation. The stability protocol was performed with a rotating disk electrode (RDE) setup in 0.1 M $HClO_4$ and consisted of 51 scans with 200 mV s^{-1} between around 0.3 and 1.2 V vs. MMSE. After that protocol, no dissolved Pt could be found in the

solution. Furthermore, HUPD features decreased, but did not totally vanish [54]. The OER deactivation of the Pt nanoparticles during the stability protocol was explained by the build-up of a poorly conductive Pt oxide at high potentials. A thicker oxide layer leads to a lower electronic conductivity resulting in a decrease of oxygen evolution rate. Because of the higher oxophilicity of the Pt nanoparticles compared to the bulk Pt, the oxide layer was assumed to be thicker, leading to a strong decrease of the OER activity of Pt nanoparticles [54]. The still observable HUPD features after the treatment can be explained by the partial reversibility of the Pt oxidation [112]. Moreover, Reier's protocol is performed above ORR potentials leading to less irreversible platinum degradation than in our stability protocol A. We suggest that in our stability protocol no total OER deactivation is observed mainly because of the upper potential limit being lower and thus, leading to a thinner oxide layer compared to Reier's work. Possibly, the smaller size of Reier's nanoparticles compared to our ones led also to a stronger deactivation. In accordance with other literature [31,32,54], an increase of the currents in the double layer region can be observed after the charge-discharge treatment that can be assigned to carbon substrate degradation (Fig. 8a, b).

To describe our observations on the degradation of the ORR currents on a statistical basis, the ORR peak current after the stability protocol was divided by the current before. To estimate a possible influence of the vanadium contamination on the degradation behavior, the mean value and standard deviation of the current ratios were calculated in all cases. The results are shown in Tab. 3.

name of protocol	potential vs. MMSE / V	i_{ORR}(after) / i_{ORR}(initial) without V ions	i_{ORR}(after) / i_{ORR}(initial) with V ions
A	-0.2 ... 1.1	0.68 ± 0.04	0.74 ± 0.04
B	0.2 ... 1.1	0.94 ± 0.04	0.91 ± 0.06
C	-0.2 ... 0.2	0.90 ± 0.04	0.92 ± 0.02
D	-0.2 ... 0.8	0.72 ± 0.05	0.71 ± 0.05
E	0.2 ... 0.8	0.95 ± 0.04	0.94 ± 0.03

Table 3: *Mean value and standard deviation of the ratio of the ORR peak current i_{ORR} after the stability protocol and i_{ORR} before it for protocols with different potential ranges and solutions with or without vanadium contamination.*

In contrast to the former experiments with the Pt bulk electrode, the charge discharge treatment (A) leads to a severe degradation of the catalyst, as evidenced by the decrease of the considered current ratio to around 70 percent (see Tab. 1). The degradation of the ORR current is similar after performing stability protocol D, that employs 0.8 V vs. MMSE as upper potential limit. The protocols that do not include ORR potentials (B and E) or no high potentials (C) show a much smaller

degradation of the ORR peak.

This can be explained by the repeated build-up and detachment of the (hydr)oxide layer on the platinum under these conditions and is in agreement with observations made in other studies [31] on Pt nanoparticles as oxygen catalysts. They show that the most degrading treatment is the detachment of the previously built (hydr)oxide layer. The higher the upper potential limit is, the more (hydr)oxide is built that can be detached in the ORR potential range degrading the catalyst. In the discharge open circuit treatment (C), the surface (hydr)oxide layer is only built up to a small degree at the upper potential limit, leading to a lower ORR current and, therefore, a smaller degradation. There is no significant difference between the degradation behavior of the ORR current after the mild treatments B, C and E.

4.7 Influence of V Ions on the Degradation Behavior of Pt Nanoparticles

Turning now to the influence of vanadium ions, a significant influence (according to analysis of variances with a significance level of 5 percent) can be observed in the case of stability protocol A, but not in the other treatments. The presence of V ions counteracts the ORR decrease in treatment A. We suggest the following explanation: this treatment is very aggressive due to the high degree of (hydr)oxide occupancy that is achieved by the high upper potential limit [106] and the following high ORR current, meaning a high amount of surface (hydr)oxide being reduced to water and detached. The EQCM measurements on bulk Pt indicate that V oxidation leads to a decrease of surface (hydr)oxide occupancy. Consequently, less (hydr)oxide can be reduced to water and detach at the ORR potential, meaning a lower degradation. The whole interaction with the V ions is assumed not to be aggressive enough to compensate the stability gain by the decreased ORR detachment. In the other stability protocols, no influence can be observed, because in case B and E no ORR takes place, and in case C and D, the upper potential limit is lower, meaning a lower degree of (hydr)oxide occupancy in the V-free case and, thus, a smaller difference in (hydr)oxide occupancy when V ions are present. The smaller this difference is, the smaller is the difference in the degradation behavior.

4.8 Conclusion

In this chapter, the stability of bulk Pt and carbon supported Pt nanoparticles (Pt/C) was examined under conditions relevant to their use in the positive half-cell

of a vanadium air redox flow battery. Special attention was paid to the investigation of possible influences of vanadium ions in the solution on the stability of the Pt catalysts with respect to the oxygen reduction reaction.

Analysis of different stability protocols showed neither a decrease of bulk Pt surface nor any influence of V ions on it. In the case of Pt/C, protocols including ORR potentials and high potentials led to a severe decline of the ORR currents. In the case of cycling between ORR and OER potentials, the presence of V ions led to a lower degradation of the Pt/C.

EQCM measurements performed in the case of bulk Pt in V-containing solution showed no deposition of V compounds, but a decrease of the electrode mass in the range of V^{3+} and VO^{2+} oxidation potential compared to measurements in V-free electrolyte. We suggest, that these oxidations reduce the surface (hydr)oxide occupancy at the Pt electrode, so that the degrading ORR currents are lower, and finally less degradation is observed.

Concerning the use in a bifunctional reaction unit of a vanadium air redox flow battery, the highest stability of Pt/C should be achieved avoiding high potentials that are needed for the OER during discharge, for example by the use of a positive half-cell consisting of two electrically separated electrodes for charge and discharge. Another perspective is the stability improvement of the Pt nanoparticles and the substrate by future research in material science.

5 Stability of Pt Nanorods decorated with Ir Nanodots

One possibility to design the bifunctional oxygen electrode of a VARFB or a PEM URFC (proton exchange membrane unitized regenerative fuel cell) is using bifunctional OER-ORR catalysts (see chapter 2.4). Literature shows, that colloidchemical preparation leads to a better dispersion of the particles compared to physical mixing [59]. Because of insufficient stability of RuO_2, bifunctional OER-ORR catalysts in acidic systems are usually based on Pt and Ir. The stepwise synthesis allows a higher control of the composite nanoparticles' morphology and, thus, their activity and stability. As described in chapter 2.4, stability studies are rare. And more seldom is a deeper investigation of the degradation mechanisms of bifunctional catalysts and possible approaches to increase the stability. The interaction between the Ir-based OER catalyst and the Pt ORR catalyst in a bifunctional Ir@Pt catalyst towards the electrochemical stability is investigated in this chapter. The structural properties of Ir nanodots, Pt nanorods and Ir decorated Pt nanorods (Ir@Pt) are studied with XRD and TEM. Pt nanorods served as support, since an excellent stability is reported compared to Pt/C at least for simulated fuel cell operation [37–39]. The stability towards an OER stability protocol (simulating repeated change of the operation mode between charging mode and stop of the VARFB) and towards an OER-ORR stability protocol (simulating repeated change between charge and discharge mode of an VARFB) is studied in a three electrode cyclic voltammetry setup. The OER stability of Ir@Pt is compared to the OER stability of pure Ir nanodots, and the ORR stability of Ir@Pt is compared to pure Pt nanorods, respectively. The influence of annealing on the structure and electrochemical stability is also investigated. Detailed information about the experimental methods can be found in chapter 3. Parts of the content are currently submitted to the Journal of Physical Chemistry C and under review.

5.1 Structural Characterization

Unsupported Ir nanodots were synthesized with varying Ir salt concentrations (20, 40, 60 and 80 mg $IrCl_3$·n H_2O were added). As expected, the XRD patterns (Fig. 5.1) show only peaks for Ir (ICDD reference pattern 03-065-9327). In the patterns b, c and d, there is a small peak shift for the 111, 220 and 311 peak of 0.1° to 0.3° to higher angles that can be explained by compressive strain and superposition with the other Ir peaks. In the case of pattern a, the shift for these three peaks ranges from -0.6° (311 peak) to 0.4° (111 peak), probably due to more superposition

of the broader peaks. The width of the peaks indicates small crystalline domains. Assuming monodisperse, quasi-spherical particles (k=0.9) without inhomogeneous lattice strain the lower angle half of the 111 peak and the 220 peak were analyzed using the Scherrer equation. Accordingly, the mean diameter of the crystalline domains is 2 nm except for the synthesis with the smallest Ir salt concentration (Tab. 4). In the latter case, the mean diameter is 1.5 nm. This deviation can be explained by the shorter growth time of the nanodots due to lower Ir salt concentration. In accordance with the results from XRD analysis the TEM images (Fig. 5.2) of all samples show single-crystalline nanodots with a typical diameter in the range of 2 nm. Kong's synthesis also resulted in particles with a size in this range [61].
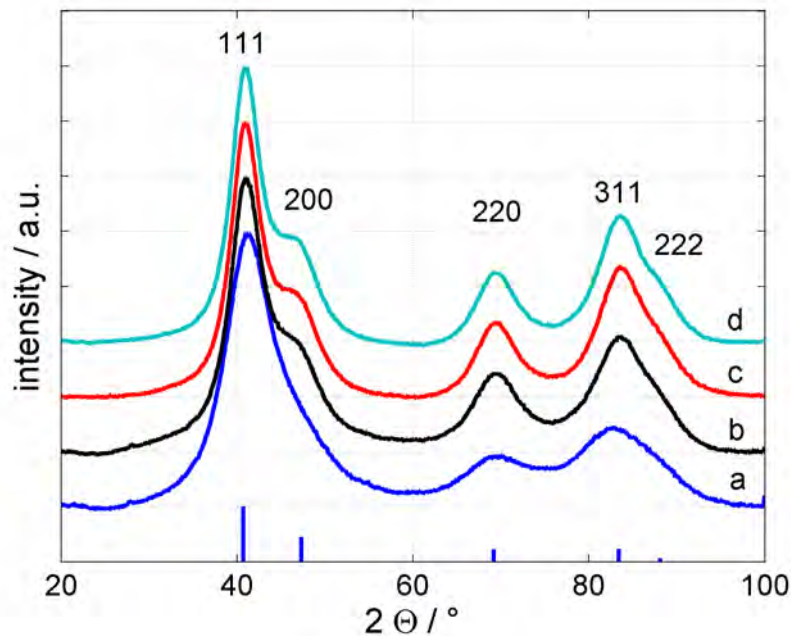
Figure 5.1: *XRD patterns of Ir nanodots synthesized with 20 (a), 40 (b), 60 (c), and 80 mg Ir salt (d). All patterns are normalized to the 111 peak. The line pattern shows the ICDD reference pattern for Ir (03-065-9327).*

Amount of Ir salt used in synthesis	Mean crystallite diameter / nm
20 mg	1.5 ± 0.1
40 mg	1.9 ± 0.2
60 mg	2.0 ± 0.3
80 mg	2.0 ± 0.1

Table 4: *Mean value and standard deviation of the Ir crystallite diameter for syntheses with varying Ir salt concentration determined via Scherrer equation from XRD measurements.*
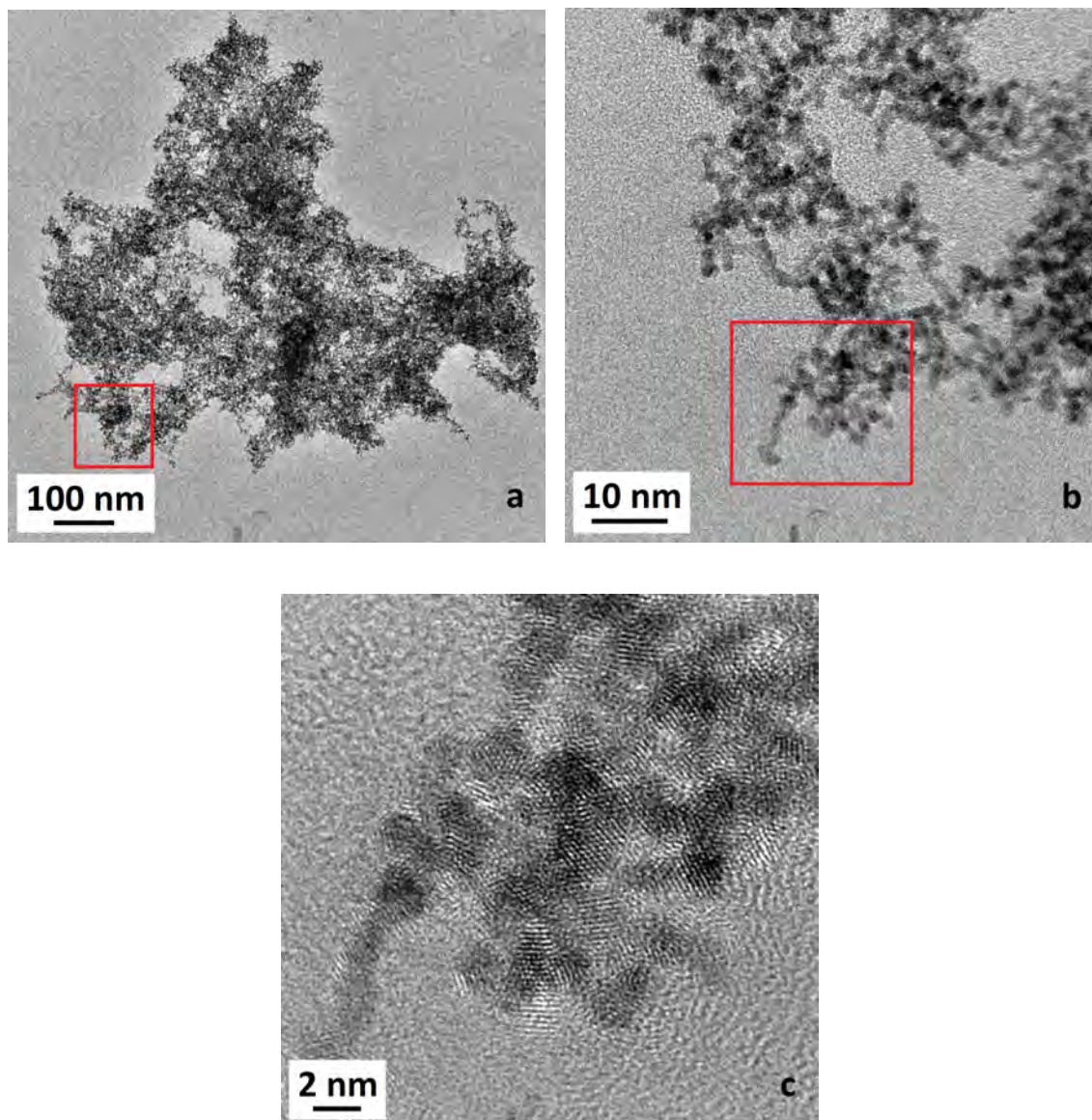
Figure 5.2: *Exemplary TEM images of Ir nanodots. The area marked in a and b is shown with higher magnification in b and c. The TEM images show agglomerates of crystalline Ir nanodots with a typical diameter in the range of 2 nm.*

The Pt nanorod synthesis proved to be robust against changes in the concentration of the different chemicals. As expected, the XRD pattern (Fig. 5.3) shows the Pt peaks to be broadened due to the small crystallite size. The positions of the Pt 111-, 200-, 220-, and 311-peak are shifted by $(0.3 \pm 0.1)°$ towards higher angles. This can be explained by a homogeneous compressive strain compared to bulk material. The peak position does not change after Ir decoration. Since the lattice structure of Pt and Ir is very similar and the amount of Ir is low compared to the amount of Pt, no significant changes in the XRD patterns can be observed. The TEM images show

agglomerates of crystalline Pt nanorods (Fig. 5.4). Ir nanodots were successfully deposited on the Pt nanorods (Fig. 5.4). The nanorods' morphology is stable during Ir decoration. The Ir:Pt atomic ratio determined from EDX spectroscopy is $(6 \pm 3)\%$.
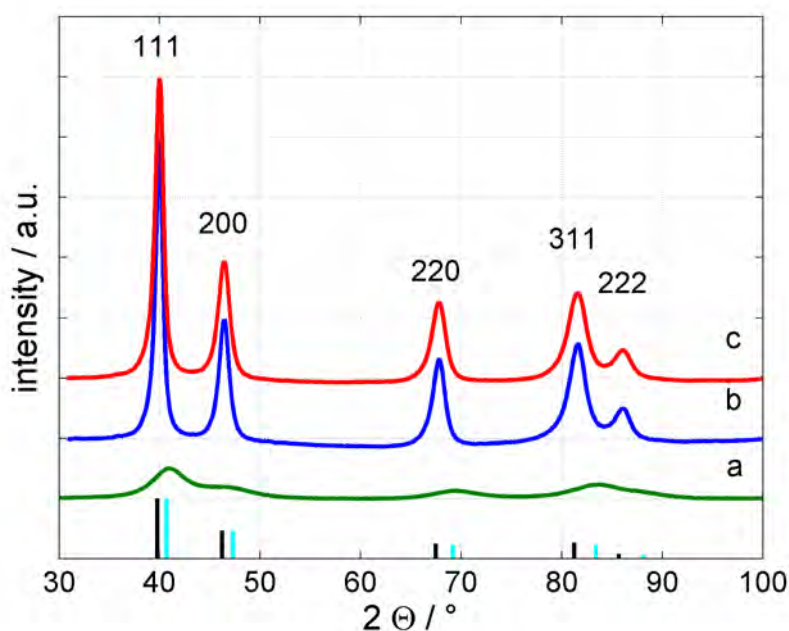
Figure 5.3: *XRD patterns of Ir nanodots prepared without Pt (a), Pt nanorods (b), and Pt nanorods decorated with Ir nanodots (c). The patterns of the Pt based samples (b,c) are normalized to the 111 peak. The line patterns show the ICDD reference patterns of Pt (black, 03-065-2868) and Ir (light blue, 03-065-9327). The hkl values in the figure are identical for both Ir and Pt.*
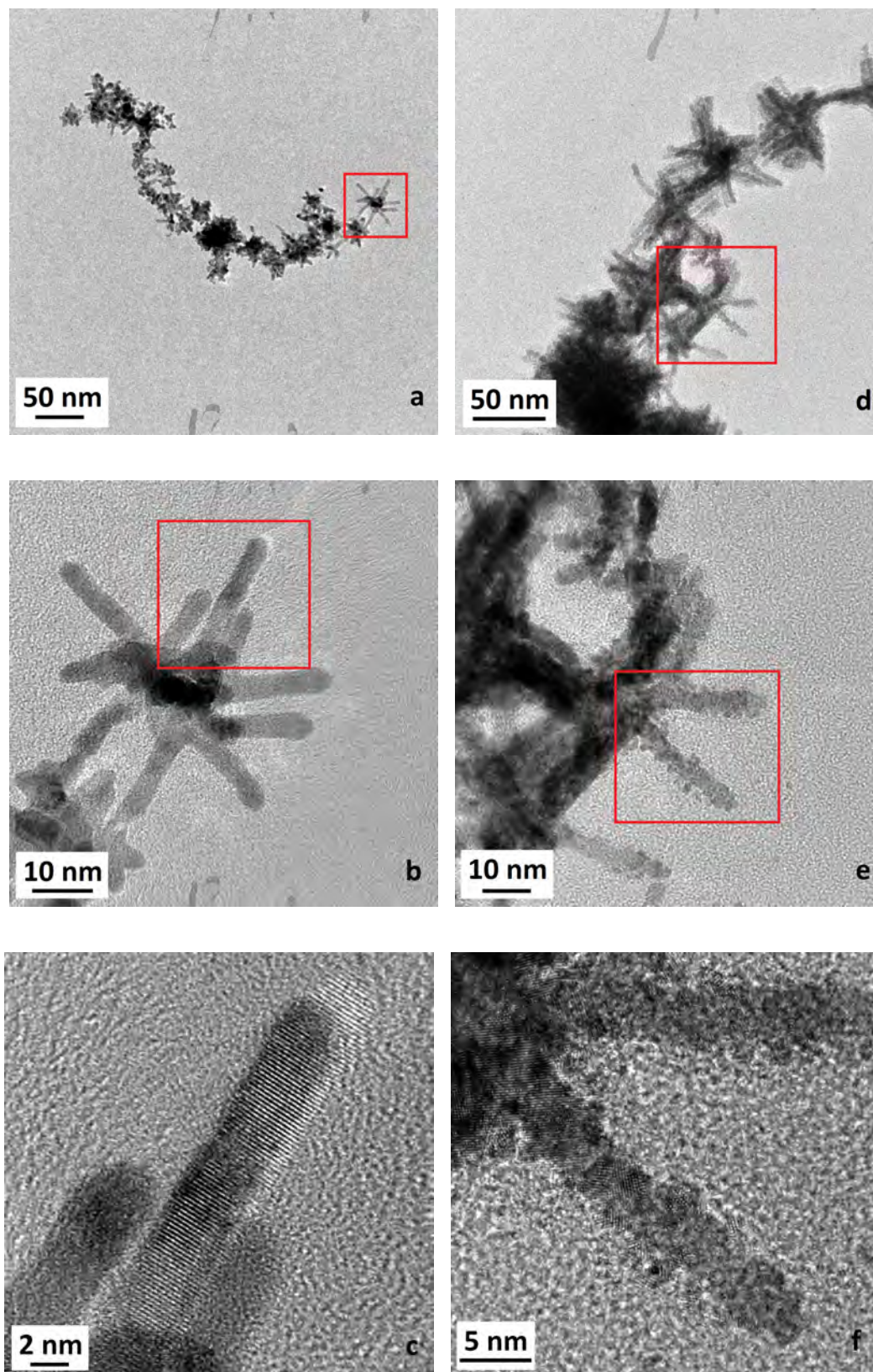
Figure 5.4: *TEM images of Pt nanorods before (a, b, c) and after Ir decoration (d, e, f). The marked areas in a, b, d, and e are shown with higher magnification in b, c, e and f.*

5.2 Electrochemical Characterization

The left row of Fig. 5.5 shows the first and the last wide potential cycle of the activation protocol for the pure Ir nanodots (top), pure Pt nanorods (middle) and Ir decorated Pt nanorods (bottom). In the right row of Fig. 5.5 the last low potential cycle before and after the wide potential cycles are shown for the same samples. To increase the comparability, the pure Pt nanorod sample experienced the Ir nanodot synthesis without Ir salt. Both Ir CVs show a strong decrease of the HUPD (hydrogen under potential deposition) features below 0.3 V vs. MMSE due to oxidation of Ir at least at the nanodots' surface according to the literature [54, 73]. The Pt CVs show an increase of the HUPD signal. This is due to electrochemical cleaning of the surface during the wide potential cycles in accordance with the literature [92]. The CVs of Ir@Pt do not show any significant change in the HUPD charge, but a slight sharpening of the features. This can be explained by a superposition of a decrease of HUPD charge due to Ir oxidation and an increase of HUPD charge due to Pt surface cleaning.

Fig. 5.6 shows CVs of Ir nanodots, Pt nanorods, and Ir decorated Pt nanorods after the activation protocol, meaning after the electrochemical oxidation of the Ir nanodots to IrO_2. The CVs of the Pt nanorods and of the (oxidized) Ir nanodots show the typical features [54]: Pt exhibits ORR activity, but only weak OER activity, whereas the Ir nanodots are a good OER catalyst, but show no pronounced ORR activity. Regarding the Ir@Pt sample, Fig. 5.6 shows that the composite catalyst has pronounced peaks in both the OER and ORR region. Thus, a bifunctional catalyst was obtained. Interestingly, the low potential CV of Ir@Pt at the end of the activation protocol shows no significant change compared to the CV of Pt. The wide potential CV shows a broadening of the ORR peak and a negative shift of the currents at low potentials compared to the CV of pure Pt nanorods. We explain this by the higher amount of O_2 that is produced at OER potentials and that can consequently be reduced at lower potentials.

The OER stability is defined as the OER peak current I_{OER} in the wide potential characterization CV after a certain number of degradation cycles normalized to the initial OER current $I_{OER,0}$. The mean value and standard deviation of four measurements are shown. The ORR stability of the Pt is defined as the hydrogen desorption charge after a certain number of degradation cycles Q_{Hdes} normalized to the initial value $Q_{Hdes,0}$. This charge is correlated with the electrochemically active surface area of the Pt and calculated by integration of the hydrogen desorption currents corrected by the double layer currents [113]. Since in wide potential CVs the ORR currents in the cathodic scan superimpose the HUPD features (Fig. 5.7),

the low potential characterization CVs serve as a basis for the calculation of Q_{Hdes}.
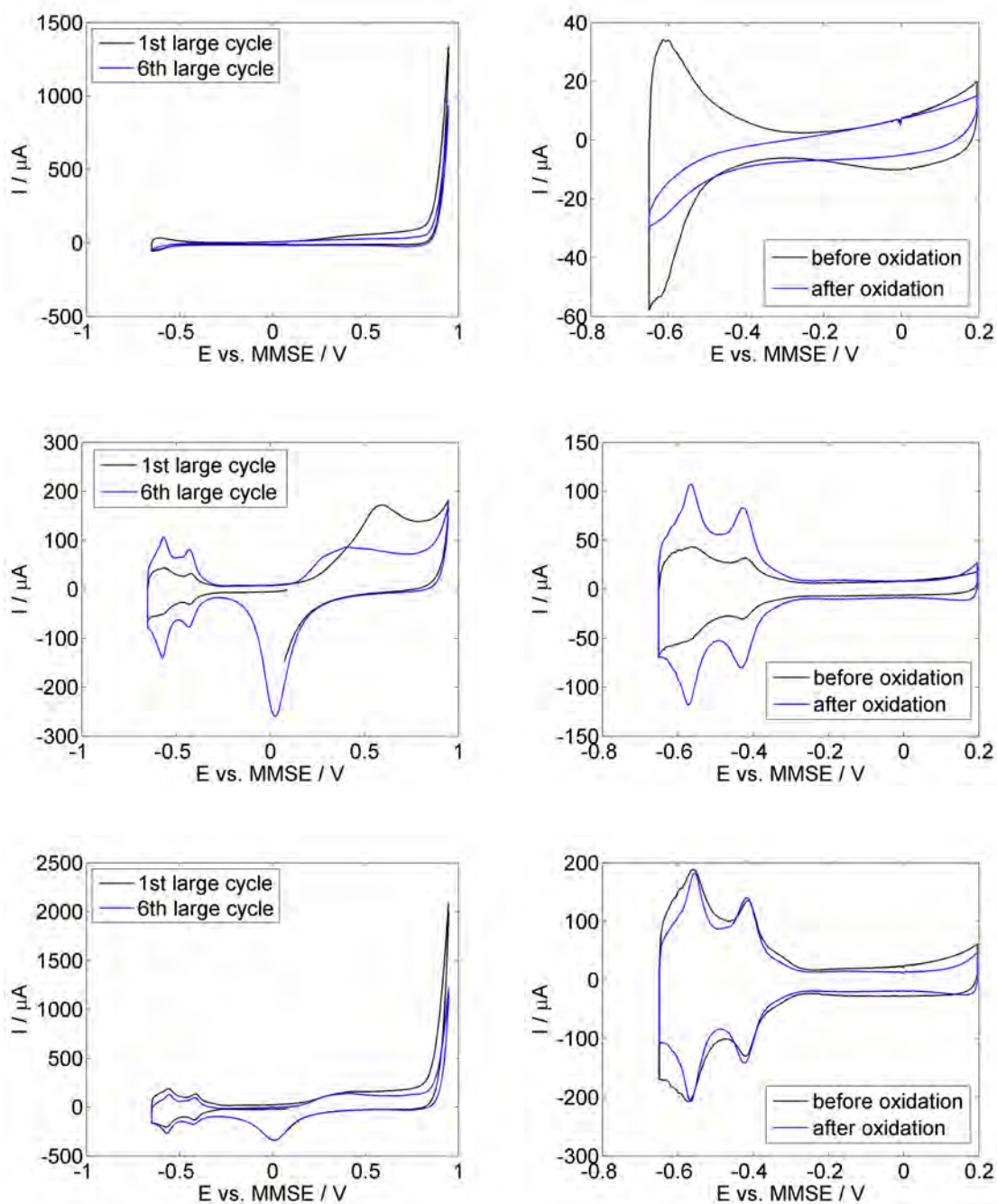
Figure 5.5: *The left row shows the first and the last wide potential cycle of the activation protocol for the pure Ir nanodots (top), pure Pt nanorods (middle) and Ir decorated Pt nanorods (bottom). The right row shows the last low potential cycle before and after the wide potential cycles for the same samples. All CVs were recorded in 2 M H_2SO_4 with a sweep speed of 100 mV s^{-1}. The evolution of the HUPD signals is explained by Ir oxidation, electrochemical Pt surface cleaning and a superposition of both.*
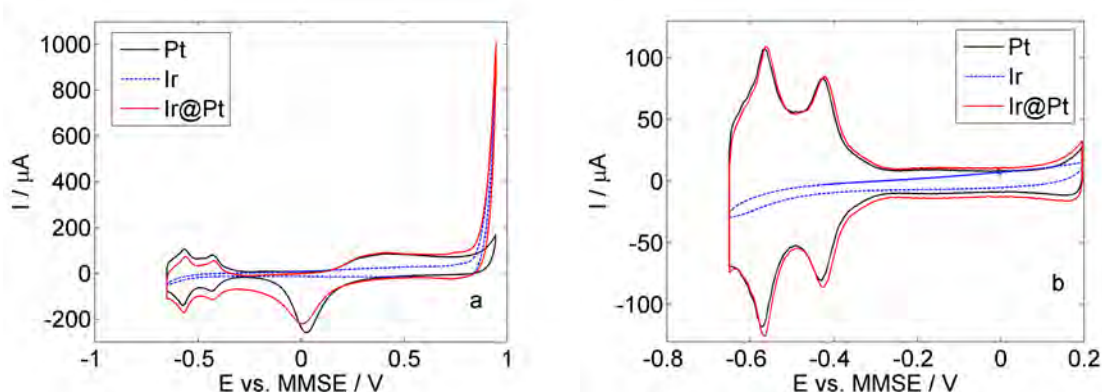
Figure 5.6: *a: CVs of Pt nanorods (black solid), Ir nanodots (blue dashed) and Ir@Pt (red solid) including OER potentials. b: CVs in the lower potential regime used for the determination of the active surface area of the Pt. The image shows typical CVs of Pt and Ir. The lower potential CV of the Ir@Pt sample shows no significant changes compared to the Pt nanorod sample. The wide potential CV of Ir@Pt shows a broadening of the ORR peak and a negative shift of the currents in the lower potential regime. All CVs were recorded in 2 M H_2SO_4 with a sweep speed of 100 mV s^{-1}.*
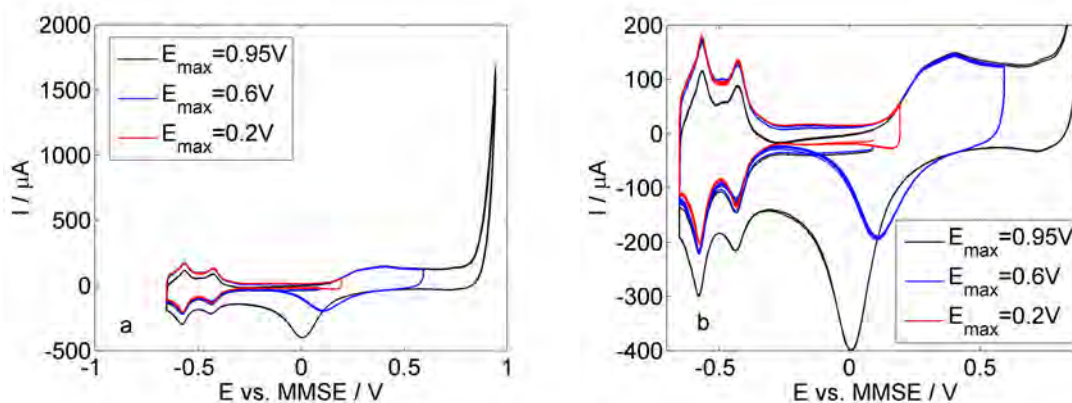
Figure 5.7: *CVs of Ir@Pt with varying upper potential limit in total (a) and with the magnified low potential region (b). The CVs show an influence of the ORR currents on the HUPD signal, when the upper potential limit is in the OER range. The HUPD currents are negatively shifted, and the shift itself is not constant for varying potentials. The CVs were recorded in 2 M H_2SO_4 with a sweep speed of 100 mV s^{-1}.*

Fig. 5.8 shows the OER stability of pure Ir nanodots compared to Ir@Pt during the OER stability protocol and the OER-ORR stability protocol as well as the ORR stability of pure Pt nanorods compared to Ir@Pt during these protocols. The mean

value and standard deviation of four measurements are shown.
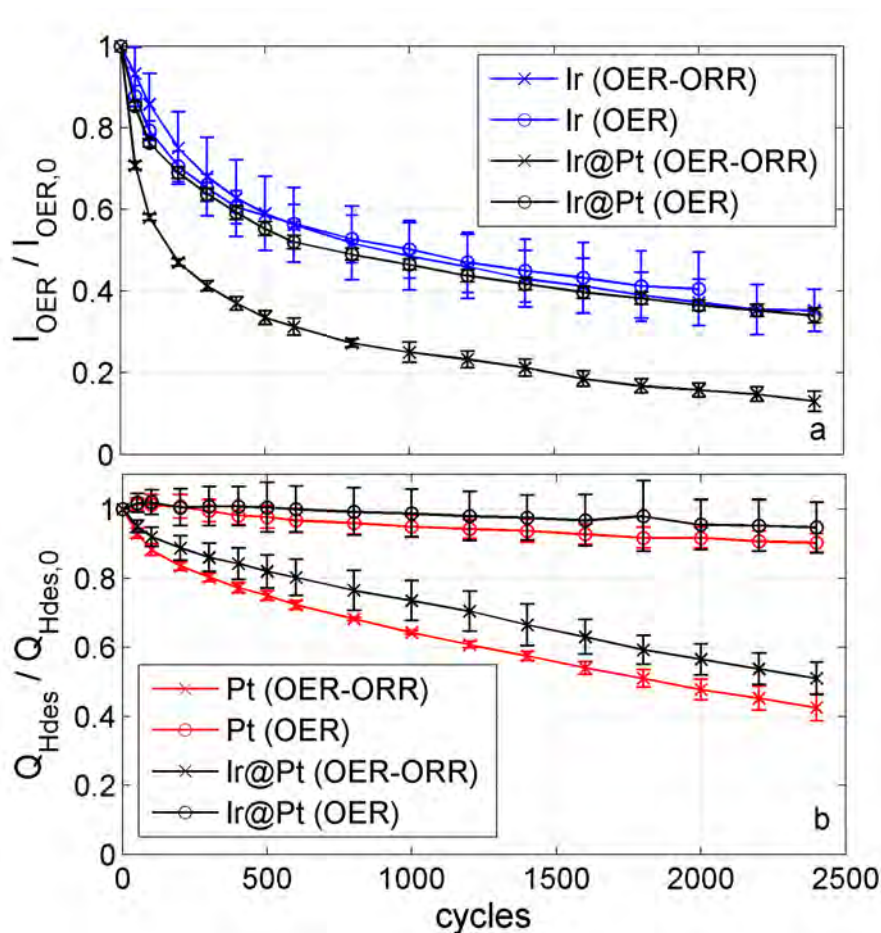
Figure 5.8: *OER stability (a) and ORR stability (b) of the Ir decorated Pt nanorods (black) compared to the unsupported Ir nanodots (blue) and the pure Pt nanorods (red), respectively, as a function of the number of cycles of the OER-ORR stability protocol (crosses) and of the OER stability protocol (circles). Lines serve as guide to the eye. The OER-ORR stability protocol is more degrading for the Pt than the OER stability protocol. Ir decorated on Pt degrades faster during the OER-ORR protocol due to Pt degradation.*

The mean stability values after 2000 cycles are presented in Tab. 5. Fig. 5.9 shows selected characterization cycles from the OER-ORR stability protocol, to illustrate the evolution of the CVs, that serve as base for the stability data shown in Fig. 5.8. The loading of the electrode with Ir is defined as the initial OER current and is (1.1 ± 0.3) mA for pure Ir nanodots and (1.5 ± 0.6) mA for Ir@Pt. The loading with Pt is defined as the hydrogen desorption charge from the low potential characterization CV corrected by the double layer current and is (260 ± 180) mC in the case of pure Pt nanorods and (270 ± 80) mC in the case of Ir@Pt. No influence of the loading on the stability could be observed. The OER stability decreases

strongly during the first hundreds of cycles. Three of four data sets show a decrease of the OER current to roughly 40% after 2,000 cycles, while it is below 20% in the case of Ir@Pt after 2,000 cycles of the OER-ORR stability protocol. In the case of the Ir@Pt samples, there is a small positive offset in the OER stability originating from the OER currents resulting from the Pt support. We explain the difference in the OER stability by the strong Pt degradation when experiencing potential cycling between ORR and OER potentials. This degradation is explained by the repeated build up and reduction of a (hydr)oxide layer on the Pt [8,31]. Comparing the OER stability after 200 cycles of the OER-ORR protocol with the results from Papazisi's study, the unsupported Ir nanodots are as stable as their pure IrO_2 while the Ir decorated on Pt degrades faster than both their $Ir_{0.8}Pt_{0.2}O_2$ and $Ir_{0.2}Pt_{0.8}O_2$ (47% compared to 86% and 60%)[43]. The OER stability of Kong's particles determined from the peak current densities after 2,000 OER cycles was the same in both cases with $(87 \pm 5)\%$ (Pt/Ir-IrO2) and $(85 \pm 5)\%$ (Pt/IrO2) and significantly higher than the OER stability of both the unsupported Ir nanodots and the Pt supported ones (roughly 40% after 2,000 OER cycles)[38]. We assume the higher OER stability of Kong's particles to be due to the contribution of the bigger and, thus, more stable IrO_2 support particles. The results of the ORR stability measurements of pure Pt and Ir@Pt during the OER and OER-ORR stability protocol presented in Fig. 5.8 show in accordance with the literature, that the stability is massively decreased, when not only OER, but also ORR potentials are applied during the protocol [8,31]. While there is no significant difference in the stability values of pure and Ir decorated Pt throughout the OER protocol, the stability is slightly higher in the OER-ORR stability protocol, when Pt is decorated with Ir. We assume, that this difference is due to a partial coverage of the Pt surface by Ir at the beginning. The loss of Ir within the stability protocol leads to an uncovering of formerly blocked Pt surface. The difference in the stability behavior can be explained by an initial blocking of 10 % of the Pt surface by Ir.

sample (stability protocol)	ORR stability after 2000 cycles	OER stability after 2000 cycles
Ir nanodots (OER)	-	40
Ir nanodots (OER-ORR)	-	40
Ir@Pt (OER)	>90	40
Ir@Pt (OER-ORR)	60	<20
Pt nanorods (OER)	>90	-
Pt nanorods (OER-ORR)	<50	-

Table 5: *ORR and OER stability of the different samples after 2000 cycles of both stability protocols.*
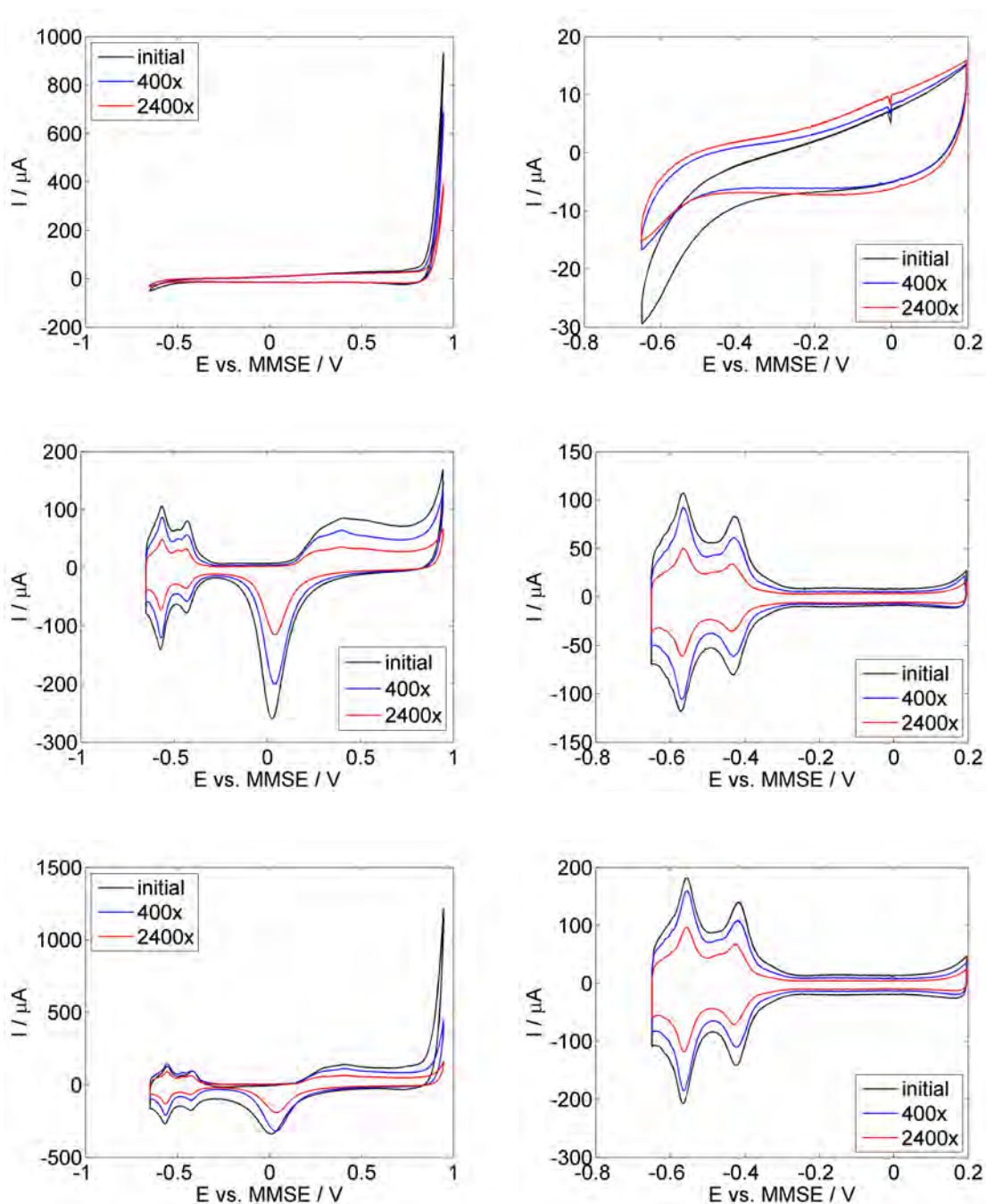
Figure 5.9: *Wide potential characterization CVs (left) and low potential characterization CVs (right) of pure Ir nanodots (top), pure Pt nanodots (middle) and Ir@Pt (bottom) are shown at the beginning, after 400 and 2400 cycles of the OER-ORR stability protocol. All CVs were recorded in 2 M H_2SO_4 with a sweep speed of 100 mV s^{-1}.*

The TEM images of Ir@Pt samples after 400 cycles of the OER-ORR stability protocol support this explanation (Fig. 5.10). In the TEM images, no Ir nanodots could be observed while the nanorod morphology is conserved. Ir is not detected in the EDX measurements of this sample, meaning that the Ir content is below

detection limit (that is below 0.1 weight percent as mentioned in chapter 3.3). Thus, the Ir:Pt atomic ratio equals zero after 400 cycles of the OER-ORR stability protocol (compared to $(6 \pm 3)\%$ initially).
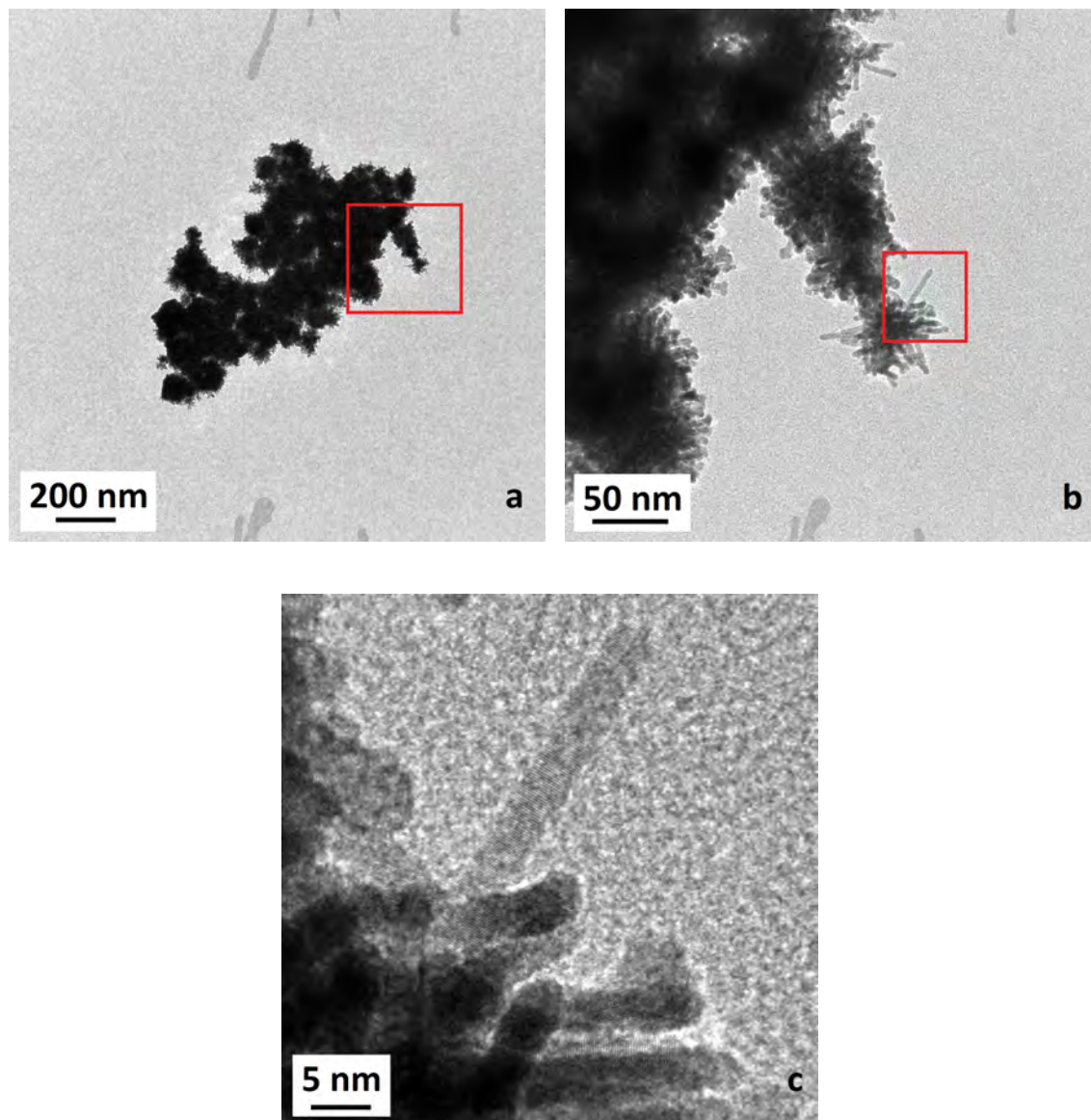
Figure 5.10: *TEM images of Ir decorated Pt nanorods after 400 cycles of the stability protocol. The marked areas in a and b are shown magnified in b and c. The nanorod structure is conserved. Ir nanodots cannot be observed.*

Fig. 5.11 shows a CV of an Ir@Pt sample before, during and at the end of the stability protocol. At the end, the CV looks similar to a CV of pure Pt. To study quantitatively, if there are Ir related OER currents observable in the last CV, we defined a ratio of the OER peak current and the second hydrogen desorption peak current at around -0.4 V vs. MMSE $I_{OER}/I_{2.HdesPeak}$. $I_{2.HdesPeak}$ is related to the

active Pt surface area and, thus, the ORR. This current was taken from the low potential CVs and corrected by the double layer current. The figure shows the mean and standard deviation of four measurements. As shown in Fig. 5.11, this ratio is in the range of 2 throughout the whole stability protocol for a pure Pt nanorod sample. In the case of the Ir decorated Pt nanorods, the ratio is much higher initially due to the Ir loading that leads to much higher OER currents. Within the stability protocol this ratio decreases fast, meaning a stronger decrease of the OER current than of the ORR-related hydrogen desorption current. Interestingly, the ratio does not reach the values of pure Pt even at the end of the stability protocol. Therefore, we suggest that there is still a small amount of Ir left on the Pt nanorods even after 2,400 cycles. This amount is too small to be detectable with EDX spectroscopy, which measures integral over the sample's volume. Since the Ir was deposited on the support particles, the surface ratio of Ir to Pt is higher than the volume ratio. Since cyclic voltammetry is a surface sensitive method, it is capable of detecting Ir (oxides) even below the EDX detection limit.
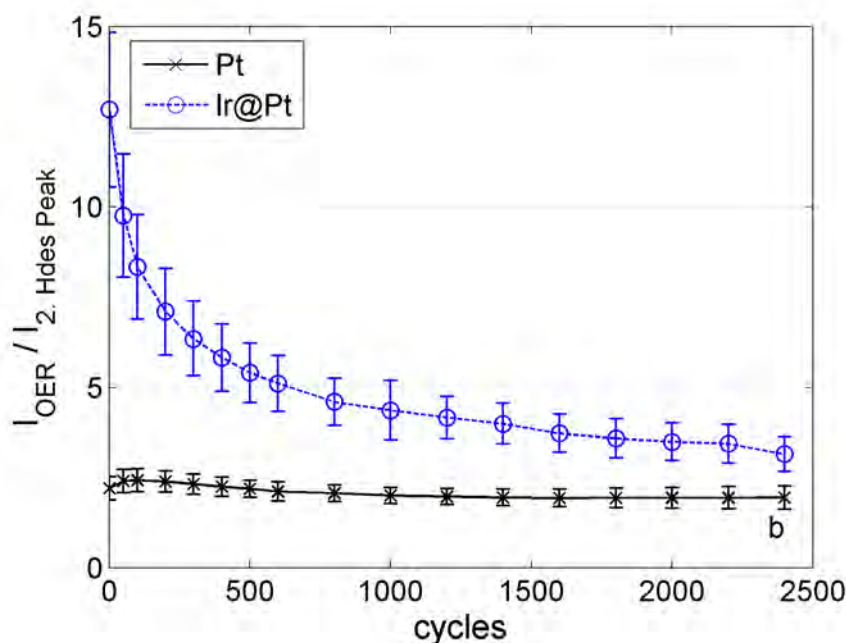
Figure 5.11: *Ratio of the OER peak current and the second hydrogen desorption peak current of the low potential CV corrected by the double layer current as function of the number of stability cycles. Lines serve as guide to the eye.*

5.3 Influence of Annealing

During the previously presented studies the question arose, if the stability of Ir@Pt can be increased by a mild annealing procedure, that does not harm the nanos-

tructure of the particles and might improve the adhesion of the Ir nanodots on the Pt support. This subsection reports on the influence of annealing procedures on the structural and electrochemical properties of Ir@Pt. As preliminary study, the thermal stability of pure Ir nanodots and pure Pt nanorods was investigated via XRD.

5.3.1 Structural Characterization

Before the annealing of the Ir@Pt samples, XRD measurements were performed to gain insights in the temperature dependent stability of the Ir and Pt nanoparticles (Fig. 5.12 and 5.13). The annealing procedure is described in chapter 3.4. The samples were annealed under a synthetic air atmosphere. The XRD patterns were recorded at room temperature.
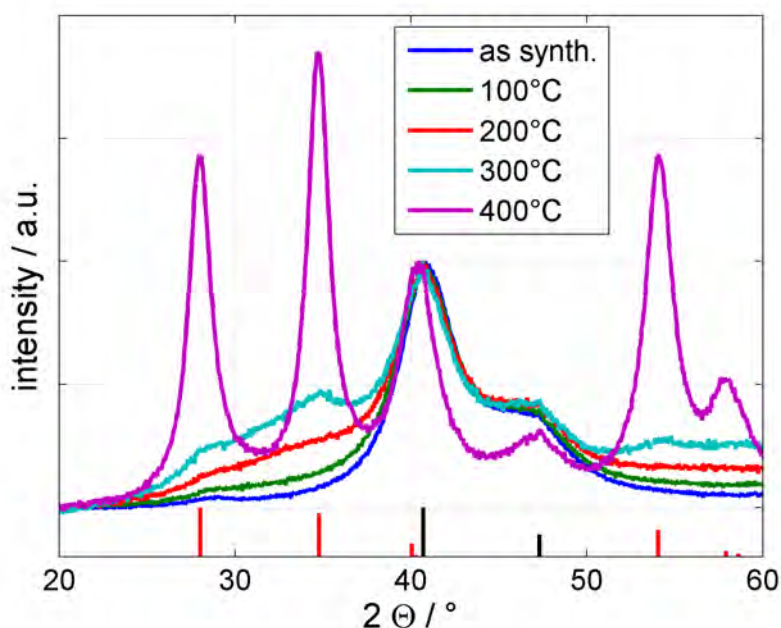
Figure 5.12: *XRD patterns of Ir nanodots as synthesized and after annealing at 100, 200, 300 and 400° C. All patterns were recorded at room temperature and are normalized to the 111 peak of Ir. The line patterns show reference patterns for Ir (black) and IrO$_2$ (red).*

The XRD measurements of Ir nanodots (Fig. 5.12) show the evolution of IrO$_2$ peaks with rising annealing temperature. They lead to a broad feature after annealing at 200°C, get observable after annealing at 300°C and are the dominant features after annealing at 400°C. The shape of the Ir mean peaks is stable even after annealing at 300°C. In other words, the crystallite size does not change. After annealing at 400°C the Ir peak width strongly decreased. This can be explained by the growth

of the crystallites at higher temperatures - probably due to recrystallization of agglomerates.

Fig. 5.13 shows, that the crystallite size is stable even after annealing at 300°C. After annealing at 400°C the peaks narrow due to growth of the mean crystallite size. This might be explained by a change of the shape from rodlike to quasi-squerical and by recrystallization of agglomerates. The peak shift to smaller angles is explained by a loss of compressive strain or in other words by a relaxation of the crystals' lattice.
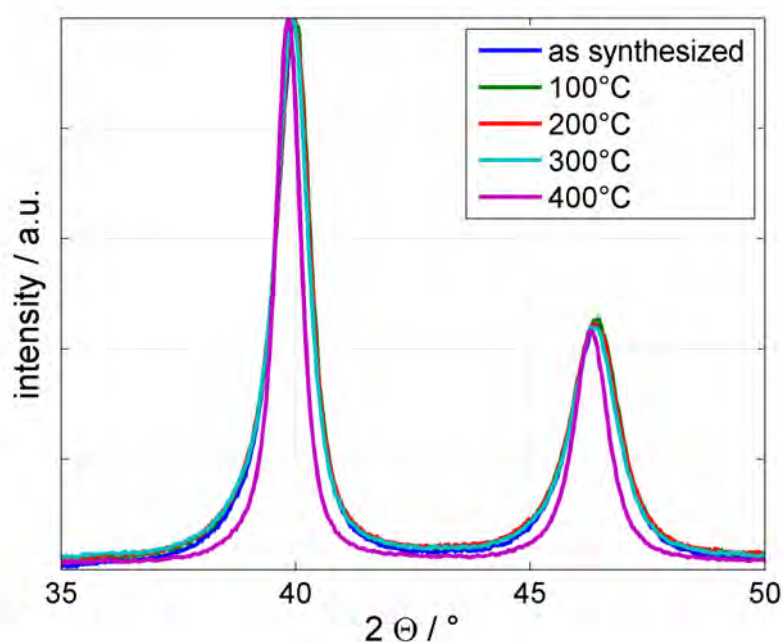
Figure 5.13: *XRD patterns of Pt nanorod after synthesis and after annealing at 100, 200, 300 and 400°C. All patterns were recorded at room temperature and are normalized to the Pt 111 peak.*

To avoid temperature induced particle degradation, 200°C were chosen as annealing temperature. To avoid oxidation of the nanoparticles the Ir@Pt samples were annealed under Ar atmosphere. The annealing procedure was performed in a tube furnace. The temperature was held on 200°C for 6 hours.

Fig. 5.14 shows TEM images of the annealed Ir@Pt nanoparticles. Rod-like structures can still be observed, but with a lower aspect (meaning length-to-diameter) ratio. Also nanodot-sized structures are observable.
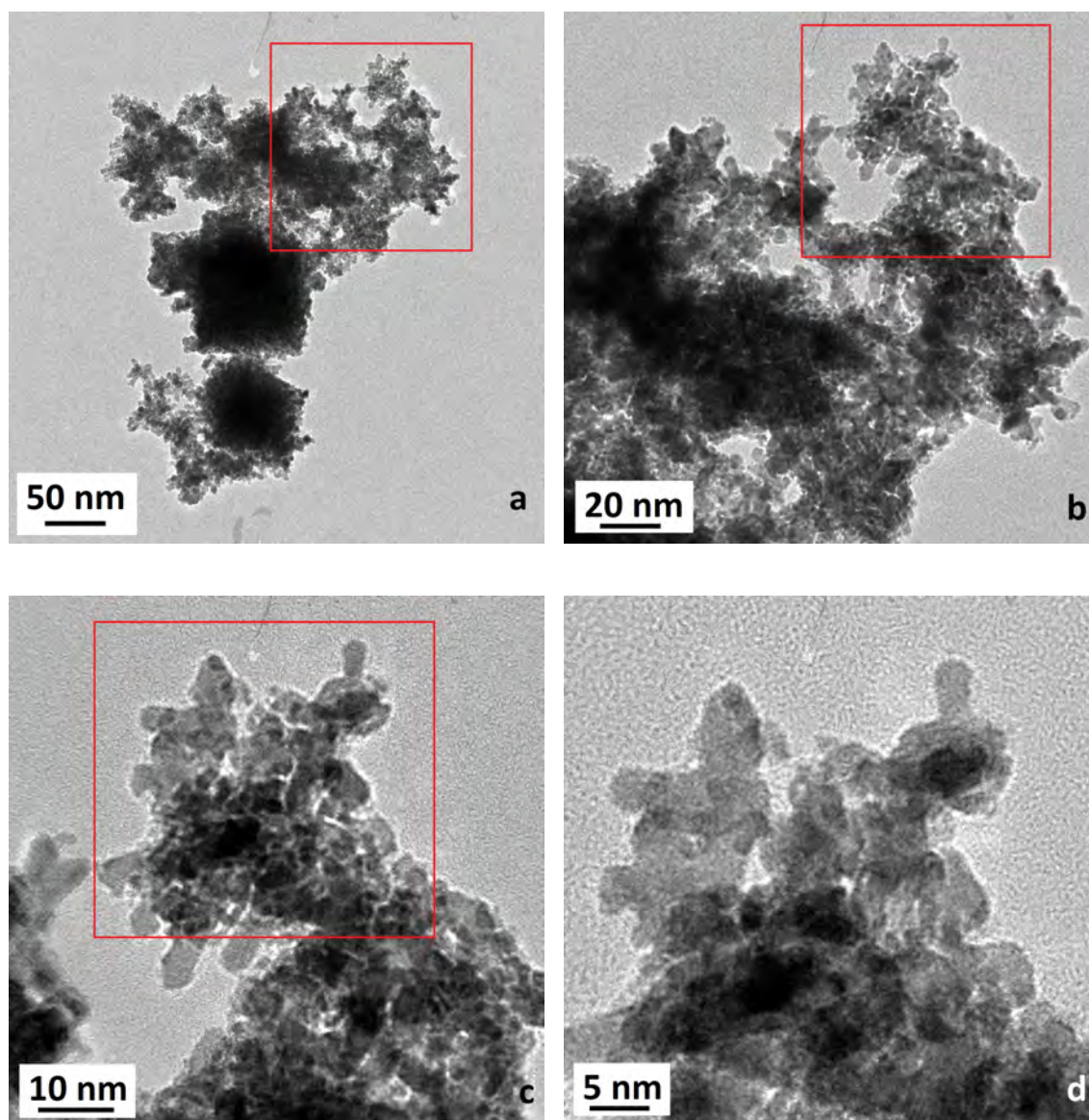
Figure 5.14: *TEM images of Ir@Pt annealed at 200° C under Ar. The markes areas in a,b and c are shown with higher magnification in b,c and d.*

5.3.2 Electrochemical Characterization

The behavior of annealed, pure Pt nanorods and of annealed Ir@Pt during the activation protocol (Fig. 5.15) does not differ from the behavior of the samples, that were not annealed: the HUPD features of pure Pt nanorods grow due to electrochemical cleaning. That the change of the intensity of the HUPD features of annealed Ir@Pt is small, is explained by a superposition of the Ir oxidation to IrO_2 leading to a intensity loss of the HUPD features and the electrochemical cleaning of the Pt surface leading to a gain in intensity of the HUPD features. A sharpening of the features can be observed in accordance with the former results.
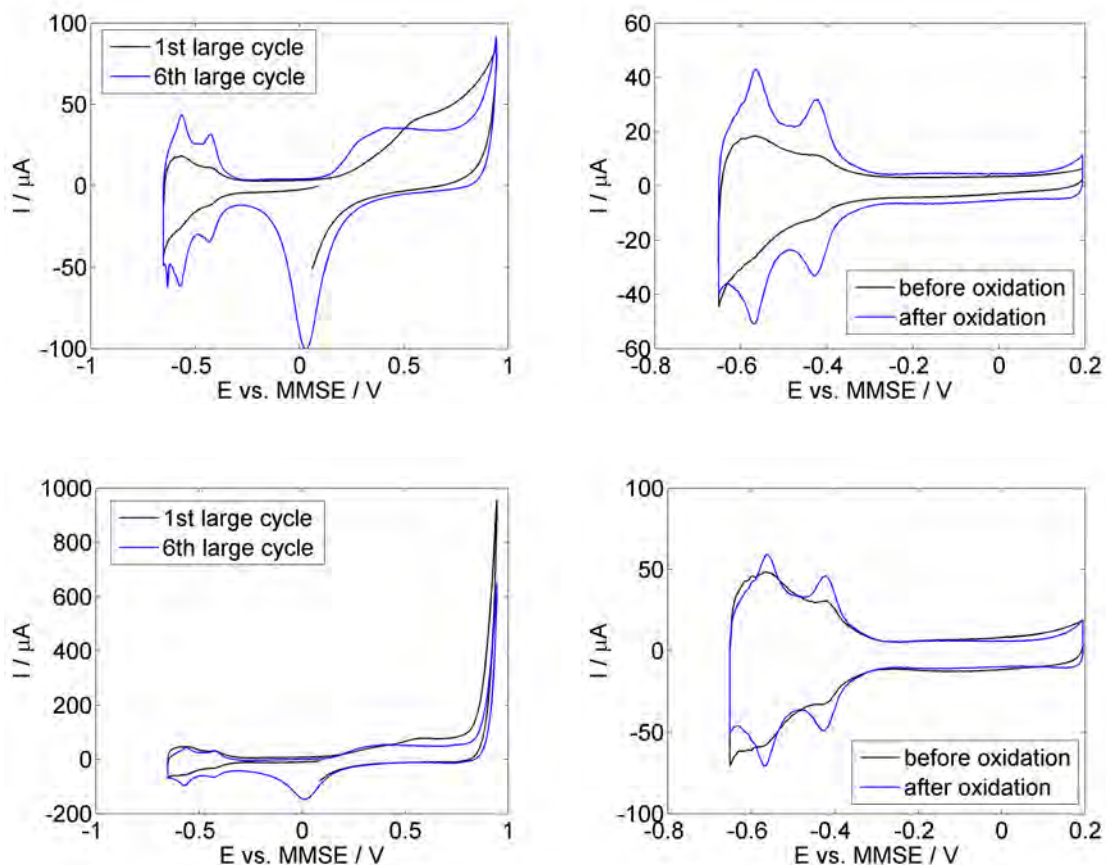
Figure 5.15: *The first and the last wide potential cycle of the activation protocol (on the left) and the last low potential cycle before and after the wide potential cycles (on the right) for annealed, pure Pt nanorods (top) and annealed Ir@Pt (bottom) are shown. All CVs were recorded in 2 M H_2SO_4 with a sweep speed of 100 mV s^{-1}.*

The CV of the annealed Ir@Pt sample does not differ significantly from the CV of the Ir@Pt sample, that was not heat-treated (Fig. 5.16).
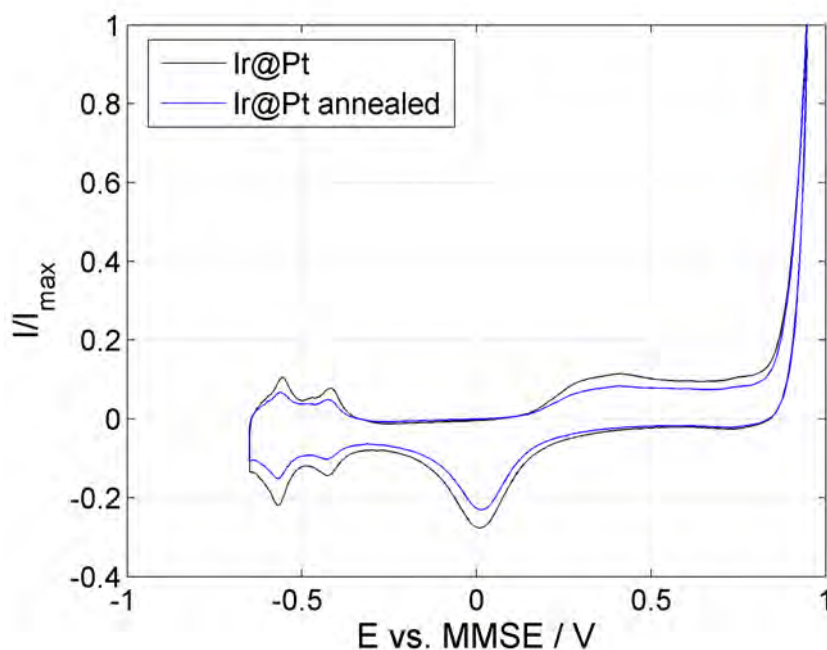
Figure 5.16: *CVs of the annealed Ir@Pt sample (blue) and the Ir@Pt sample, that was not heat-treated (black). Scan rate: 100 mV s^{-1}. Both CVs are normalized to the peak current in order to enable better comparability. No significant difference is observable.*

The stability of the annealed Ir@Pt was studied with the OER-ORR stability protocol as described before and compared to the results for Ir@Pt, that was not annealed (Fig. 5.17). The Ir loading of the annealed Ir@Pt, defined as initial OER current, was (660 ± 490) μA, while the initial Pt loading, defined as hydrogen desorption charge from the low potential CV corrected by the double layer current, was (80 ± 54) μC. This is significantly lower than tha values for the Ir@Pt samples, that were not annealed $((1.5 \pm 0.6)$ mA and (270 ± 80) mC $)$. This can be exlained by a lower concentration of the dispersion with the annealed nanoparticles and by a loss of mass specific surface area due to a higher degree of agglomeration of the particles and a slight change of the Pt nanorod shape towards a lower aspect ratio, that are both induced by the annnealing procedure. No influence of the loading on the stability could be observed. Fig. 5.17 shows the OER and ORR stability of the annealed Ir@Pt samples compared to the Ir@Pt samples, that were not heat treated. Again, the mean and standard deviation of four measurements are shown. Although the initial ORR stability of the annealed sample is slightly higher, this trend does not hold during the whole stability protocol. At the end of the protocol, no significant influence of the annealing on the ORR stability can be observed. The OER stability of the annealed sample is slightly lower than that of the untreated sample.
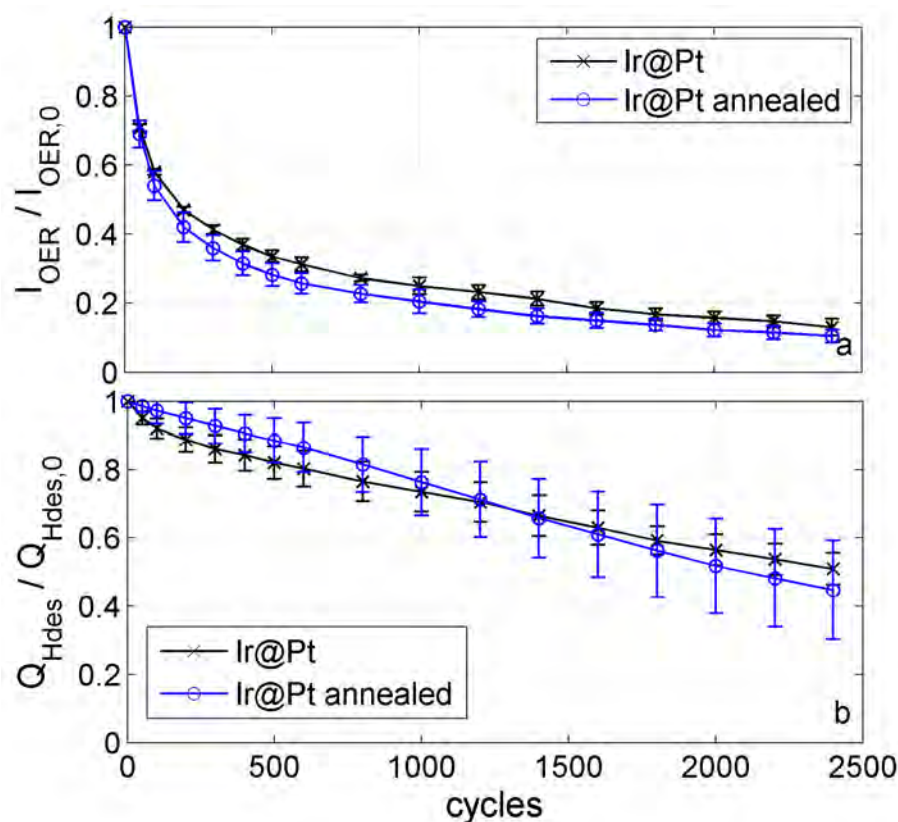
Figure 5.17: *OER stability (a) and ORR stablity (b) of an annealed Ir@Pt sample (blue, circles) compared to an Ir@Pt sample, that was not heat treated (black, crosses) during the OER-ORR stability protocol.*

5.4 Conclusion

The synthesis of Ir nanodots with a size of 2 nm without support as well as deposited on Pt nanorods could successfully be conducted. The nanorods' morphology is stable during Ir synthesis. The Ir nanodots are well dispersed on the Pt support particles. To investigate the stability of the bifunctional Ir@Pt OER-ORR catalyst towards simulated charge-stop and charge-discharge operation of a VARFB, OER stability protocols as well as OER-ORR stability protocols were conducted. The OER currents of unsupported Ir decrease to 40% of the initial value after 2,000 cycles of both stability protocols. The degradation of Ir deposited on Pt is the same in the case of the OER stability protocol, but in the case of the OER-ORR stability protocol, the OER current is less than 20% of the initial value after 2,000 cycles. This is due to the rapid Pt degradation when experiencing alternating ORR and OER potentials. The active surface area of Pt with and without Ir decoration is still more than 90% of the initial value after 2000 cycles of the OER stability protocol. In the case of the OER-ORR stability protocol, the pure Pt nanorods' active surface area degrades to less than 50%, while it is in the range of 60% when the Pt is

decorated with Ir. This can be explained by the initial blockage of Pt surface by Ir and degradation of Ir during the stability protocol and consequently, uncovering of formerly blocked Pt surface. While no Ir is observable in the Ir@Pt sample after 400 cycles of the OER-ORR stability protocol in EDX and TEM measurements, the analysis of data recorded with the more sensitive cyclic voltammetry indicated the presence of small amounts of Ir left even at the end of the stability protocol. A mild annealing procedure was conducted aiming at an increase of the stability by an improved adhesion of the Ir nanodots to the support, but did not increase the OER or ORR stability of Ir@Pt.

To take a view on perspectives concerning bifunctional OER-ORR catalysts: Pt degrades strongly under cycling between OER and ORR potentials. It is, thus, helpful to protect Pt from OER potentials, meaning the use of separated OER and ORR catalysts. If one accepts this degradation, one has to take into account, that the stability of Ir deposited on Pt suffers from the Pt degradation. Nevertheless, the stepwise synthesis allows a uncomparably higher control of the morphology of the composite catalyst and, thus, the electrochemical properties including the stability. And the interaction of the composite parts is, yet, hardly understood. For further research on bifunctional OER-ORR catalysts, it might be useful concerning the stability, to take an Ir-based catalyst as support and deposit Pt on it. Another option might be, to deposit both catalysts on a stable support like SnO_2.

6 Stability of RuO_2 Nanoparticles decorated with Ir Nanodots

Since the conditions during charge in the oxygen electrode of a VARFB (or PEM URFC or PEM water electrolyzer) are known to be harsh due to the acidic environment and the high potentials, one major challenge is to improve the nanocatalyst's stability. Since RuO_2 is generally recognized as one of the OER catalysts with the highest activity, but has a poor stability in acidic systems and IrO_2 is more stable, but less active, usually Ir-Ru-based mixed oxides are used as OER catalyst in acidic systems. In the literature it is reported for the bulk and the nanoparticle form, that nanosegregated Ru-Ir mixed oxides possess a similar activity but a 3 to 4 times higher stability compared to homogeneous Ru-Ir mixed oxides (see chapter 2.5 and [15]). The aim of this study is to decorate RuO_2 nanoparticles with Ir nanodots that are oxidized to IrO_2 later on, at least at the surface, and to compare the OER stability of both single nanoparticle catalysts and the composite catalyst. The advantage of this stepwise approach is the possibility to control more easily the morphology and thus activity and stability of both nanoparticle species. The particles' structural properties are investigates using XRD and TEM. Their stability towards an OER stability protocol is studied in a three electrode cyclic voltammetry setup. The influence of a mild annealing procedure on the structure and electrochemical stability is also investigated. Detailed information about the experimental methods can be found in chapter 3. Parts of the content are currently submitted to the Journal of Physical Chemistry C and under review.

6.1 Structural Characterization

The results for pure Ir nanodots are shown in chapter 5.1. For the synthesis of Ir nanodots in the presence of RuO_2 nanoparticles, 20 mg RuO_2 were used and the amount of Ir salt was varied between 0 and 100 mg. Fig. 6.1 shows TEM images of Ir nanodots being well dispersed on the bigger RuO_2 nanoparticles. EDX measurements yield an Ir:Ru atomic ratio of $(10 \pm 4)\%$ for the RuO_2 sample treated with 100 mg Ir salt. Fig. 6.2 shows the XRD patterns of RuO_2 nanoparticles as bought and after syntheses with 0, 20, 40, 60, and 80 mg Ir salt and of Ir nanodots without RuO_2 support. The RuO_2 peak positions of the as bought sample are shifted to higher values compared to the calculated positions (ICDD pattern 03-065-2824). The shift averaged over the 110, 101, 211, 220, and 002 peak is $(0.32 \pm 0.08)°$. This shift might be explained by a homogeneous compressive strain of the nanoparticles. The synthesis procedure conducted without Ir salt does not change the RuO_2 peak

positions compared to the as bought sample. The positions of the mentioned peaks shift to smaller angles after Ir synthesis. The shift does not depend on the amount of added Ir salt and is $(0.08 \pm 0.04)°$. This shift might be explained by a relaxation of the RuO_2 lattice due to interaction with the Ir nanodots or, more probably, by enrichment of IrO_2 in the RuO_2 particles and overlap of the very similar XRD patterns.
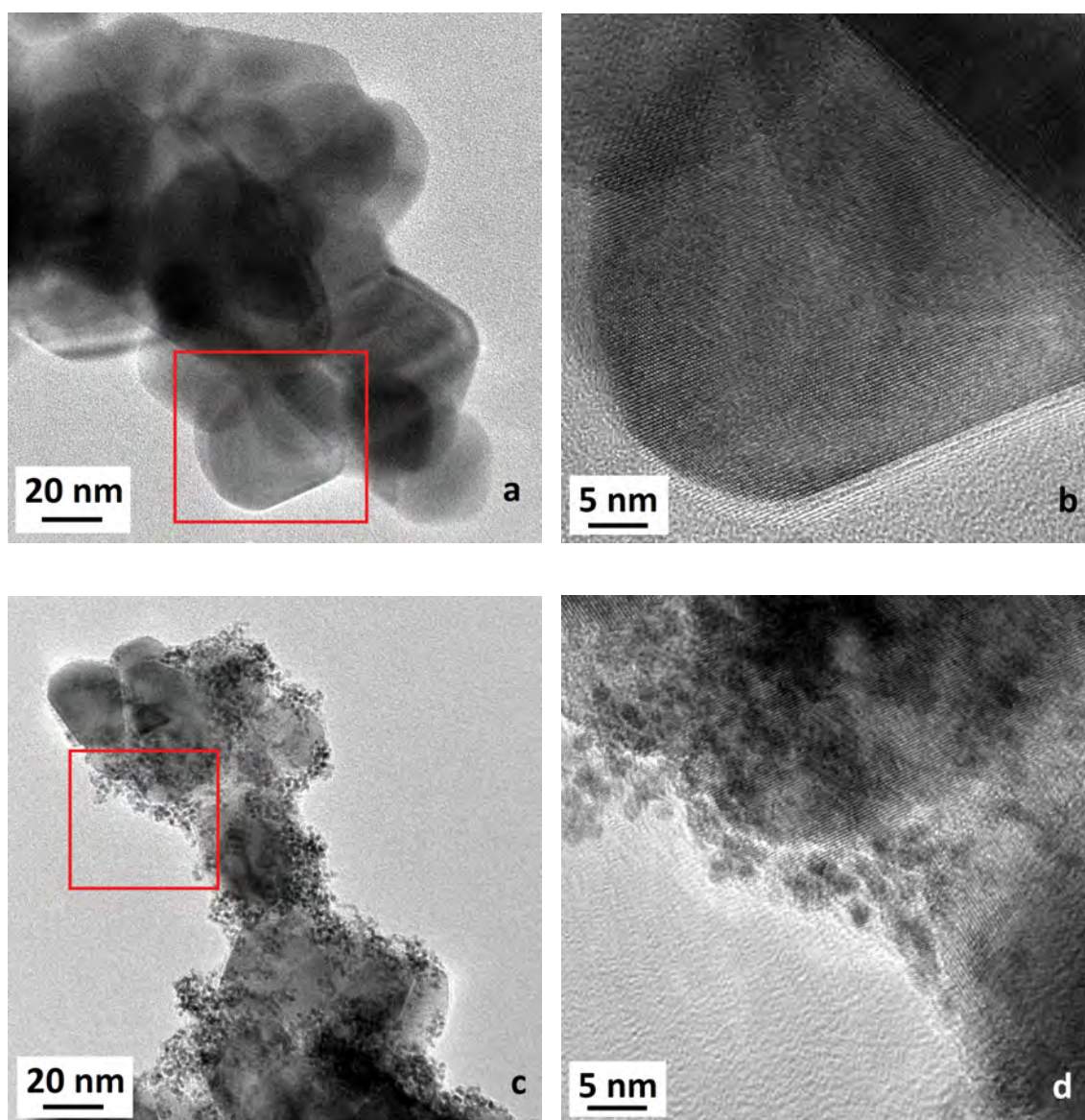
Figure 6.1: *a and b: TEM images of as bought RuO_2 nanoparticles. b shows crystalline RuO_2 nanoparticles. c and d: TEM images of the Ir@RuO_2 nanoparticles from the synthesis using 100 mg Ir. The marked area in c is shown with higher magnification in d. The Ir nanodots are well dispersed on the RuO_2 support particles.*
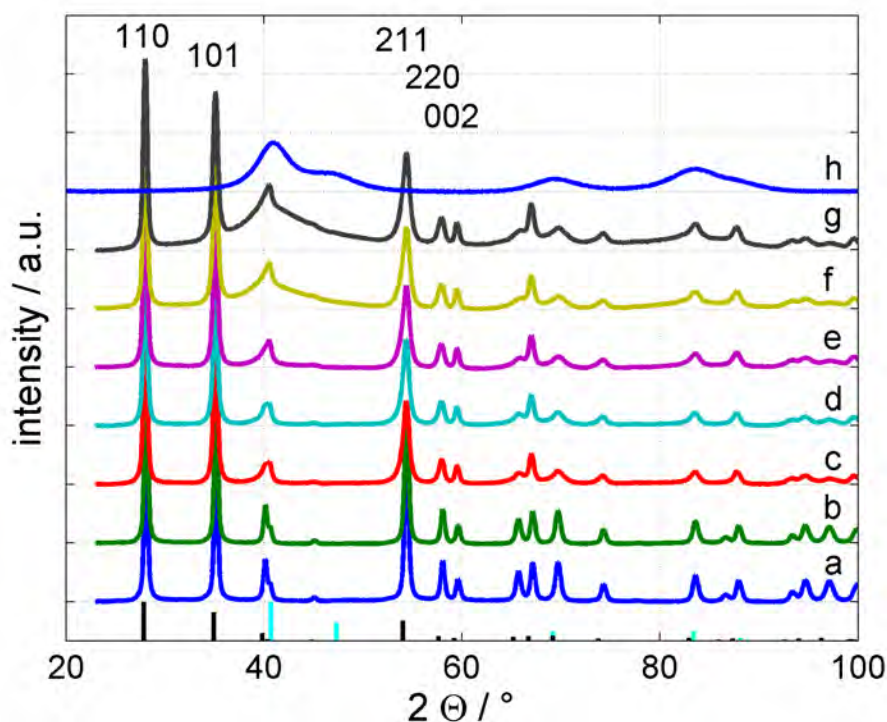
Figure 6.2: *XRD patterns of as bought RuO$_2$ nanoparticles (a), RuO$_2$ nanoparticles after the synthesis conducted without Ir salt (b) and with 20 (c), 40 (d), 60 (e), 80 (f), and 100 mg Ir salt (g) and of Ir nanodots prepared without RuO$_2$ nanoparticles (h). The patterns a - g are normalized to the 110 peak. Selected RuO$_2$ peaks are named in the figure. The line patterns show the ICDD reference pattern of RuO$_2$ (black, 03-065-2824) and Ir (light blue, 03-065-9327).*

The mean crystallite diameters estimated via the Scherrer equation from the 110 and 101 peak for the different samples are shown in Tab. 6. Comparing the peak widths of as bought RuO$_2$ nanoparticles and RuO$_2$ nanoparticles after the synthesis conducted with 100 mg Ir salt shows an apparent decrease of the mean crystallite size from (30.1 ± 0.4) nm to (18.4 ± 0.4) nm. An alternative explanation for the peak broadening is an increase in inhomogeneous lattice spacings that might originate from additive inhomogeneous strain due to interaction with the Ir nanodots or by enrichment of IrO$_2$ in the RuO$_2$ particles. The difference in the apparent mean diameter between as bought RuO$_2$ and RuO$_2$ after the synthesis procedure conducted without Ir salt might be explained either by a decrease of the RuO$_2$ crystallite size e.g. by dissolution or by an increase of the lattice inhomogeneities during the synthesis. The TEM images in Fig. 3 show crystalline RuO$_2$ nanoparticles with a mean diameter in the range of the mentioned values.

In the XRD patterns of the samples prepared with 80 and 100 mg Ir salt a broad feature evolves around 40°. According to the XRD patterns of the pure Ir nanodot

Sample	Mean diameter of RuO$_2$ crystallites / nm
RuO$_2$ as bought	30.1 ± 0.4
RuO$_2$ + 0 mg Ir salt	28.5 ± 0.4
RuO$_2$ + 20 mg Ir salt	23.9 ± 3.5
RuO$_2$ + 40 mg Ir salt	24.0 ± 1.2
RuO$_2$ + 60 mg Ir salt	21.5 ± 4.7
RuO$_2$ + 80 mg Ir salt	18.9 ± 5.4
RuO$_2$ + 100 mg Ir salt	18.4 ± 0.4

Table 6: *Mean value and standard deviation of the RuO$_2$ crystallite diameter for different samples estimated from the 110 and 101 XRD peak assuming pure, quasi-spherical RuO$_2$ nanoparticles, that are not inhomogeneously strained.*

samples this feature is attributed to the Ir main peak. Compared to the unsupported Ir sample the Ir main peak is broadened. The TEM images in Fig. 6.1 show Ir nanodots with a typical diameter in the range of 2 nm deposited on the RuO$_2$. Therefore, this peak broadening might be explained by higher lattice strain of the Ir nanodots caused by interaction with the RuO$_2$ support.

6.2 Electrochemical Characterization

In the first low potential CVs of the activation protocol, the Ir HUPD (hydrogen under potential deposition) features can be observed in the Ir and the Ir@RuO$_2$ (from the synthesis with 100 mg Ir salt) data at potentials below 0.3 V vs. MMSE. As shown in Fig. 6.3, these features vanish within few wide potential cycles due to oxidation of Ir at least at the nanodots' surface in agreement with the literature [54, 63]. A decrease of the OER currents is observable for all samples during the activation protocol. Beyond that, no significant changes of the RuO$_2$ can be detected.
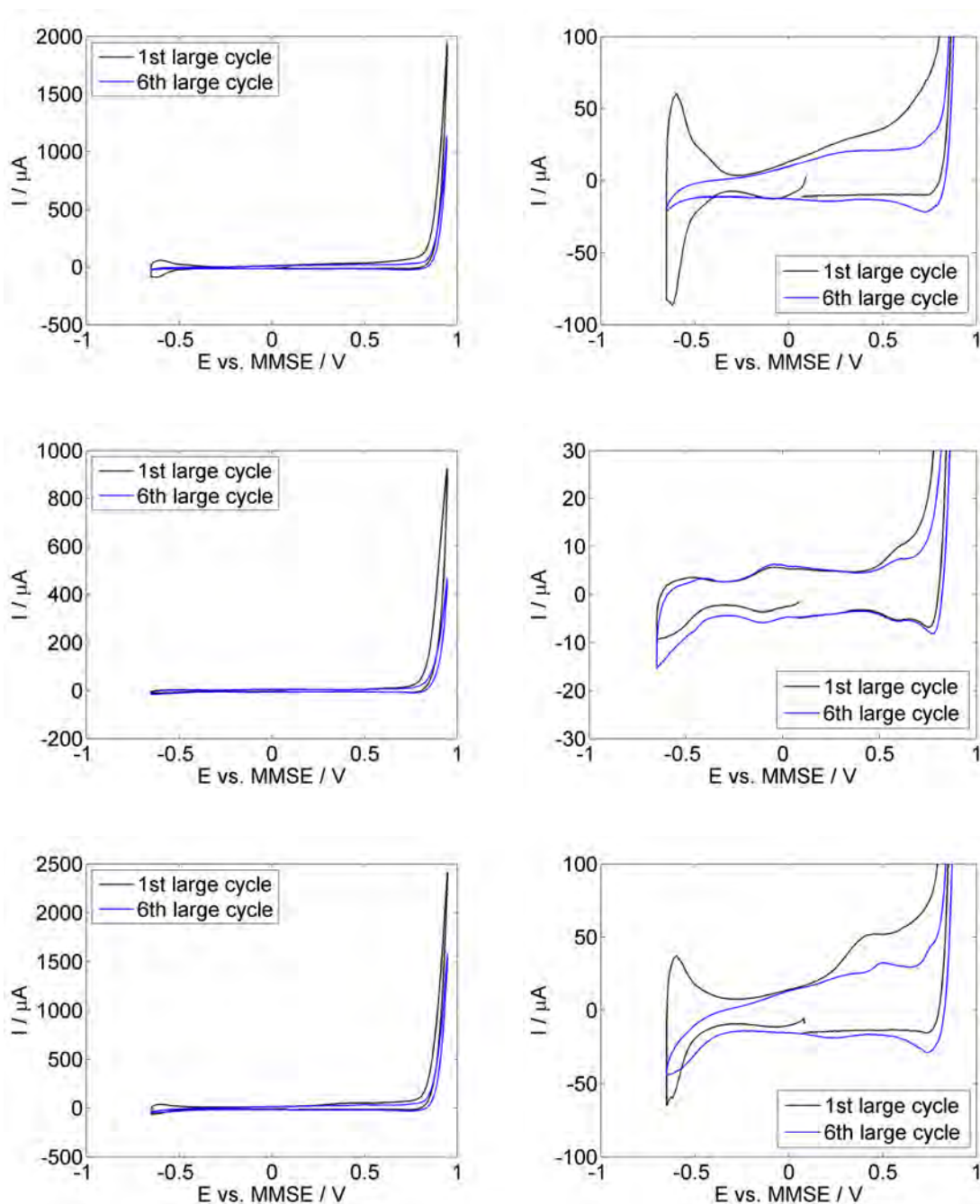
Figure 6.3: *First and 6. wide potential CV of the activation protocol shown in total (left) and with a magnified current axis (right) for Ir nanodots (top), RuO₂ nanoparticles (middle) and Ir@Ru₂ (bottom). Scan rate: 100 mVs⁻¹. The Ir HUPD features vanish within few cycles due to Ir oxidation.*

Fig. 6.4 shows the initial characterization CVs of the stability protocol (after the activation procedure) normalized to the peak current. The CV of the RuO₂ nanoparticles shows the typical Ru^{III}/Ru^{IV} redox couple at -0.1 V vs. MMSE and the Ru^{IV}/Ru^{VI} redox couple at 0.6V vs. MMSE and HUPD features below -0.3 V vs.

MMSE [9,54,78,80]. The CV of the oxidized Ir nanodots shows no distinct features. Probably the redox features are broadened due to the small size of the nanodots. In the Ir@RuO$_2$ CV, a very weak feature can be observed at 0.3 V vs. MMSE that might be attributed to the Ir^{III}/Ir^{IV} redox couple [74, 78]. The onset potential for the OER is nearly the same for all samples - only the one of the Ir@RuO$_2$ CV is a little bit shifted to higher potentials.
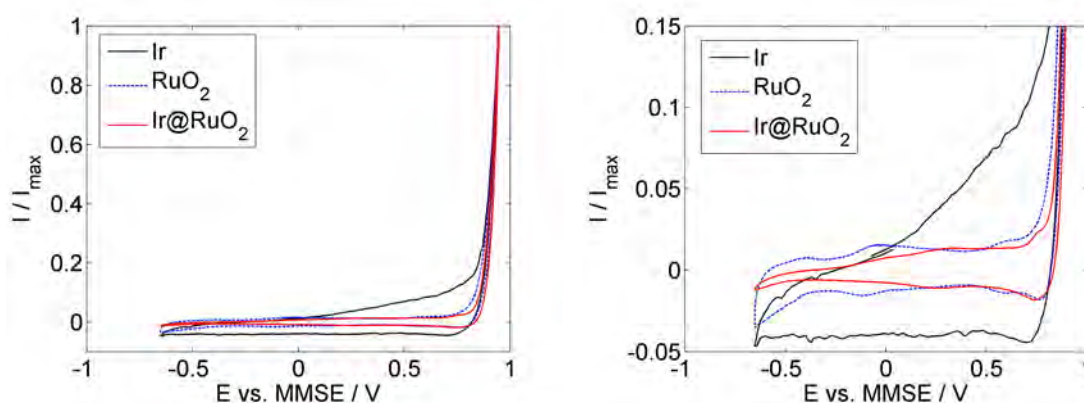
Figure 6.4: *Left: Initial characterization CVs of the stability protocol of Ir nanodots (black solid), RuO$_2$ nanoparticles (blue dashed) and Ir decorated RuO$_2$ nanoparticles (red solid). The currents are normalized to the peak current. Right: Detailled view of the low potential regime of the CVs. All CVs were recorded in 2 M H$_2$SO$_4$ with a sweep speed of 100 mV s^{-1}.*

To evaluate the stability of the catalysts with respect to the OER, the decrease of the OER peak current in the CVs is analyzed. To calculate the OER stability, the OER peak currents of the characterization CVs within the stability protocol were divided by the initial OER peak current. Fig. 6.5 shows, that there is no influence of the loading on the OER stability of RuO$_2$. The loading is defined as initial OER current and ranges over two orders of magnitude: from 26 μA to 2.2 mA.

Fig. 6.6 shows the stability of the three catalysts as function of the number of degradation cycles performed within the stability protocol. The mean values and standard deviation of four measurements were calculated for the stability diagrams.
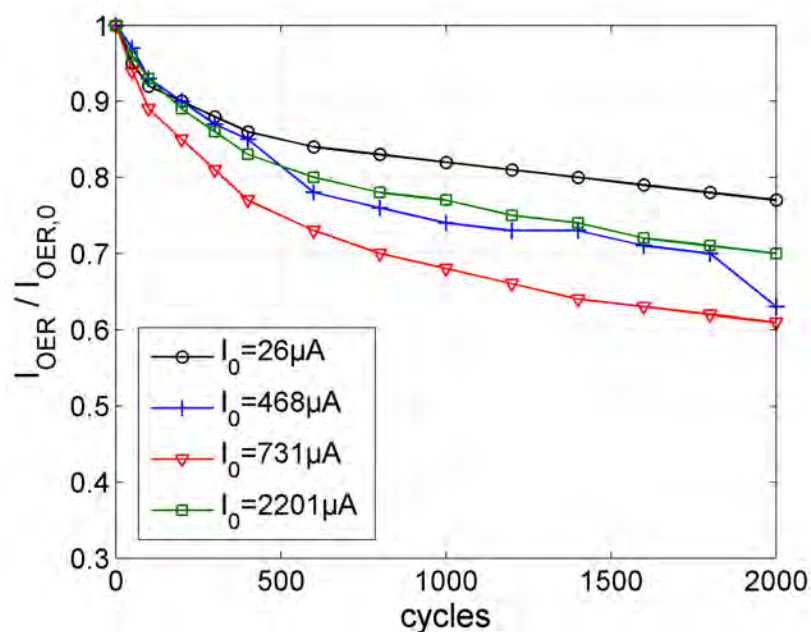
Figure 6.5: *OER stability of RuO$_2$ as function of the number of cycles of the OER stability protocol for different catalyst loadings defined as initial OER currents. Lines serve as guide to the eye.*
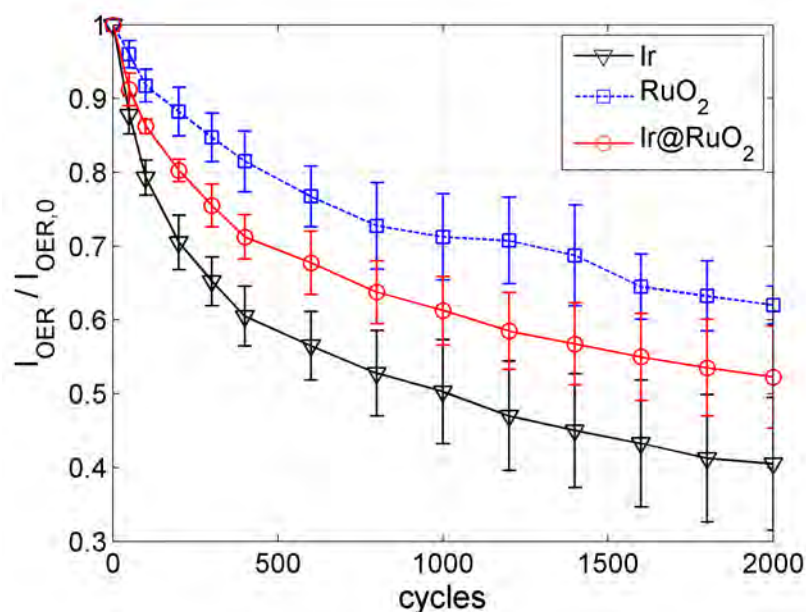
Figure 6.6: *OER stability of RuO$_2$ (blue dashed, squares), Ir (black, triangles) and Ir decorated RuO$_2$ (red, circles) defined as the OER peak current in a characterization CV after the given amount of degradation cycles normalized to the initial OER peak current. The lines serve as guide to the eye. Each curve shows the mean and standard deviation of four measurements.*

Fig. 6.7 shows selected characterization cycles from the stability protocols, to illustrate the evolution of the CVs, that serve as base for the stability data shown in Fig. 6.6. TEM images of Ir decorated RuO_2 nanoparticles after 2,000 cycles of the stability protocol are shown in Fig. 6.8.
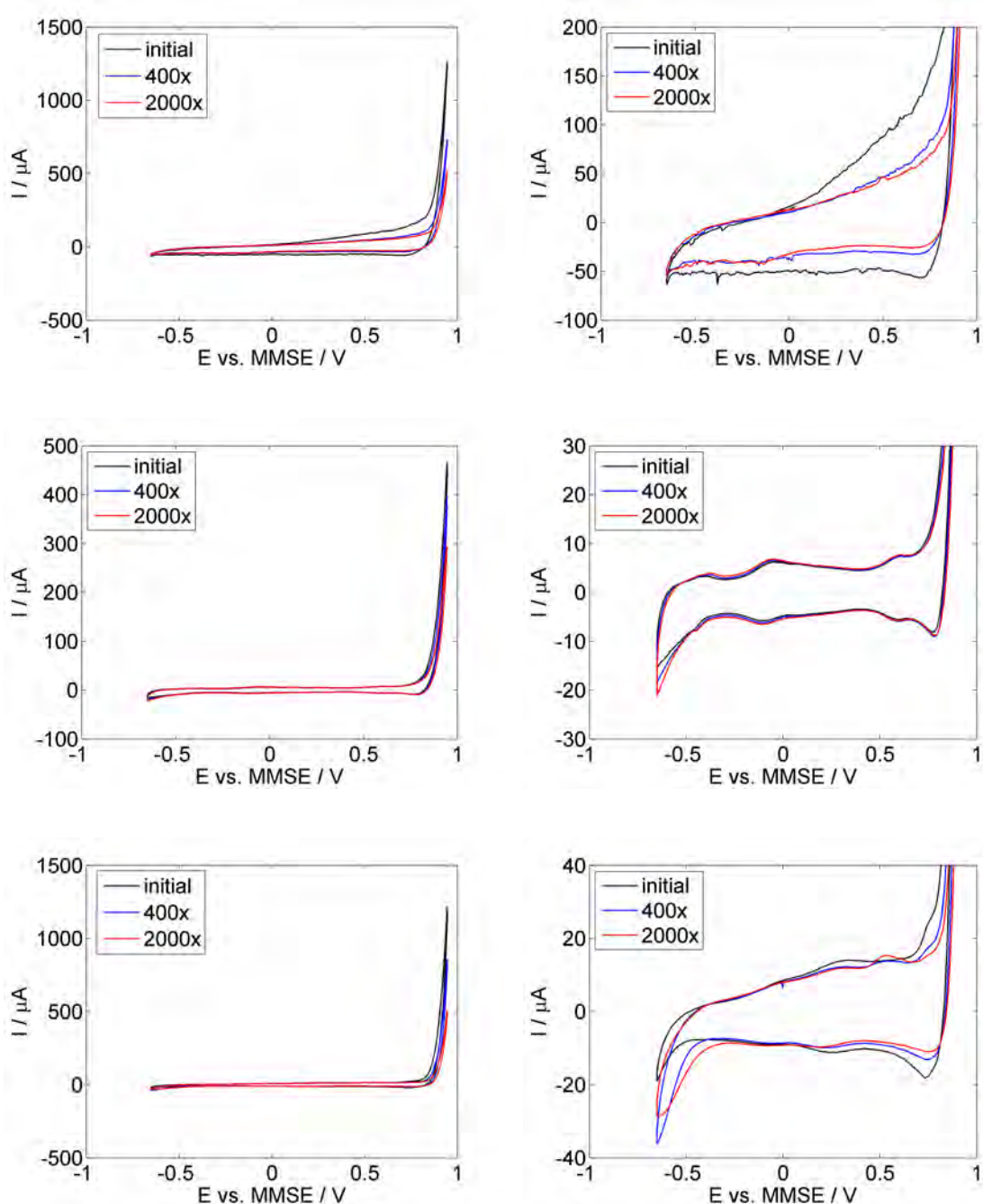
Figure 6.7: *Characterization CVs of Ir nanodots (top), RuO_2 nanoparticles (middle) and Ir@RuO$_2$ (bottom) in total (left) and with a magnified current axis (right). All CVs were recorded in 2 M H_2SO_4 with a sweep speed of 100 mV s^{-1}.*

The increase of cathodic currents at potentials below 0.5 V vs. MMSE at the Ir@RuO$_2$ sample during the stability protocol might be explained by a higher ratio of RuO$_2$ surface to IrO$_2$ surface. The loading of the electrode with the catalyst is defined by the initial OER current. The loading for the selected measurements is (0.6 ± 0.2) mA for RuO$_2$, (1.23 ± 0.06) mA for the Ir nanodots and (2 ± 1) mA for the Ir@RuO$_2$ sample. No influence of the loading on the stability could be observed.
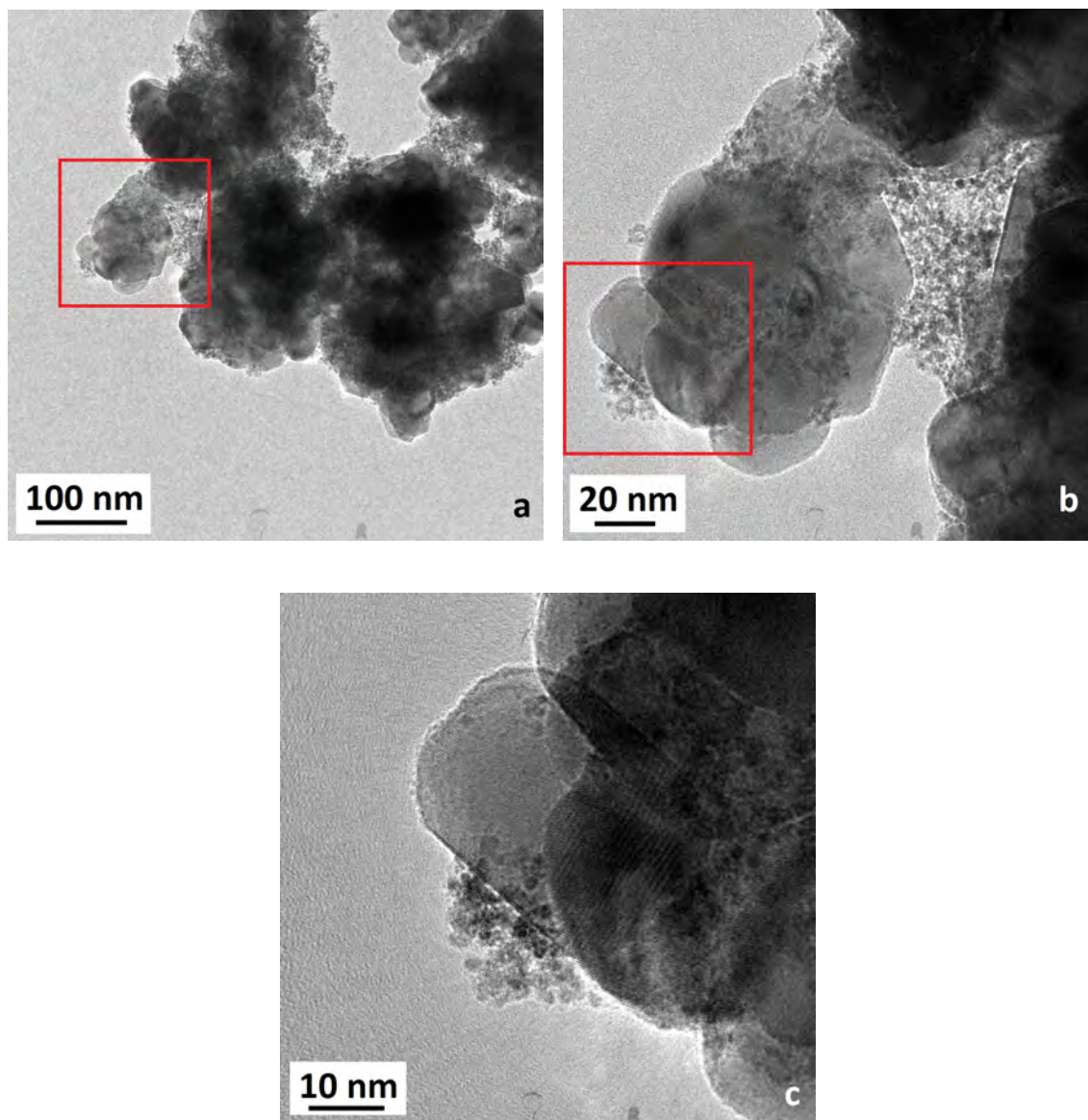
Figure 6.8: *TEM images of Ir decorated RuO$_2$ nanoparticles after 2,000 cycles of the stability protocol. The marked areas in a and b are shown with higher magnification in b and c. No significant change in the morphology of the RuO$_2$ nanoparticles can be observed. Ir nanodots are still present.*

After 2,000 cycles, the OER peak current is decreased to around 60, 50 and 40%

of the initial value for RuO_2 nanoparticles, RuO_2 nanoparticles decorated with Ir nanodots and pure Ir nanodots, respectively. Although the material-specific stability of IrO_2 is higher than that of RuO_2 [9, 34, 59], the Ir nanodots degrade faster than the RuO_2. We attribute this to a size effect: As shown for fuel cell catalysts, smaller nanoparticles are less stable than bigger ones due to their high surface energy [10, 42, 114]. The decoration of RuO_2 with Ir nanodots does not lead to a stability increase. TEM images of the Ir decorated RuO_2 nanoparticles after 2,000 cycles of the stability protocol do not show a significant alteration of the shape or size of the RuO_2 nanoparticles (Fig. 6.8). Moreover, there are still Ir nanodots on the RuO_2 support. Accordingly, EDX measurements yield an Ir:Ru atomic ratio of $(7 \pm 3)\%$ after 2,000 cycles (initial value: $(10 \pm 4)\%$). This can be explained by the fact, that the difference in the stability behavior of Ir nanodots and RuO_2 nanoparticles is not that big: comparing the mean values after 2,000 cycles, the OER stability of Ir is only two thirds of the OER stability of the RuO_2.

6.3 Influence of Annealing

This subsection deals with the question, if the OER stability of Ir@RuO_2 can be improved by a mild annealing procedure, that does not harm the nanostructure of the particles and might improve the adhesion of the Ir nanodots on the RuO_2 support. To study the influence of annealing on the OER stability of Ir@RuO_2, this sample was annealed in a tube furnace under Ar atmosphere. Based on the study on the thermal stability of Ir nanodots (chapter 5.3), the temperature was held on 200°C for 6 hours, to prevent significant Ir degradation. The OER stability of the annealed sample is compared with the values for the sample, that has not been annealed.

6.3.1 Structural Characterization

Fig. 6.9 shows TEM images of Ir@RuO_2 after the annealing procedure. Still, nano-sized structures are observable on the RuO_2 nanoparticles. At least a part of the Ir nanodots seems to be agglomerated to elongated structurs with an average length in the range of 5 nm.
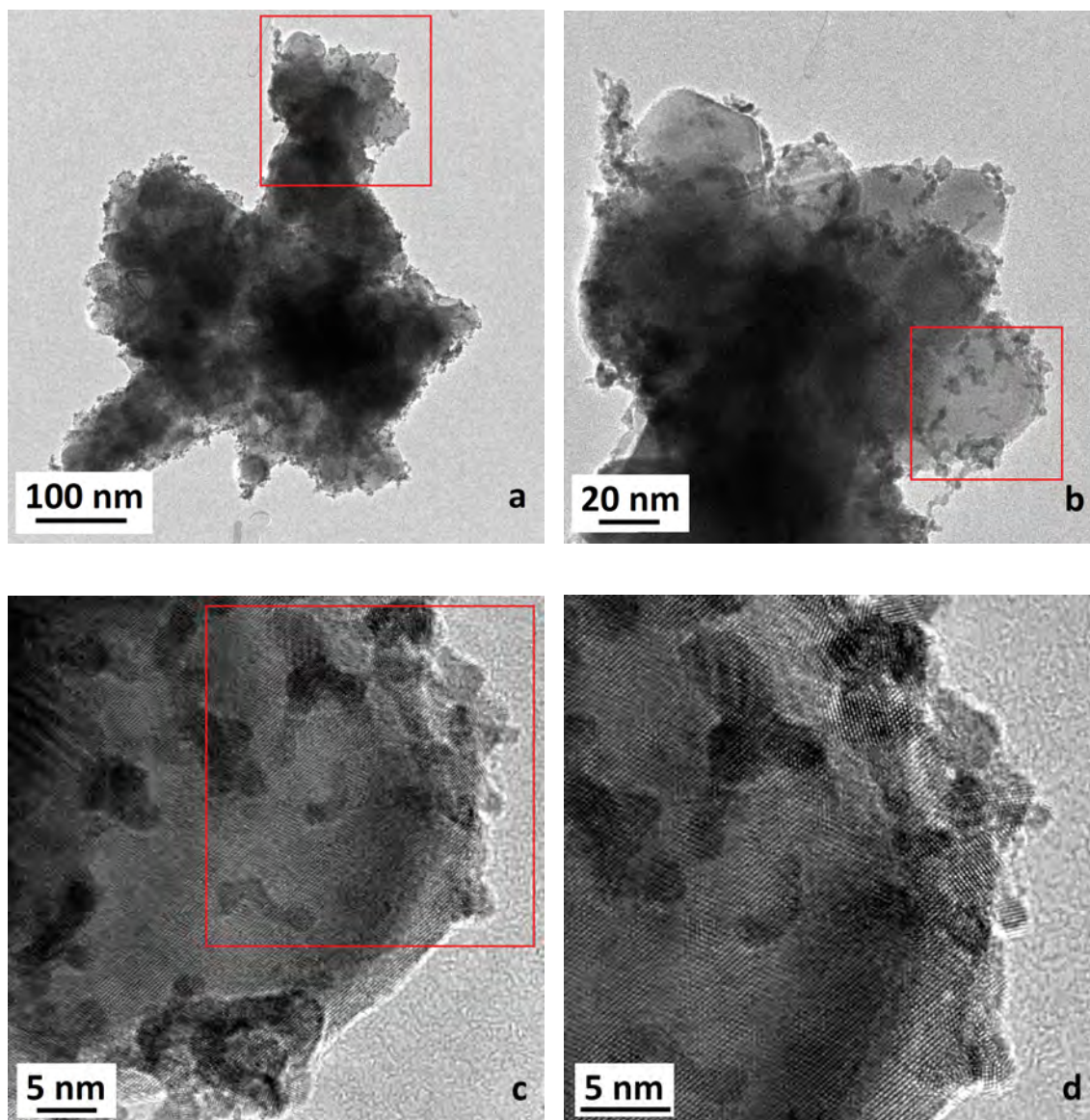
Figure 6.9: *TEM images of Ir@RuO$_2$ after the annealing procedure. The marked areas in a, b and c are shown with higher magnification in b,c and d.*

6.3.2 Electrochemical Characterization

In Fig. 6.10 the first and the last wide potential characterization cycle of the activation protocol are shown for the annealed Ir@RuO$_2$ sample. According to the sample, that was not annealed, the vanishing of the Ir-related HUPD features can be observed.
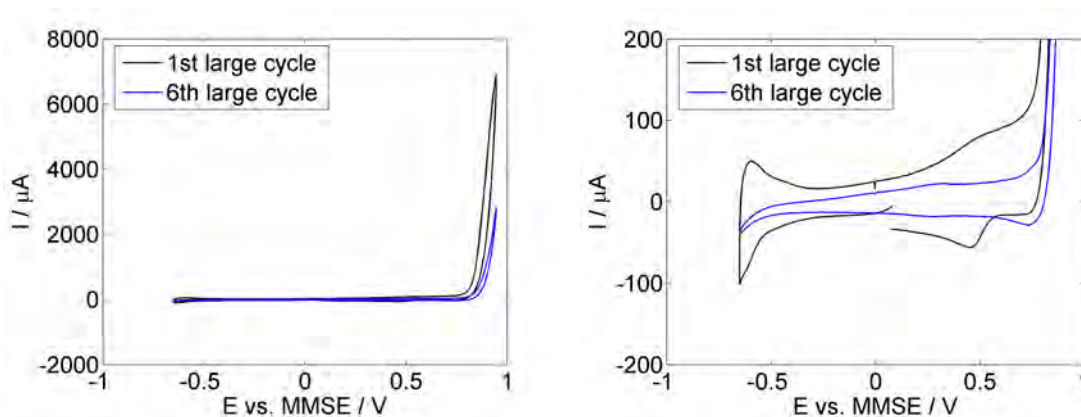
Figure 6.10: *The first and the last wide potential characterization cycle of the activation protocol are shown for the annealed Ir@RuO$_2$ sample. All CVs were recorded in 2 M H$_2$SO$_4$ with a sweep speed of 100 mV s^{-1}.*

The CV of the annealed Ir@RuO$_2$ sample does not differ significantly from the CV of the Ir@RuO$_2$ sample, that was not heat-treated (Fig. 6.11).
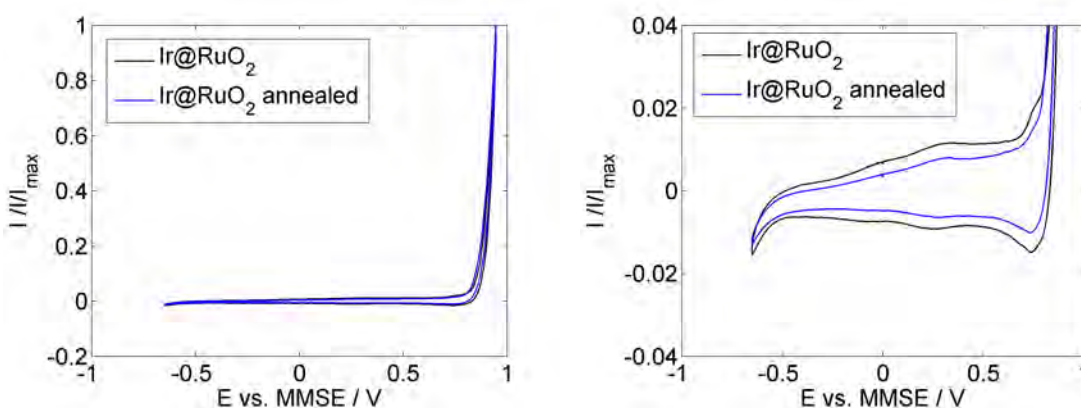
Figure 6.11: *Left: CVs of the annealed Ir@RuO$_2$ sample (blue) and the Ir@RuO$_2$ sample, that was not heat-treated (black). Scan rate: 100 mV s^{-1}. Both CVs are normalized to the peak current, in order to enable better comparability. Right: Detailled view of the smaller CV features.*

The OER stability was calculated as described before. The catalyst loading defined as initial OER current is (1.7 ± 1.4) mA for the annealed Ir@RuO$_2$ sample. That is comparable to the loading of the Ir@RuO$_2$ sample, that was not heat treated $((2 \pm 1)$ mA). No influence of the loading on the stability could be observed. No influence of the annealing procedure on the OER stability is observable (Fig. 6.12).
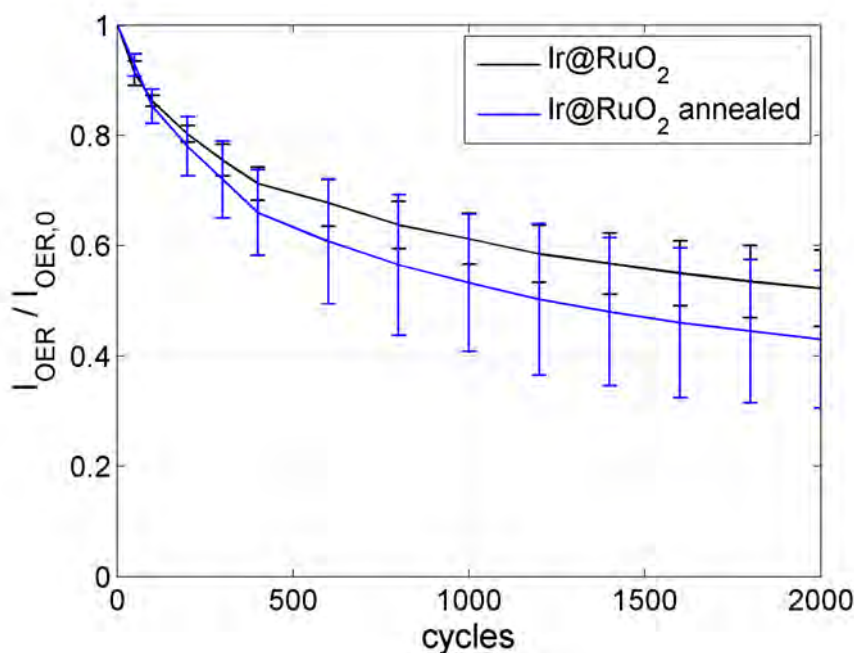
Figure 6.12: *OER stability of the annealed Ir@RuO₂ sample (blue) and the Ir@RuO₂ sample, that was not heat-treated (black).*

6.4 Conclusion

Ir nanodots could succesfully be deposited on RuO_2 nanoparticles. The Ir nanodots are well dispersed on the support.

A shift of the RuO_2 XRD peaks is explained by compressive strain and is reduced by Ir synthesis due to temperature induced relaxation, interaction with the Ir decoration or by enrichment of IrO_2 in the RuO_2. In the case of Ir@RuO_2, peak analysis with the Scherrer equation leads to an apparent decrease of the mean crystallite diameter after Ir decoration. The underlying peak broadening might also be explained by an increase in lattice inhomogeneities due to interaction with the Ir nanodots or due to enrichment of IrO_2 in the RuO_2 particles. The Ir peak broadening of the Ir@RuO_2 sample compared to the pure Ir nanodot sample is explained by inhomogeneous strain due to interaction with the RuO_2.

The OER stability studies yield a decrease of the OER currents of RuO_2 to 60%, of Ir@RuO_2 to 50 % and of Ir to 40% of the initial value after 2,000 cycles of the OER stability protocol. The higher material-specific stability of IrO_2 seems to be overcompensated by size effects. The stability of RuO_2 could not be increased by the decoration with Ir nanodots. After 2,000 cycles, Ir nanodots are still observable on the RuO_2 in TEM and Ir is still detected with EDX spectroscopy.

A mild annealing procedure was performed aiming at an increase of the stability by an improved adhesion of the Ir nanodots to the support, but did not improve the catalysts' OER stability.

Still, the stepwise synthesis allows a uncomparably higher control of the morphology of the composite catalyst and, thus, also the electrochemical properties including the OER stability. Further research is required to deepen the understanding of the interaction of the parts of composite OER catalysts at the surface and to further enhance the stability of composite OER catalysts. For stepwise colloidchemically prepared Ir-Ru-based nanocatalysts the following options might be considered in order to further increase the OER stability:

- deposition of bigger Ir nanoparticles on RuO_2 nanoparticles, since the stability decreases with decreasing diameters for small nanoparticles

- synthesize Ru-based and or Ir-based particles with shapes, that yield a higher stability, since the stability also depends on the particles' surface facets

- use a third material like SnO_2 as support for both, since the stability also depends on the catalyst-support interaction and the amount of noble metal used might be reduced this way

7 Conclusion and Outlook

This thesis investigated the structure and electrochemical stability of noble metal based nanoparticles as catalysts for oxygen reduction and evolution in VARFBs and related systems.

The electrochemical stability of bulk Pt and Carbon supported Pt nanoparticles (Pt/C) was examined with Cyclic Voltammetry under conditions relevant to their use in the positive half-cell of a vanadium air redox flow battery. Analysis of different stability protocols showed neither a decrease of bulk Pt surface nor any influence of V ions on it. It was shown that Pt/C experience a strong degradation when alternating OER and ORR potentials are applied. V ions in the solution lowered the degradation in this case. EQCM measurements performed in the case of bulk Pt in V-containing solution showed no deposition of V compounds, but a decrease of the electrode mass in the range of V^{3+} and VO^{2+} oxidation potential compared to measurements in V-free electrolyte. It is suggested that these oxidations reduce the surface (hydr)oxide occupancy at the Pt electrode. As consequence, the degrading ORR currents are lower, and finally less degradation is observed.

The interaction between the Ir-based OER catalyst and the Pt ORR catalyst in a bifunctional Ir decorated Pt nanorods (Ir@Pt) catalyst towards the electrochemical stability was investigated. The structure and electrochemical stability of Ir@Pt was studied with XRD, TEM, EDX and Cyclic Voltammetry and compared with the single catalysts. Pt nanorods served as support due to their improved stability compared to Pt/C at least under simulated fuel cell operation. The stepwise synthesis allows a higher control of the composite nanoparticles' morphology and, thus, of their activity and stability. Ir nanodots with a 2 nm diameter both without support and deposited on Pt nanorods were successfully synthesized. The nanorods' morphology is stable during Ir synthesis. To investigate the electrochemical stability of the bifunctional Ir@Pt OER-ORR catalyst towards simulated charge-stop and charge-discharge cycles of a VARFB, OER stability protocols as well as OER-ORR stability protocols were conducted. The stability of pure Pt nanorods and Ir decorated Pt is above 90% after 2000 cycles the OER stability protocol, but for the OER-ORR stability protocol it decreases to less than 50% in the case of pure Pt and to 60% in the case of Ir decorated Pt. This stability increase is explained by the Ir degradation and a subsequent uncovering of additional Pt surface area. The stability of Ir supported on Pt drops to less than 20% after 2000 cycles of the OER-ORR stability protocol due to Pt degradation. In all other cases, it is 40%. A mild annealing procedure was conducted aiming at an increase of the stability by an improved adhesion of the Ir nanodots to the support, but did not increase the

OER or ORR stability of Ir@Pt.

Ir nanodots could succefully be deposited on RuO_2 nanoparticles. Investigations on the structure and electrochemical stability of Ir decorated RuO_2 nanoparticles (Ir@RuO_2) were conducted with XRD, TEM, EDX and cyclic voltammetry. The Ir nanodots are well dispersed on the support. The OER stability studies yield a decrease of the OER currents of RuO_2 to 60%, of Ir@RuO_2 to 50% and of Ir to 40% of the initial value after 2,000 cycles of the OER stability protocol. The higher material-specific stability of IrO_2 seems to be overcompensated by size effects. The stability of RuO_2 could not be increased by the decoration with Ir nanodots. A mild annealing procedure was performed in order to increase the stability by an improved adhesion of the Ir nanodots to the support, but did not improve the catalysts' OER stability.

Finally, some hints for further research on noble metal based catalysts for OER and ORR are sketched:

1.) Pt degrades strongly under cycling between OER and ORR potentials. It is, thus, helpful to protect Pt from OER potentials, meaning the use of electrically separated OER and ORR catalysts.

2.) If the use of bifunctional OER-ORR catalysts is appreciated, one has to take into account, that the stability of Ir deposited on Pt suffers from the Pt degradation. However, the stepwise synthesis allows an incomparably higher control of the morphology of the composite catalyst and, thus, the electrochemical properties including the stability. Moreover, the interaction of the composite parts is, yet, hardly understood. For further research on bifunctional OER-ORR catalysts it is useful concerning the stability, to take an Ir-based catalyst as support and deposit Pt on it. Another option is to deposit both catalysts on a stable support like SnO_2.

3.) For further improvements in the field of OER catalysts the research on inhomogeneous surfaces seems to be very promising. For stepwise colloidchemically prepared Ir-Ru-based nanocatalysts the following options might be considered in order to further increase the OER stability:

- deposition of bigger Ir nanoparticles on RuO_2 nanoparticles, since the stability decreases with decreasing diameters for small nanoparticles

- synthesis of Ru-based and or Ir-based particles with surface facets and shapes that yield a higher stability, since the stability also depends on the particles' surface properties

- use of a third material like SnO_2 as support for both, since the stability also

depends on the catalyst-support interaction and the amount of noble metal used might be reduced this way

References

[1] B. Droste-Franke, P.B. Paal, C. Rehtanz, D.U. Sauer, J.P. Schneider, M. Schreurs, T. Ziesemer (Eds.), Balancing Renewable Electricity, Ethics of Science and Technology Assessment, Volume 40, Springer, Berlin (2012).

[2] H. Kaneko, A. Negishi, K. Nozaki, K. Sato, M. Nakajima, EU Patent 0517217 (1992).

[3] H. Kaneko, A. Negishi, K. Nozaki, K. Sato, M. Nakajima, US Patent 5318865 (1992).

[4] C. Menictas, M. Skyllas-Kazacos, J. Appl. Electrochem. 41, 1223 (2011).

[5] S. Hosseiny, M. Saakes, M. Wessling, Electrochem. Commun. 13, 751 (2011).

[6] J. Noack, C. Cremers, D. Bayer, J. Tuebke, K. Pinkwart, J. Power Sources 253, 297 (2014).

[7] J. g. Austing, C. Nunes Kirchner, E.-M. Hammer, L. Komsiyska, G. Wittstock, J. Power Sources 273, 1163 (2015).

[8] C. Gutsche, C. Moeller, M. Knipper, H. Borchert, J. Parisi, T. Plaggenborg, Electrocatalysis, 6, 455 (2015).

[9] S. Park, Y. Shao, J. Liu, Y. Wang, Energy Environ. Sci., 5, 9331 (2012).

[10] I. Katsounaros, S. Cherevko, A.R. Zeradjanin, K.J. Mayrhofer, Angew. Chem. Int. Ed., 53, 102 (2014).

[11] R. Winter (UniEnergy Technologies), 'Chemistry and Engineering to Make a Good Vanadium Battery Better', International Flow Battery Forum, June 6th 2013, Dublin, Ireland.

[12] E. Potiron, A. Le Gal La Salle, A. Verbaere, Y. Piffard, D. Guyomard, Electrochim. Acta 45, 197 (1999).

[13] J.-M. Li, K.-H. Chang, C.-C. Hu, Electrochim. Acta 55, 8600 (2010).

[14] J. Zhang, K. Sasaki, E. Sutter, R.R. Adzic, Science, 315, 220 (2007).

[15] N. Danilovic, R. Subbaraman, K.C. Chang, S.H. Chang, Y. Kang, J. Snyder, A.P. Paulikas, D. Strmcnik, Y.T. Kim, D. Myers, V.R. Stamenkovic, N.M. Markovic, Angew. Chem., 126, 14240 (2014).

[16] M. Skyllas-Kazacos, M.H. Chakrabarti, S.A. Hajimolana, F.S. Mjalli, M.

Saleem, J. Electrochem. Soc. 158, R55 (2011).

[17] L. Joerissen, J. Power Sources 155, 23 (2006).

[18] P. Millet, Hydrogen Production, Wiley-VCH Verlag GmbH & Co. KGaA, 167 (2015).

[19] J. Petterson, B. Ramsey, D. Harrison, J. Power Sources, 157, 28 (2006).

[20] S. Grigoriev, P. Millet, V. Porembsky, V. Fateev, Int. J. Hydrogen Energy, 36, 4164 (2011).

[21] Y.H. Wen, J. Cheng, P.H. Ma, Y.S. Yang, Electrochim. Acta 53, 3514 (2008).

[22] H.A. Gasteiger, N.M. Markovic, Science, 324, 48 (2009).

[23] A. Rabis, P. Rodriguez, T.J. Schmidt, ACS Catalysis, 2, 864 (2012).

[24] M.K. Debe, Nature, 486, 43 (2012).

[25] M. Oezaslan, F. Hasche, P. Strasser, J. Phys. Chem. Lett., 4, 3273 (2013).

[26] M. Escudero-Escribano, A. Verdaguer-Casadevall, P. Malacrida, U. Gruen-bjerg, B.P. Knudsen, A.K. Jepsen, J. Rossmeisl, I.E.L. Stephens, I. Chork-endorff, J. Am. Chem. Soc. 134, 16476 (2012).

[27] D. Strmcnik, D. Li, P.P. Lopes, D. Tripkovic, K. Kodama, V.R. Stamenkovic, N.M. Markovic, Topics in Catalysis, 58, 18, 1174 (2015).

[28] J. Zhang, M.B. Vukmirovic, K. Sasaki, A.U. Nilekar, M. Mavrikakis, R.R. Adzic, J. Am. Chem. Soc, 127, 12480 (2005).

[29] C.H. Wang, H.C. Hsu, K.C. Wang, J. Coll. Int. Sci., 427,91 (2014).

[30] K.A. Stoerzinger, L. Qiao, M.D. Biegalski, Y. Shao-Horn, J. Phys. Chem. Lett., 5, 1636 (2014).

[31] A. Zana, J. Speder, M. Roefzaad, L. Altmann, M. Baeumer, M. Arenz, J. Electrochem. Soc. 160, F608 (2013).

[32] A. Zana, J. Speder, N. E. A. Reeler, T. Vosch, M. Arenz, Electrochim. Acta 114, 455 (2013).

[33] S. Zhang, X.Z. Yuan, J.N.C. Hin, H. Wang, K.A. Friedrich, M. Schulze, J. Power Sources, 194, 588 (2009).

[34] E. Fabbri, A. Habereder, K. Waltar, R. Kotz, T.J. Schmidt, Catal. Sci. Technol., 4, 3800 (2014).

[35] N. Danilovic, R. Subbaraman, K.C. Chang, S.H. Chang, Y. Kang, J. Snyder, A.P. Paulikas, D. Strmcnik, Y.T. Kim, D. Myers, V.R. Stamenkovic, N.M. Markovic, J. Phys. Chem. Lett., 5, 2474 (2014).

[36] E.A. Paoli, F. Masini, R. Frydendal, D. Deiana, C. Schlaup, M. Malizia, T.W. Hansen, S. Horch, I.E.L. Stephens, I. Chorkendorff, Chem. Sci., 6, 190 (2015).

[37] S. Sun, D. Yang, G. Zhang, E. Sacher, J.-P. Dodelet, Chem. Mater., 19, 6376 (2007).

[38] S. Sun, D. Yang, D. Villers, G. Zhang, E. Sacher, J.-P. Dodelet, Adv. Mater., 20, 571 (2008).

[39] S. Sun, G. Zhang, D. Geng, Y. Chen, R. Li, M. Cai, X. Sun, Angew. Chem., 123, 442 (2011).

[40] S. Grigoriev, K. Dzhus, D. Bessarabov, P. Millet, Int. J. Hydrogen Energy, 39, 20440 (2014).

[41] Y. Liu, W.E. Mustain, J. Am. Chem. Soc., 135, 530 (2013).

[42] Y. Liu, L. Zhang, B.G. Willis, W.E. Mustain, ACS Catalysis, 5, 1560 (2015).

[43] M.N. Groves, C. Malardier-Jugroot, M. Jugroot, J. Phys. Chem. C, 116, 10548 (2012).

[44] S.G. Neophytides, K. Murase, S. Zafeiratos, G. Papakonstantinou, F.E. Paloukis, N.V. Krstajic, M.M. Jaksic, J. Phys. Chem. B, 110, 3030 (2006).

[45] R.E. Fuentes, S. Rau, T. Smolinka, J.W. Weidner, ECS Trans., 28, 23 (2010).

[46] R.E. Fuentes, J. Farell, J.W. Weidner, Electrochem. Solid-State Lett., 14, E5 (2011).

[47] K.S. Lee, H.Y. Park, H.C. Ham, S.J. Yoo, H.J. Kim, E. Cho, J. Phys. Chem. C, 117, 9164 (2013).

[48] J. Lee, B. Jeong, J. D. Ocon, Curr. Appl. Phys., 13, 309 (2013).

[49] Y. Zhang, Q. Huang, Z. Zou, J. Yang, W. Vogel, H. Yang, J. Phys. Chem. C, 114, 6860 (2010).

[50] F. Rahman, M. Skyllas-Kazacos, J. Power Sources 72, 105 (1998).

[51] M. Kazacos, M. Cheng, M. Skyllas-Kazacos, J. Appl. Electrochem. 20, 463 (1990).

[52] M. Skyllas-Kazacos, C. Menictas, M. Kazacos, J. Electrochem. Soc. 143, L86

(1996).

[53] L. Li, S. Kim, W. Wang, M. Vijayakumar, Z. Nie, B. Chen, J. Zhang, G. Xia, J. Hu, G. Graff, J. Liu, Z. Yang, Ad Energy Mat. 1, 394 (2011).

[54] T. Reier, M. Oezaslan, P. Strasser, ACS Catal. 2, 1765 (2012).

[55] F. Hasche, M. Oezaslan, P. Strasser, Phys. Chem. Chem. Phys. 12, 15251 (2010).

[56] K. Hartl, M. Hanzlik, M. Arenz, Energy Environ. Sci. 4, 234 (2011).

[57] K. J. J. Mayrhofer, S. J. Ashton, J. C. Meier, G. K. H. Wiberg, M. Hanzlik, M. Arenz, J. Power Sources 185, 734 (2008).

[58] S.Y. Huang, P. Ganesan, H.Y. Jung, B.N. Popov, J. Power Sources, 198, 23 (2012).

[59] E. Antolini, ACS Catal., 4, 1426 (2014).

[60] F.D. Kong, S. Zhang, G.P. Yin, N. Zhang, Z.B. Wang, C.Y. Du, Electrochem. Commun., 14, 63 (2012).

[61] F.D. Kong, S. Zhang, G.P. Yin, Z.B. Wang, C.Y. Du, G.Y. Chen, N. Zhang, Int. J. Hydrogen Energy, 37, 59 (2012).

[62] F.D. Kong, S. Zhang, G.P. Yin, N. Zhang, Z.B. Wang, C.Y. Du, J. Power Sources, 210, 321 (2012).

[63] Y. Zhang, H. Zhang, Y. Ma, J. Cheng, H. Zhong, S. Song, H. Ma, J. Power Sources , 195, 142 (2010).

[64] J. Cruz, V. Baglio, S. Siracusano, R. Ornelas, L. Arriaga, V. Antonucci, A. Aric, Int. J. Hydrogen Energy, 37, 5508 (2012).

[65] Y.H. Pai, C.W. Tseng, J. Power Sources, 202, 28 (2012).

[66] W. Yao, J. Yang, J. Wang, Y. Nuli, Electrochem. Commun., 9, 1029 (2007).

[67] H.Y. Jung, S. Park, B.N. Popov, J. Power Sources, 191, 357 (2009).

[68] Y. Zhang, C. Wang, N. Wan, Z. Mao, Int. J. Hydrogen Energy, 32, 400 (2007).

[69] S.D. Yim, G.G. Park, Y.J. Sohn, W.Y. Lee, Y.G. Yoon, T.H. Yang, S. Um, S.P. Yu, C.S. Kim, Int. J. Hydrogen Energy, 30, 1345 (2005).

[70] S.D. Yim, W.Y. Lee, Y.G. Yoon, Y.J. Sohn, G.G. Park, T.H. Yang, C.S. Kim, Electrochim. Acta, 50, 713 (2004).

[71] T. Ioroi, K. Yasuda, Z. Siroma, N. Fujiwara, Y. Miyazaki, J. Power Sources, 112, 583 (2002).

[72] S. Sui, L. Ma, Y. Zhai, J. Power Sources, 196, 5416 (2011).

[73] G. Zhang, Z.G. Shao, W. Lu, G. Li, F. Liu, B. Yi, Electrochem. Commun., 22, 145 (2012).

[74] K.M. Papazisi, A. Siokou, S. Balomenou, D. Tsiplakides, Int. J. Hydrogen Energy, 37, 16642 (2012).

[75] N. Hodnik, P. Jovanovic, A. Pavlisic, B. Jozinovic, M. Zorko, M. Bele, V.S. Selih, M. Sala, S. Hocevar, M. Gaberscek, J. Phys. Chem. C, 119, 10140 (2015).

[76] R. Frydendal, E.A. Paoli, B.P. Knudsen, B. Wickman, P. Malacrida, I.E.L. Stephens, I. Chorkendorff, ChemElectroChem, 1, 2075 (2014).

[77] R. Koetz, S. Stucki, J. Electrochem. Soc., 132, 103 (1985).

[78] J. Cheng, H. Zhang, G. Chen, Y. Zhang, Electrochim. Acta, 54, 6250 (2009).

[79] M. Carmo, D. L. Fritz, J. Mergel, D. A. Stolten, Int. J. Hydrogen Energy, 38, 4901 (2013).

[80] T. Audichon, E. Mayousse, S. Morisset, C. Morais, C. Comminges, T.W. Napporn, K.B. Kokoh, Int. J. Hydrogen Energy, 39, 16785 (2014).

[81] C.N.R. Rao et al., Nanocrystals: Synthesis, Properties and Applications, Springer, Berlin (2007).

[82] F. J. Owens, C.P. Poole Jr., The Physics and Chemistry of Nanosolids, John Wiley & Sons, Inc., Hoboken (2008).

[83] K.G. Lickfeld, Elektronenmikroskopie, Ulmer, Stuttgart (1979).

[84] B. Fultz, J.M. Howe, Transmission Electron Microscopy and Diffractometry of Materials, Springer, Toyo (2002).

[85] S.L. Fleger et al., Elektronenmikroskopie, Spektrum Akad. Verlag, Heidelberg (1995).

[86] K. Gries, Untersuchungen der Bildungsprozesse und der Struktur des Perlmutts von Abalonen, Ph.D. Thesis, University of Bremen (2011).

[87] J.I. Goldstein et al.: Scanning Electron Microscopy and X-Ray Microanalysis, Plenum Press, New York (1992).

[88] L. Spieß et al., Moderne Röntgenbeugung, Vieweg+Teubner, Wiesbaden

(2009).

[89] J. I. Langford, A. J. C. Wilson, J. Appl. Cryst. 11, 102 (1978).

[90] G. Williamson, W. Hall, Acta Metallurgica, 1, 22 (1953).

[91] D. Pletcher, A First Course in Electrode Processes, RSC Publishing, Cambridge (2009).

[92] D, Pletcher et al., Instrumental Methods in Electrochemistry, Ellis Horwood Limited, Chichester (1985).

[93] C.H. Hamann, W. Vielstich, Elektrochemie, Wiley-VCH, Weinheim (2005).

[94] A.J. Bard, L.R. Faulkner, Electrochemical Methods, John Wiley & Sons, Inc., New York (2001).

[95] P. He, L. P. Faulkner, Anal. Chem. 58, 517 (1986).

[96] E. Gileadi, Physical Electrochemistry, Wiley-VCH, Weinheim (2011).

[97] S.V. De Cliff, Electrochemical Quartz Crystal Microbalance and Impedance Analysis Investigations of Surface Processes at Platinum Electrodes, Ph.D. Thesis, University of Ottawa (1996).

[98] G. Sauerbrey, Z. Phys. 155, 206 (1959).

[99] B. Sun, M. Skyllas-Kazacos, Electrochim. Acta 36, 513 (1991).

[100] W.H. Wang, X.D. Wang, Electrochim. Acta 52, 6755 (2007).

[101] M. Lukaszewski, A. Czerwinski, J. Electroanal. Chem. 589, 38 (2006).

[102] M. Watanabe, H. Uchida, N. Ikeda, J. Electroanal. Chem. 380, 255 (1995).

[103] S. Bruckenstein, M. Shay, J. Electroanal. Chem. 188, 131 (1985).

[104] Y. Lim, E. Hwang, Bull. Korean Chem. Soc. 18, 6 (1997).

[105] M.C. Santos, D.W. Miwa, S.A.S. Machado, Electrochem. Comm. 2, 692 (2000).

[106] G. Jerkiewicz, G. Vatankhah, J. Lessard, M. P. Soriaga, Y.-S. Park, Electrochim. Acta 49, 1451 (2004).

[107] T. Morita, H. Kuroe, A. Eguchi, S. Imabayashi, J. Phys. Chem. C 118, 15114 (2014).

[108] Y. Israel, L. Meites, Vanadium. in: A. J. Bard (Ed.), Encyclopedia of Electrochemistry of the Elements, Dekker, New York (1976).

[109] N. Oehl, P. Michalowski, M. Knipper, J. Kolny-Olesiak, T. Plaggenborg, J. Parisi, J. Phys. Chem. C 118, 30238 (2014).

[110] K.J.J. Mayrhofer, B.B. Blizanac, M. Arenz, V.R. Stamenkovic, P.N. Ross, N.M. Markovic, J. Phys. Chem. B. 109, 14433 (2005).

[111] K. Kinoshita, J. Electrochem. Soc. 137, 845 (1990).

[112] Y. Zhang, S. Chen, Y. Wang, W. Ding, R. Wu, L. Li, X. Qi, Z. Wie, J. Power Sources 273, 62 (2015).

[113] T.J. Schmidt, H.A. Gasteiger, G.D. Staeb, P.M. Urban, D.M. Kolb, R.J. Behm, J. Electrochem. Soc., 145, 2354 (1998).

[114] E.F. Holby, W. Sheng, Y. Shao-Horn, D. Morgan, Energy Environ. Sci., 2, 865 (2009).

Coworkers' Contributions to this Work

The Ir nanodot synthesis was conducted by Christoph Möller under the supervision of Christian Gutsche. The XRD measurements were performed by Christoph Möller under the supervision of Christian Gutsche and by Martin Knipper. A minor part of TEM measurements was performed by Christoph Möller. All TEM measurements were supported by Erhard Rhiel and Ute Friedrich from the University's central TEM facility.

The Pt nanorod synthesis, the major part of the TEM measurements, all EDX measurements and all electrochemical measurements were performed by Christian Gutsche. The analysis of all data was conducted by Christian Gutsche. The data were interpreted by Christian Gutsche under the supervision of Martin Knipper, Holger Borchert, Jürgen Parisi and Thorsten Plaggenborg.

List of publications

Journal Articles

- C. Gutsche, C. Moeller, M. Knipper, H. Borchert, J. Parisi, T. Plaggenborg: "Synthesis, structure and electrochemical stability of Ir decorated RuO_2 nanoparticles and Pt nanorods as oxygen catalysts", J. Phys. Chem. C, 120, 1137 (2016).

- 2015: C. Gutsche, C. Moeller, M. Knipper, H. Borchert, J. Parisi, T. Plaggenborg: "Influence of vanadium ions on degradation of platinum catalysts for vanadium air redox flow batteries", Electrocatalysis, 6, 455 (2015).

Conference Talks

- 2015, Glasgow, International Flow Battery Forum: "Influence of Vanadium Ions on Degradation of Platinum Catalysts for Vanadium Air Redox Flow Batteries"

- 2013, Berlin, 6. Annual Meeting of the Reiner Lemoine Stiftung: "Entwicklung und Charakterisierung bifunktionaler Platin-Iridium-basierter Katalysatoren für Vanadium-Luft-Redox-Flow-Batterien"

- 2010, Dresden, DPG Spring Meeting: "Spatially Resolved Photoluminescence Studies on $CuGaSe_2$- and $CuInSe_2$ Thin-Film Systems"

Poster Presentations at Conferences

- 2015, Berlin, 8. Annual Meeting of the Reiner Lemoine Stiftung: "Influence of Vanadium ions on the degradation behavior of Platinum nanoparticles for Vanadium air redox flow batteries"

- 2014, Berlin, 7. Annual Meeting of the Reiner Lemoine Stiftung: "Influence of Vanadium contamination on Platinum nanoparticles for Vanadium air redox flow batteries"

- 2014, Hamburg, International Flow Battery Forum: "Vanadium crossover in Vanadium air redox flow batteries: Studies on the Influence on Platinum Catalysts"

- 2014, Lille, EMRS Spring Meeting: "Influence of Vanadium contamination on Platinum nanoparticles for Vanadium air redox flow batteries" - awarded as

best poster presentation of the energy storage session

- 2013, Delmenhorst, Next Generation Batteries: "On the influence of Vanadium contaminations on the catalytic properties of Pt nanoparticles for Vanadium air redox flow batteries"

- 2013, Dublin, International Flow Battery Forum: "Towards bifunctional catalysts for vanadium-air redox flow batteries: preparation and characterization of Pt nanoparticles"

- 2013, Karlsruhe, EnMat II: "Towards bifunctional catalysts for vanadium-air redox flow batteries: preparation and characterization of Pt nanoparticles"

Awards

- doctorate scholarship from the Stiftung der Metall-Industrie im Nord-Westen

- doctorate scholarship from the Reiner-Lemoine-Stiftung

- Best Poster Award of the energy storage session at the EMRS Spring Meeting 2014 in Lille for the poster presentation "Influence of Vanadium contamination on Platinum nanoparticles for Vanadium air redox flow batteries"

- student scholarship of the Rosa-Luxemburg-Stiftung

Curriculum Vitae

- since 12/2015: Researcher, Energy and Semiconductor Research Laboratory, University of Oldenburg.

- 12/2012 - 11/2015: Ph.D. student. Thesis evaluated with magna cum laude.

- 07/ 2012 - 11/2012: Researcher, Energy and Semiconductor Research Laboratory, University of Oldenburg. Electron resonance studies on Lithium-Air-Batteries.

- 11/2011 - 01/2012: Teacher for physics, Schule am Leibnizplatz, Bremen.

- 10/2009 - 10/2011: Master of Science student in physics, Universities of Bremen and Oldenburg. Profile: Solid state physics and physics of renewable energies. Final grade: 1.7. Master thesis in the field of photovoltaics at the Helmholtz Centre Berlin and University of Oldenburg (Supervisors: Prof. Dr. K. Lips, Dr. T. Unold, Prof. Dr. G.H. Bauer, grade: 1.7)

- 10/2005 - 09/2009: Bachelor of Science student in physics and biology, University of Bremen. Final grade: 2.3. Bachelor Thesis: AFM studies on mother of pearl (Supervisor: Prof. Dr. M. Fritz, grade: 1.7).

- 06/2004 - 03/2005: Civil service, Friedehorst, Bremen-Lesum.

- 05/2004: High School diploma at the Philipp-Melanchthon-Gymnasium in Gerstungen (Thuringia). grade: 1.3.

Danksagung

Ich danke Christoph Möller und Carli Freudenberg, deren Masterarbeiten ich betreut habe, für die produktive, lehrreiche und erfreuliche Zusammenarbeit.

Ich danke meinen Bürokollegen für die Gespräche über unsere Arbeit und darüber hinaus: Vielen Dank an Matthias, Niko, Daniel, Peter und Atef.

Vielen Dank an all jene Mitglieder der EHF, des Next Energy, des Fraunhofer IFAM und der Uni Oldenburg, die ich nicht namentlich genannt habe, für die gute Zusammenarbeit.

Ingo: danke für das herzliche Willkommen in der AG. Gute Reise.

Zu guter Letzt danke ich meinen Freunden für die gemeinsame Zeit, die Unterstützung, die witzigen und die kritischen Fragen: Laura, Malte, Till, Micha, Dirk, Anja, Andi, Diren, Janne, Sabine, Henrik, Annegret, Philipp und Janina.

Erklärung

Oldenburg, den 29.03.2016

Hiermit erkläre ich, dass ich diese Arbeit selbstständig verfasst und keine anderen als die angegebenen Quellen und Hilfsmittel benutzt habe. Außerdem versichere ich, dass ich die allgemeinen Prinzipien wissenschaftlicher Arbeit und Veröffentlichung, wie sie in den Leitlinien guter wissenschaftlicher Praxis der Carl von Ossietzky Universität Oldenburg festgelegt sind, befolgt habe. Teile der Dissertation wurden bereits veröffentlicht (siehe Publikationsliste). Diese Dissertation liegt weder in ihrer Gesamtheit noch in Teilen einer anderen wissenschaftlichen Hochschule zur Begutachtung in einem Promotionsverfahren vor.

Christian Gutsche